

*Do not go where the path may lead,
go instead where there is no path and leave a trail.*

R.W. Emerson

University of Alberta

Cyclotron Production of Technetium-99m

by

Katherine M Gagnon

A thesis submitted to the Faculty of Graduate Studies and Research
in partial fulfillment of the requirements for the degree of

Doctor of Philosophy

in

Medical Physics

Department of Physics

© Katherine M. Gagnon

Spring 2012

Edmonton, Alberta

Permission is hereby granted to the University of Alberta Libraries to reproduce single copies of this thesis and to lend or sell such copies for private, scholarly or scientific research purposes only. Where the thesis is converted to, or otherwise made available in digital form, the University of Alberta will advise potential users of the thesis of these terms.

The author reserves all other publication and other rights in association with the copyright in the thesis and, except as herein before provided, neither the thesis nor any substantial portion thereof may be printed or otherwise reproduced in any material form whatsoever without the author's prior written permission.

Abstract

Technetium-99m (^{99m}Tc) has emerged as the most widely used radionuclide in medicine and is currently obtained from a $^{99}\text{Mo}/^{99m}\text{Tc}$ generator system. At present, there are only a handful of ageing reactors worldwide capable of producing large quantities of the parent isotope, ^{99}Mo , and owing to the ever growing shutdown periods for maintenance and repair of these ageing reactors, the reliable supply ^{99m}Tc has been compromised in recent years. With an interest in alternative strategies for producing this key medical isotope, this thesis focuses on several technical challenges related to the direct cyclotron production of ^{99m}Tc via the $^{100}\text{Mo}(p,2n)^{99m}\text{Tc}$ reaction.

In addition to evaluating the $^{100}\text{Mo}(p,2n)^{99m}\text{Tc}$ and $^{100}\text{Mo}(p,x)^{99}\text{Mo}$ reactions, this work presented the first experimental evaluation of the $^{100}\text{Mo}(p,2n)^{99g}\text{Tc}$ excitation function in the range of 8–18 MeV. Thick target calculations suggested that large quantities of cyclotron-produced ^{99m}Tc may be possible. For example, a 6 hr irradiation at 500 μA with an energy window of 18→10 MeV is expected to yield 1.15 TBq of ^{99m}Tc . The level of coproduced ^{99g}Tc contaminant was found to be on par with the current $^{99}\text{Mo}/^{99m}\text{Tc}$ generator standard eluted with a 24 hr frequency.

Highly enriched ^{100}Mo was required as the target material for ^{99m}Tc production and a process for recycling of this expensive material is presented. An 87% recovery yield is reported, including metallic target preparation, irradiation, ^{99m}Tc extraction, molybdate isolation, and finally hydrogen reduction to the metal. Further improvements are expected with additional optimization experiments. A

method for forming structurally stable metallic molybdenum targets has also been developed. These targets are capable of withstanding more than a kilowatt of beam power and the reliable production and extraction of Curie quantities of ^{99m}Tc has been demonstrated.

With the end-goal of using the cyclotron-produced ^{99m}Tc clinically, the quality of the cyclotron-produced ^{99m}Tc has been extensively compared with relevant United States Pharmacopeia (USP) specifications for the existing $^{99}\text{Mo}/^{99m}\text{Tc}$ production strategy. Additional quality testing, including biodistribution studies of [^{99m}Tc]pertechnetate and [^{99m}Tc]disofenin in both mice and rabbits was also evaluated. Using the strategies and results presented throughout this dissertation, this thesis concludes with the world's first cyclotron-based ^{99m}Tc patient images obtained as part of a Phase I Clinical Trial at the University of Alberta using [^{99m}Tc]pertechnetate.

Acknowledgements

Thank you to everyone who has helped me along the way. The ongoing support from my parents, family, and friends has had a strong and positive influence in my successful accomplishment of this exciting milestone. Rather than the traditional saying of, “Publish or Perish”, when procrastinating on my writing, I will certainly never forget my mom’s favorite words of motivation which always made me laugh, “Write it or Bite it”. While I never imagined, when moving to Edmonton, that there would be days where it didn’t matter if the temperature was being reported in Celsius or Fahrenheit, it was sure great to have had many friends to share fun adventures with in this frosty town. Big hugs to all! ☺

The work presented in this thesis would not have been possible without help from teams in the CCI Department of Nuclear Medicine, Edmonton Radiopharmaceutical Centre, Edmonton PET Centre, CCI Machine Shop, CCI Clinical Trials Group, and collaborators, both at the U of A and abroad including TRIUMF, Risø, and BNL. In particular, acknowledgements are extended to Guangcheng Chen for help with the ICP-MS measurements, Alicia Strelkov for assistance with the animal studies, Mariusz Bereznicki for coordinating the supply of generators and helping with clinical ^{99m}Tc QC, Joseph Romaniuk for chemistry automation, Chris Holt for assistance with target fabrication, and my supervisors, Don Robinson and Steve McQuarrie. Be it taking an extra course, visiting a lab to learn some new skills, being invited and welcomed to non-research-based meetings (e.g. regulatory, facility planning, funding, etc.), or working on many other non- ^{99m}Tc projects throughout my PhD, Steve has always been extremely supportive of my continued desire for learning and growth, both academically and professionally. For this, I am very grateful. I am also thankful to have had the opportunity to work with Sandy McEwan. Thanks to his strong vision, this research was seen all the way through to a Phase I Clinical Trial. His enthusiasm and drive for this project were highly motivating and I look forward to learning of the progress and successes with the new TR-24 facility. An extra special thanks goes out to John Wilson and the countless number of hours and weekends of his

help in the lab. No matter how many times Murphy's Law might strike in a day, any feelings of setback were always eclipsed by John's positive laughter which could, of course, be heard from down the hall. As a mentor throughout my studies, I also thank Tom Ruth for introducing me to the exciting world of isotope production, but moreover, encouraging me to follow my dreams.

This work was funded through an NSERC graduate scholarship (PGS-D), a grant from NSERC/CIHR (MIS 100934), and Natural Resources Canada's Non-Reactor Based Isotope Supply Contribution Program (NISP). Existing TR-19/9 cyclotron infrastructure used for these studies has been supported by the Canada Foundation for Innovation, the Alberta Cancer Foundation and Alberta Infrastructure. I am grateful to the funding agencies for making this research possible.

Table of Contents

1.	Introduction.....	1
1.1.	Technetium	1
1.2.	^{99m}Tc in medicine.....	3
1.3.	Reactor-based production of ^{99m}Tc	7
1.4.	Current ^{99m}Tc supply challenges.....	8
1.5.	Alternative production strategies	11
1.6.	Cyclotron production of technetium	12
1.7.	Thesis overview	13
1.8.	References.....	14
2.	A starting point – Cyclotron production of ^{94m}Tc	20
2.1.	Introduction.....	20
2.2.	^{94m}Tc as an alternative to ^{99m}Tc	20
2.3.	Production and processing of ^{94m}Tc	21
2.3.1.	^{94m}Tc Production	21
2.3.2.	^{94m}Tc Target preparation	25
2.3.3.	^{94m}Tc Target processing	26
2.4.	References.....	30
3.	$^{100}\text{Mo}(p,x)$ Cross sections	36
3.1.	Introduction.....	36
3.2.	Materials and methods	38
3.2.1.	Foil irradiations	38
3.2.2.	Activity assay.....	41
3.2.3.	Monitor reactions	47

3.2.4.	ICP-MS	48
3.2.5.	Cross section calculations	52
3.3.	Results and discussion	53
3.3.1.	$^{100}\text{Mo}(p,x)^{99}\text{Mo}$	53
3.3.2.	$^{100}\text{Mo}(p,2n)^{99m}\text{Tc}$	55
3.3.3.	$^{100}\text{Mo}(p,2n)^{99g}\text{Tc}$	58
3.4.	Conclusion	62
3.5.	References.....	62
4.	Energy evaluation	65
4.1.	Introduction.....	65
4.2.	Theory.....	66
4.3.	Materials and methods.....	69
4.3.1.	Monitor foils	70
4.3.2.	Degrader thickness.....	70
4.3.3.	Expected activity ratio	73
4.3.4.	Irradiation parameters	74
4.3.5.	Foil measurements	75
4.3.6.	Calculating the measured activity ratio.....	76
4.4.	Results and discussion	79
4.5.	Conclusion	82
4.6.	References.....	82
5.	Recycling ^{100}Mo metal.....	84
5.1.	Introduction.....	84
5.2.	Materials and methods.....	86

5.2.1.	Target irradiation.....	86
5.2.2.	Target dissolution.....	88
5.2.3.	^{99m} Tc/ ¹⁰⁰ Mo separation.....	88
5.2.4.	Molybdate isolation	90
5.2.5.	Molybdenum reduction	91
5.2.6.	Molybdenum isotopic composition.....	93
5.2.7.	Radionuclidic analysis	93
5.2.8.	^{99m} Tc Radiochemical analysis	94
5.3.	Results.....	95
5.3.1.	Molybdenum reduction and recovery	95
5.3.2.	Molybdenum isotopic composition.....	97
5.3.3.	^{99m} Tc Radionuclidic analysis	97
5.3.4.	^{99m} Tc Radiochemical analysis	100
5.4.	Discussion	101
5.5.	Conclusion	102
5.6.	References.....	103
6.	High-current metallic ¹⁰⁰ Mo targets	106
6.1.	Introduction.....	106
6.2.	Materials and methods	108
6.2.1.	Sintering overview	108
6.2.2.	Sintering optimization.....	109
6.2.3.	Bonding.....	110
6.2.4.	Irradiation.....	113
6.2.5.	Target dissolution and ^{99m} Tc extraction.....	115

6.3.	Results and discussion	116
6.3.1.	Sintering.....	116
6.3.2	Bonding.....	118
6.3.3.	Irradiation.....	118
6.4.	Conclusion	121
6.5.	References.....	122
7.	Quality control of cyclotron produced ^{99m}Tc	126
7.1.	Introduction.....	126
7.2.	Materials and methods	127
7.2.1.	USP specifications	130
7.2.2.	Additional chemical purity tests	133
7.2.3.	Stability of $[\text{}^{99m}\text{Tc}]\text{TcO}_4^-$ and labelling of other ^{99m}Tc - pharmaceuticals.....	134
7.2.4.	Biodistribution studies	135
7.3.	Results and Discussion	137
7.3.1.	USP specifications	137
7.3.2.	Additional chemical purity tests	140
7.3.3.	Stability of $[\text{}^{99m}\text{Tc}]\text{TcO}_4^-$ and labelling of other ^{99m}Tc - pharmaceuticals.....	140
7.3.4.	Biodistribution studies	143
7.4.	Conclusion	149
7.5.	References.....	149
8.	Summary and future direction	151
8.1.	Research summary.....	151
8.2.	Future research.....	154

8.3. References..... 155

List of Tables

Table 1-1. Summary of reactors and 2008 market shares for commercial production of ^{99}Mo [23, 29].	9
Table 2-1. Selection of published data on $^{94\text{m}}\text{Tc}$ production.	24
Table 3-1. Isotopic compositions of natural abundance and enriched molybdenum foils.	39
Table 3-2. Summary of nuclear decay data obtained from the NNDC NuDat database [7].	45
Table 3-3. Experimental cross sections (in mb) measured in this work assuming 100% ^{100}Mo enrichment.	54
Table 3-4. Summary of the EOB thick target $N_{m\text{Tc}}/N_{m+g\text{Tc}}$ ratio and the $^{99\text{m}}\text{Tc}$ yields for eight irradiation conditions.	60
Table 4-1. The recommended aluminum degrader thicknesses and second order curve fitting terms.	72
Table 4-2. The nominal proton irradiation energies and nominal/measured foil thicknesses.	75
Table 4-3. The proton energies evaluated in this experiment using the ^{63}Zn activity ratio.	81
Table 5-1. Irradiation conditions for new (N) and recycled (R) ^{100}Mo metal targets.	87
Table 5-2. Summary of reduction temperatures/atmospheres implemented in this ^{100}Mo study.	92
Table 5-3. The nominal (Isoflex COA) and measured percent isotopic composition for new and recycled ^{100}Mo .	97

Table 5-4. Percent of impurity activity to ^{99m}Tc activity at EOB for new and recycled ^{100}Mo targets. _____	98
Table 5-5. $[\text{}^{99m}\text{Tc}]\text{TcO}_4^-$ pH, radiochemical purity, and Al^{3+} concentration evaluated in this study following irradiation of both new and recycled ^{100}Mo . _____	100
Table 6-1. Programmed temperature profile used for sintering of molybdenum metal pellets. _____	109
Table 6-2. Irradiation conditions for the $^{\text{nat}}\text{Mo}$ and ^{100}Mo targets prepared in this study. _____	115
Table 6-3. Percent of theoretical saturated yield based on assays performed prior to extraction, and post extraction. _____	121
Table 7-1. The two ^{100}Mo batches used for ^{99m}Tc production at the EPC. _____	128
Table 7-2. A chronological summary of all thick target experiments performed with enriched ^{100}Mo up to September 2011. _____	129
Table 7-3. Summary of nuclear decay data obtained from the NNDC NuDat database [6]. _____	132
Table 7-4. Summary of test results to evaluate USP specifications. _____	138
Table 7-5. Relative RNP data reported as a percentage of ^{99m}Tc at EOB. _____	139
Table 7-6. $[\text{}^{99m}\text{Tc}]\text{TcO}_4^-$ radiochemical purity and stability from 1–50 hr post extraction. _____	141
Table 7-7. Labelling efficiency and stability for MDP and disofenin. _____	142
Table 7-8. 15 kBq $[\text{}^{99m}\text{Tc}]\text{disofenin}$ uptake in mice 1 hr post-injection. _____	144
Table 7-9. 40 MBq $[\text{}^{99m}\text{Tc}]\text{TcO}_4^-$ uptake in at 25, 40, and 55 minutes post-injection using the same rabbit. _____	145

List of Figures

- Figure 1-1. Simplified decay scheme for ^{99}Mo . _____ 2
- Figure 3-1. Select subset of reactions following the proton irradiation of ^{100}Mo which give rise both to the direct and indirect production of both $^{99\text{m}}\text{Tc}$ and $^{99\text{g}}\text{Tc}$. _____ 37
- Figure 3-2. HPGe detector efficiency calibration curve measured for a 25 cm sampling distance. Efficiency data is plotted against the natural log of energy for ease of curve fitting. Two separate polynomial curves are given; the blue curve is used for $E_\gamma < 350$ keV while the red curve is used for $E_\gamma > 350$ keV. _____ 41
- Figure 3-3. Sample m/z count rates for both a non-irradiated and an irradiated enriched ^{100}Mo foil. Each foil underwent chemical extraction to separate the bulk ^{100}Mo . Error bars are given as the standard deviation of the three replicate readings. _____ 50
- Figure 3-4. Experimental excitation function for the $^{100}\text{Mo}(p,x)^{99}\text{Mo}$ reaction. Error bars for the short ^{100}Mo irradiations are included. _____ 55
- Figure 3-5. Experimental excitation function for the $^{100}\text{Mo}(p,2n)^{99\text{m}}\text{Tc}$ reaction. Error bars for the short ^{100}Mo irradiations are included. _____ 56
- Figure 3-6. Experimental excitation function for the $^{100}\text{Mo}(p,2n)^{99\text{g}}\text{Tc}$ and $^{100}\text{Mo}(p,2n)^{99\text{m}}\text{Tc}$ reactions. _____ 59
- Figure 3-7. Saturated thick target $^{99\text{m}}\text{Tc}$ yields [GBq/ μA]. Yields have been calculated based on a 1 MeV step size, and coincide with the line intersections. In other words, the color represents an average of the yield calculated at the four respective intersections. The thickness of metallic ^{100}Mo required to degrade the respective energy assuming a perpendicular beam orientation is also reported. _____ 61

Figure 4-1. The configuration of the two copper foils and aluminum energy degrader irradiated in this experiment. The above figure is not to scale – the copper foil thicknesses have been exaggerated for the purpose of illustration. _____ 67

Figure 4-2. A comparison of the ^{63}Zn activation for two 25 μm copper foils and an 875 μm aluminum degrader given incident proton energies of (a) 15.0 MeV, and (b) 15.5 MeV using the IAEA recommended cross-section data [1]. Calculated using the SRIM software package [6], the shaded regions represent the finite energy loss in each of the two copper foils and the aluminum degrader. _____ 69

Figure 4-3. The expected ^{63}Zn activity ratio calculated from equation (4.3) as a function of proton energy for aluminum degraders ranging in thickness from 650–850 μm . _____ 71

Figure 4-4. A plot of the residuals for the decay curve fitting of the ten dose-calibrator readings for the first copper foil for the 18.6 MeV cyclotron irradiation. Plot A was obtained using the fitting function described in equation (4.5), while B was obtained from the fitting function of equation (4.6). _____ 78

Figure 4-5. A sample plot of the proton energy, E_p , as a function of the expected ^{63}Zn ratio, r . The plot is made with the coefficients from Table 4-1, and assumes a nominal 350 μm aluminum foil and two nominal 25 μm copper monitor foils. The straggling and energy loss of a nominal 25 μm aluminum vacuum window is included in the calculations. _____ 80

Figure 5-1. A schematic of the $^{99\text{m}}\text{Tc}$ separation strategy using ABEC-2000 resin. _____ 89

Figure 5-2. The temperature profile measured during the reduction of [^{100}Mo]ammonium molybdate to metal. _____ 92

Figure 5-3. Powder XRD of the isolated and reduced [^{100}Mo] ammonium molybdate, with comparison XRD of commercially available ^{100}Mo metal (Isoflex), $^{\text{nat}}\text{MoO}_3$ (Alfa Aesar) and $^{\text{nat}}\text{MoO}_2$ (Alfa Aesar). _____ 96

Figure 5-4. Sample γ -ray spectra to 1 MeV for (a) an aliquot of final extracted $^{99\text{m}}\text{Tc}$ obtained following irradiation of recycled ^{100}Mo , and (b) an aliquot of the ^{100}Mo collection vial. Samples were measured for 1 hr LT starting at 4.2 hr and 2.6 hr post-EOB, respectively. _____ 99

Figure 5-5. 40 MBq [$^{99\text{m}}\text{Tc}$]MDP uptake 2 hr post-injection for: (a) $^{99\text{m}}\text{Tc}$ from a generator, and (b) $^{99\text{m}}\text{Tc}$ obtained from cyclotron irradiation of recycled ^{100}Mo . The same rabbit was used for both images and imaged 6 days apart. _____ 101

Figure 6-1. Schematic denoting (a) the assembly of the tantalum plate, molybdenum powder, and tantalum “cap”, (b) the complete plate system as inserted into the sintering oven, and (c) a cross-sectional cut-out through the plate system. Green = tantalum, blue = molybdenum. _____ 110

Figure 6-2. A sample measured temperature profile of both the top and bottom heating elements of the SUSS wafer bonding system. _____ 112

Figure 6-3. Three views of the 30 degree ACSI solid target system showing both the water and helium cooling sections of the target (schematics courtesy of ACSI). _____ 114

Figure 6-4. Picture of the target system used for irradiation of the ^{100}Mo targets developed in this work. The target plate shown in this photo does not contain any ^{100}Mo or o-ring. The approximate location where the thermocouple was affixed to the helium cooling assembly has been indicated by a star. ____ 114

Figure 6-5. SEM image of pressed $^{\text{nat}}\text{Mo}$ (left) versus pressed and sintered $^{\text{nat}}\text{Mo}$ (right). _____ 117

Figure 6-6. An edge-on SEM view of a sintered $^{\text{nat}}\text{Mo}$ pellet broken in two. _ 117

Figure 6-7. A ^{nat}Mo target pre (left)- and post (right)- irradiation.	119
Figure 7-1. 40 MBq [^{99m}Tc]disofenin uptake in two different rabbits 5–10 minutes post-injection using (a) generator-based and (b) cyclotron-based ^{99m}Tc .	143
Figure 7-2. ROI delineations to evaluate uptake of 40 MBq [^{99m}Tc]TcO $_4^-$ in the same rabbit for a 50 minute dynamic scan acquisition using both generator and cyclotron sources of ^{99m}Tc .	146
Figure 7-3. 30 kBq [^{99m}Tc]TcO $_4^-$ uptake in mice as a function of time post-injection. Four subplots are given for ease of visualization.	147
Figure 7-4. 30 kBq [^{99m}Tc]TcO $_4^-$ uptake in mice (a) 15 min, (b) 45 min, and (c) 4 hr post-injection (*p < 0.05).	148
Figure 8-1. Whole body [^{99m}Tc]TcO $_4^-$ image for (a) cyclotron and (b) generator [^{99m}Tc]TcO $_4^-$.	153

List of Abbreviations

ABEC = aqueous biphasic extraction chromatography

ACSI = Advanced Cyclotron Systems Inc.

AE = automated extraction

Al = aluminum

Annih = annihilation

Ba = barium

BNL = Brookhaven National Lab

Cd = cadmium

Co = cobalt

COA = certificate of analysis

Cr = chromium

Cs = cesium

CT = computed tomography

Cts = counts

Cu = copper

d = deuteron

DTPA = diethylenetriaminepentaacetic acid

E_p = proton energy

E_γ = γ -ray energy

EBS = ethylene bis stearamide

ECD = ethylcysteinate dimer

EOB = end of bombardment

EPC = Edmonton PET Centre

ERC = Edmonton Radiopharmaceutical Centre

Fe = iron

g = ground state

G = gauge

GIT = gastrointestinal tract

HEU = highly enriched uranium
HIDA = hepatobiliary iminodiacetic acid
HM-PAO = hexamethylpropyleneamine oxime
HPGe = high purity germanium
I = iodine
IAEA = International Atomic Energy Agency
ICP-MS = inductively coupled plasma mass spectrometry
ID = inner diameter
In = indium
ITLC = instant thin layer chromatography
LEGP = low energy general purpose
LEU = low enriched uranium
m = metastable state
MAG3 = mercaptoacetyltriglycine
MAPLE = Multipurpose Applied Physics Lattice Experiment
MDP = methylene diphosphonate
ME = manual extraction
MEK = methyl ethyl ketone
Mg = magnesium
MIBI = methoxyisobutylisonitrile
Mn = manganese
Mo = molybdenum
MRI = magnetic resonance imaging
n = neutron
N = new ¹⁰⁰Mo
Na = sodium
nat = natural abundance
Nb = niobium
ND = not detected
NE = not evaluated

NISP = Non-reactor-based Isotope Supply Contribution Program

NIST = National Institute of Standards and Technology

NNDC = National Nuclear Data Center

No = number

NRU = National Research Universal

p = proton

PET = positron emission tomography

ppb = parts per billion

ppt = parts per trillion

PTFE = polytetrafluoroethylene

QC = quality control

R = recycled ¹⁰⁰Mo

RCP = radiochemical purity

Re = rhenium

RNP = radionuclidic purity

ROI = region of interest

Ru = ruthenium

SA = silicic acid

sccm = standard cubic centimetres per minute

SCX = strong cation exchange

SEM = scanning electron microscope

SG = salivary gland

SG = silica gel

Si = silicon

SOC = start of counts

SPECT = single photon emission computed tomography

SRIM = Stopping and Range of Ions in Matter

Ta = tantalum

Tc = technetium

Ti = titanium

TRIM = TRansport of Ions in Matter

TZF = three zone tube furnace

U = uranium

UHP = ultra high purity

US = United States

USP = United States Pharmacopeia

W = tungsten

XRD = x-ray diffraction

Zn = zinc

List of Symbols

A = activity of isotope

B = background fitting parameter

C = net counts in peak area

ε_{ext} = extraction efficiency

ε_i = detector efficiency at energy i

E_0 = fitting parameter

E_p = proton energy

f = branching ratio

Φ = proton irradiation current

η = number of target nuclei per unit area

I = absolute γ -ray intensity

κ = fitting parameter

K = fitting parameter

λ = disintegration constant

m = mass

$R(t)$ = Capintec reading at time t

σ = energy dependent cross section

s = fitting parameter

t = time

$t_{1/2}$ = half-life

t_b = bombardment time

t_A = time elapsed between EOB and SOC

t_{el} = time elapsed between two generator elutions

t_L = live time

t_R = real time

Z = atomic number

1. Introduction

1.1. Technetium

Technetium has the distinction of being the lowest atomic number element ($Z = 43$) for which no stable isotope exists. It is for this reason that its name arises from the Greek word “technetos,” which means “artificial” [1]. While its neighbouring elements of molybdenum ($Z = 42$) and ruthenium ($Z = 44$) were discovered in 1778, and 1844, respectively [2], the discovery of technetium which at the time was named “Element 43” occurred many years later, and is generally attributed to the 1937 investigation by Perrier and Segrè [3]. In their study, the discovery of Element 43 was made possible following the irradiation of molybdenum on a cyclotron:

“Professor E. O. Lawrence gave us a piece of molybdenum plate which had been bombarded for some months by a strong deuteron beam in the Berkley cyclotron”. [3]

Identified by the lack of beta emission, it was only two years later in 1939 that Seaborg and Segrè reported on the nuclear transition from an excited nuclear state to a ground state of Element 43 [4]. In this study, they isolated a parent isotope having a half-life of 67 ± 2 hr which they attributed to either ^{101}Mo or ^{99}Mo . This is now known to be ^{99}Mo which has a half-life of 65.94 hr. The

discovery of an isomeric state of Element 43, i.e. ^{99m}Tc , by Seaborg and Segrè was quite an impressive feat considering that technetium was itself only discovered two years earlier. The currently accepted half-life of 6.0058 hr and a γ -ray energy of 140.511 keV for ^{99m}Tc decaying to ^{99g}Tc , $t_{1/2} = 2.111 \times 10^5$ y are also consistent with this pioneering work. A simplified schematic of the ^{99}Mo decay scheme is given in Figure 1-1.

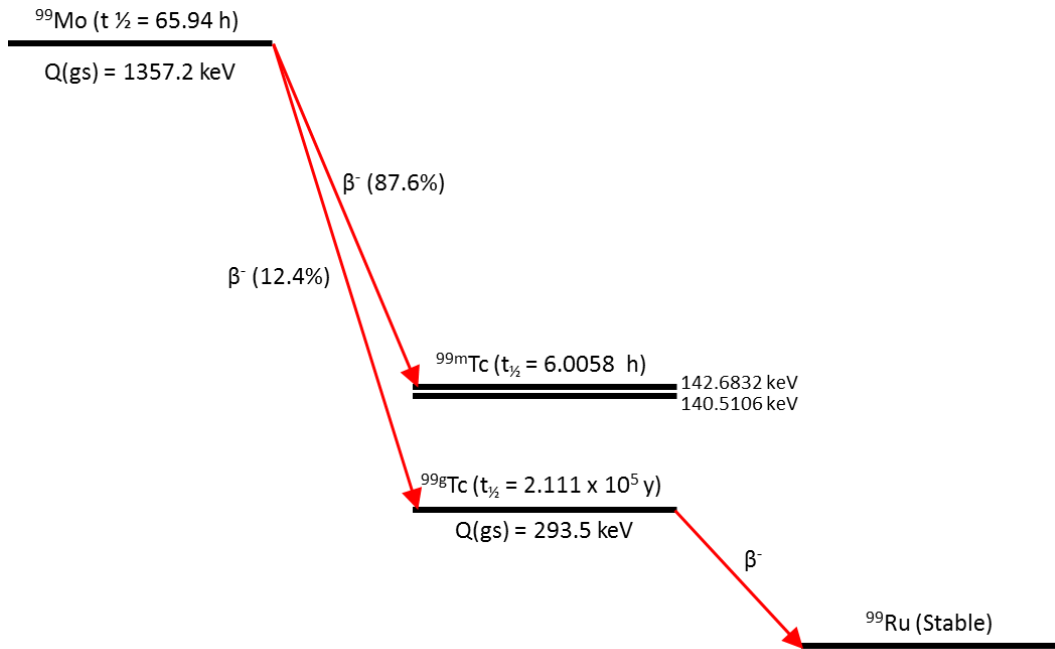


Figure 1-1. Simplified decay scheme for ^{99}Mo .

More exciting research developments surrounding ^{99m}Tc followed the 1939 study. Once again using the Berkley cyclotron, this time as a source of neutrons, ^{99m}Tc was identified in 1940 as a decay product of ^{99}Mo produced following the fissioning of uranium [5]. Both charged-particle and fission-based studies of technetium radioisotopes continued [6, 7], and a new and simple strategy to isolate ^{99m}Tc was developed in the late 1950's. During the refinement of a $^{132}\text{Te}/^{132}\text{I}$ generator at Brookhaven National Lab (BNL), Richards [8]

described that the fission-produced contaminant ^{99}Mo followed the chemistry of tellurium, while its $^{99\text{m}}\text{Tc}$ decay product followed the chemistry of iodine. These chemical similarities led to the development of the $^{99}\text{Mo}/^{99\text{m}}\text{Tc}$ generator by Tucker and Greene who presented their findings at a 1958 American Nuclear Society meeting [8]. The general principle of the traditional $^{99}\text{Mo}/^{99\text{m}}\text{Tc}$ generator relies on adsorption of ^{99}Mo , in the form of $[\text{}^{99}\text{Mo}]\text{MoO}_4^{2-}$, onto an acidic alumina column. Upon decay, $[\text{}^{99\text{m}}\text{Tc}]\text{TcO}_4^-$ is formed, and may be eluted from the alumina column with saline [9].

Interestingly, the $^{99}\text{Mo}/^{99\text{m}}\text{Tc}$ generator was initially used for research unrelated to its now well-known application in the realm of nuclear medicine. For example, several $^{99}\text{Mo}/^{99\text{m}}\text{Tc}$ generators were supplied to industry for studies evaluating, for example, mixing efficiency [8]. Since the ^{99}Mo continuously decays to $^{99\text{m}}\text{Tc}$ with an 87.6% branching ratio [10] as shown in Figure 1-1, it is possible to periodically isolate the $^{99\text{m}}\text{Tc}$ from the ^{99}Mo and thus obtain a supply of $^{99\text{m}}\text{Tc}$ for a period of one to two weeks. It was not until 1960 that Richards suggested that $^{99\text{m}}\text{Tc}$ had desirable properties for diagnostic nuclear medicine studies, and it was soon thereafter that $^{99\text{m}}\text{Tc}$ made its debut in the field of medicine [8].

1.2. $^{99\text{m}}\text{Tc}$ in medicine

Diagnostic radiopharmaceuticals used in nuclear medicine image-based applications are comprised of a radionuclide either in the free state or incorporated into a larger molecule which selectively targets regions of interest in the body. Localization of the radiopharmaceutical following administration to the patient is determined using a detection system such as a gamma camera, PET, etc. tuned to the decay-mode of the radionuclide. Unlike CT or standard MRI techniques in which only anatomical information is obtained, imaging of the distribution of radiopharmaceutical uptake within a patient allows a clinician to evaluate dynamic physiological processes. Functional information such as the evaluation of blood flow or perfusion, metabolic activity, presence/absence of a

particular receptor for drug targeting, or clearance rates of the pharmaceutical within a particular organ, give diagnostic information which is not possible with anatomical imaging alone. This additional functional information lends further guidance to personalized disease management strategies, the ultimate goal of patient care.

^{99m}Tc , which until recently has been readily and reliably available, is a single-photon emitter with a 140 keV γ -ray and has many ideal characteristics for diagnostic nuclear medicine imaging. This 140 keV γ -ray energy is sufficiently high to achieve reasonable tissue penetration, but is sufficiently low so that it may be easily collimated for imaging purposes [11]. Due to the relatively low dosimetric burden and reasonably short half-life of ^{99m}Tc , higher count rates and therefore improved image signal can be achieved [8]. Furthermore, owing to technetium's versatile chemistry, a variety of ^{99m}Tc -radiopharmaceuticals can be prepared and used to evaluate different functional processes within the body.

When eluted from a generator, the recovered ^{99m}Tc product is in the form of pertechnetate, $[\text{}^{99m}\text{Tc}]\text{TcO}_4^-$. In this form, technetium is in its highest oxidation state of +7. Forming the basis for the first ^{99m}Tc nuclear medicine studies [8], $[\text{}^{99m}\text{Tc}]\text{TcO}_4^-$ has itself been used directly as a radiopharmaceutical, but this direct use of $[\text{}^{99m}\text{Tc}]\text{TcO}_4^-$ was limited to only a few applications such as thyroid imaging and imaging of blood brain barrier defects [1, 12]. Further investigation into ^{99m}Tc -labelled compounds was soon underway in order to image other functional processes. The pertechnetate anion is very stable in aqueous solution and is not chemically accessible for binding to chelating agents or directly to biological molecules [1, 11, 12, 13]. The formation of radiolabelled compounds through chelation involves the bonding of an electron-deficient metal to atoms or functional groups capable of donating electron pairs [1], and a lower oxidation state of technetium is required.

Many reducing agents, as well as electrolytic strategies have been investigated for the reduction of pertechnetate to a lower oxidation state [1, 11, 12]. Challenges noted include temperature and pH sensitivity which, if not

carefully controlled by the cumbersome use of pH meters, buffers, etc., may result in a mixture of oxidation states [1]. Introduction of the stannous ion in the early 1970's [11, 14, 15] as a reducing agent was a key development in ^{99m}Tc -radiopharmaceutical production. The addition of the stannous ion induces a redox reaction whereby the tin is oxidized to the stannic ion, and the technetium is reduced to a lower oxidation state which is more reactive and suitable for labelling. The stannous ion allows for reduction at room temperature in a wide pH range of 4–7 [11], and is further preferred for its practical benefits such as water solubility, stability, and low toxicity [1].

Use of the stannous ion led to development of “instant kits” which greatly eased preparation of ^{99m}Tc -radiopharmaceuticals. In these kits, all non-radioactive components could be premixed in a single vial prior to addition of pertechnetate, and there was no need for additional chemicals post-labelling [14]. With the availability of the $^{99}\text{Mo}/^{99m}\text{Tc}$ generator, and the advent of easy labelling systems using stannous ion based instant kits, the use of ^{99m}Tc -labelled radiopharmaceuticals expanded rapidly [11].

Oxygen presence in the vial or oxidants formed following self-radiolysis within the vial solution may both contribute towards consumption of the stannous reductant [1]. If the stannous ion is depleted, then any reoxidation of a kinetically unstable molecule to pertechnetate will be irreversible. While this may be circumvented by adding large excesses of stannous ion, in some pharmaceuticals, large excesses of reductant may affect the biological performance [1]. In the labelling of molecules where minimal levels of stannous ion must be used, excess amounts of carrier technetium, ^{99g}Tc , have been noted to have adverse effects on the labelling [1]. That said, a contrasting study by Urbano et al. [16] has reported adequate labelling over a range of ^{99g}Tc concentrations for a variety of radiopharmaceuticals with low stannous content including, for example, hexamethylpropyleneamine oxime (HM-PAO), mercaptoacetyltriglycine (MAG3), or methoxyisobutylisonitrile (MIBI). These conflicting results suggest

that further investigation regarding the labelling efficiency of low specific activity ^{99m}Tc may be warranted.

As described by Nowotnik [1], some of the earliest nuclear medicine studies with reduced ^{99m}Tc used metal complexing compounds which were well established in chemistry. These studies included synthesis of ^{99m}Tc complexes of carbohydrate acids, gluconate, glucoheptonate, and dimercapto-succinic acid for kidney imaging; complexes of phosphonates such as methylene diphosphonate (MDP) for bone imaging; and the complex of diethylenetriaminepentaacetic acid (DTPA) for renal function imaging. One of the first ligands designed specifically for technetium labelling resulted in the hepatobiliary imaging agent, hepatobiliary iminodiacetic acid (HIDA) in 1976 [1]. Iminodiacetic acid was used in this pharmaceutical acid as a bifunctional chelate to connect ^{99m}Tc with lidocaine [17].

Despite the ongoing developments in technetium coordination chemistry, little was known about the nature of the labelled complexes and a better understanding of the chemistry was necessary [1]. Since no stable technetium could be used for this application, the first technetium crystal structure characterizations of potential pharmaceuticals were presented in 1978 using the long-lived ^{99g}Tc [11]. Throughout the 1980s, several further ^{99m}Tc -labelled compounds were developed for nuclear medicine applications including HM-PAO and ethylcysteinate dimer (ECD) for cerebral perfusion imaging, MAG3 for renal function imaging, and MIBI for myocardial perfusion imaging. Although the majority of ^{99m}Tc -pharmaceuticals used today were developed more than twenty years ago, additional ^{99m}Tc -radiopharmaceutical have been described for imaging of a variety of organ and systems including for example, bone, liver/hepatobiliary, lungs, brain myocardium, gall bladder, kidneys, tumours, and blood cells. For a discussion both of standard labelling schemes as well as ongoing research and developments of ^{99m}Tc -radiopharmaceuticals, readers are referred to the following reviews [12, 18, 19, 20, 21].

The overall ease of availability, ease of chemical labelling, versatile chemistry, low dose, capability of providing functional information for a wide

variety of organs, clinician familiarity in analysis of images, etc. have all contributed towards ^{99m}Tc emerging as the most widely used radionuclide in diagnostic nuclear medicine [18, 22]. Of these, myocardial perfusion (56%), bone scans (17%), and liver/hepatobiliary (7%) studies comprise the three dominant ^{99m}Tc -procedures [23]. Approximately 30 million procedures using ^{99m}Tc -radiopharmaceuticals are performed worldwide annually, and it is projected that this figure will increase at a rate of 3–10% per year [23]. With recent shortages in the reactor-based supply chain of ^{99m}Tc however, the reliable supply of this key medical isotope has been compromised.

1.3. Reactor-based production of ^{99m}Tc

Despite the early research which used cyclotrons to study technetium, ^{99m}Tc is, at present, exclusively obtained using nuclear reactor-based production strategies. This strategy is well established, it allows for production of the long-lived ^{99}Mo for a two week supply of high radiochemical purity ^{99m}Tc , and until recent years, the reactor-based supply chain has been quite reliable.

Two reactor-based ^{99}Mo production methods exist; $^{98}\text{Mo}(n,\gamma)^{99}\text{Mo}\rightarrow^{99m}\text{Tc}$ and $^{235}\text{U}(n,f)^{99}\text{Mo}\rightarrow^{99m}\text{Tc}$. In the former neutron-capture scheme, since both the target material and final product are chemically identical species, these components cannot be separated, and the final ^{99}Mo consists of a large quantity of bulk chemical molybdenum. In contrast, the latter reaction scheme entails the irradiation of targets enriched in ^{235}U which results in ^{99}Mo production with a 6% fission yield [24]. Upon significant chemical processing, the desired ^{99}Mo is isolated in a no-carrier-added form. Thus, the major difference in the neutron-capture based ^{99}Mo product and the fission-based ^{99}Mo product is the quantity of chemical molybdenum present.

This difference in chemical molybdenum content is of importance when considering the $^{99}\text{Mo}/^{99m}\text{Tc}$ chemical extraction strategies. Evaluating the standard acidic alumina generator extraction, the maximum room temperature adsorption is reported to be 20–25 mg of molybdenum per gram of alumina [25].

Since the alumina generator extraction scheme relies on efficient immobilization of the molybdenum, the total amount of chemical molybdenum is thus a limiting factor in construction of an alumina generator. If the chemical molybdenum quantities are on the order of hundreds of milligrams, very large alumina columns are required. In turn, excessively large volumes of saline are needed to achieve efficient generator elution, and the concentration of the resulting pertechnetate solution might be too low for practical clinical applications [25].

Of the two reactor-based strategies, the fission based ^{99}Mo production scheme is amenable to $^{99\text{m}}\text{Tc}$ extraction using the traditional acidic alumina generator. A variety of modified strategies for extracting $^{99\text{m}}\text{Tc}$ from bulk chemical molybdenum of the neutron capture based strategy have been developed and include high-temperature alumina column preparation [25], zirconium molybdate gel generator [25], biphasic extraction chromatography [26], sublimation [27], liquid-liquid extraction [28], etc. Since the neutron-capture extraction schemes are generally more elaborate than the traditional alumina-based generator used for fission- ^{99}Mo , it is not surprising that all major generator manufacturers produce $^{99}\text{Mo}/^{99\text{m}}\text{Tc}$ using the ^{235}U fission-based reaction scheme.

1.4. Current $^{99\text{m}}\text{Tc}$ supply challenges

In recent reports [23, 29], it was summarized that ^{99}Mo obtained from the fissioning of ^{235}U is principally produced from one of the five government-owned and funded multi-purpose reactors shown in Table 1-1.

As noted in Table 1-1, the worldwide supply of $^{99}\text{Mo}/^{99\text{m}}\text{Tc}$ is highly dependent on a limited number of ageing research/test reactors. Since this ageing infrastructure has required ever growing shutdown periods for maintenance and repair, the supply of $^{99}\text{Mo}/^{99\text{m}}\text{Tc}$ has become more fragile. Canada's current facility, the National Research Universal (NRU) reactor in Chalk River has the capacity to produce 40–50% of the world's supply of ^{99}Mo [31]. As a dominant producer of ^{99}Mo , Canada realized the need for development of new reactor infrastructure and began construction of the MAPLE reactors in the late 1990's.

As a replacement to the NRU reactor, these two reactors were designed for the purpose of meeting the worldwide isotope requirements twice-over [23]. With the projected impact of the MAPLE reactors, there was no anticipated need to further develop alternative global production facilities.

Table 1-1. Summary of reactors and 2008 market shares for commercial production of ^{99}Mo [23, 29].

Reactor	Location	Commissioning Date	Reactor Category	Market Share [%]
NRU	Canada	1957	Research	31
BR2	Belgium	1961	Test	10
HFR Petten	Netherlands	1961	Test	33
OSIRIS	France	1966	Research	8
SAFARI-1	South Africa	1965	Research	13
Other	–	–	–	5

Owing to years of ongoing technical difficulties during reactor commissioning however, the MAPLE reactor project was eventually cancelled in June of 2008 [30]. Plans for new production facilities in other countries have also been slow to materialize as it was assumed that the Canadian MAPLE reactors would eventually be operational [23]. Canada has consequently been forced to continue to rely on its ever ageing NRU reactor for production of ^{99}Mo .

While the supply chain of $^{99}\text{Mo}/^{99\text{m}}\text{Tc}$ has, in general, been quite reliable, serious supply interruptions have been observed over the past three years. The scheduled maintenance shutdown of Canada's NRU reactor in 2007 along with both scheduled and unscheduled interruptions at other reactor facilities resulted in a world-wide shortage of nuclear medicine isotopes in 2008 [32]. This shortage resumed soon thereafter as Canada's NRU reactor was once again shutdown for safety reasons for a period of 15 months starting in May of 2009 following the discovery of a small heavy water leak.

Adding additional supply challenges to the standard reactor-based production of ^{99m}Tc is the fact that, except for South Africa, the major $^{99}\text{Mo}/^{99m}\text{Tc}$ manufacturers of Table 1-1 use 93% enrichment for their ^{235}U target material, while South Africa uses 45% [29]. Natural abundance uranium typically contains about 0.7% of ^{235}U and 99.3% ^{238}U [29]. As a ^{235}U enrichment great than 20% is considered highly enriched uranium (HEU), for nuclear non-proliferation purposes, there is a global pressure towards using targets made from low enriched uranium (LEU), or less than 20% ^{235}U by weight of uranium. Supporting this movement, in November of 2009, legislation was passed by the US House of Representatives which would eliminate the US export of HEU for isotope production in Canada within a period of 7 to 10 years [33].

While several regional producers of ^{99}Mo use LEU targets, including for example, the RA-3 reactor in Argentina or the OPAL reactor in Australia [29], the conversion to LEU targets poses a challenge. For example, if the LEU targets simply replace HEU targets, approximately five-times as many targets need to be irradiated to achieve the same yield. While targets could instead be made larger, reactor space limitations may preclude such an option. Research is thus currently underway to alter the composition of LEU targets for the purpose of increasing the density of the ^{235}U [29]. As noted in a recent report by the Nuclear Energy Agency [34], increased waste is expected with LEU-based targets. For example, although it will depend on the type of target, 215 kg LEU uranium waste vs. 43 kg of HEU waste and 25 g of ^{239}Pu for LEU vs. 1.2g ^{239}Pu for HEU are estimated annually for 20% enriched vs. 93% enriched targets, respectively. It is further noted that LEU processed targets will yield increased volumes of intermediate and low-level liquid waste in comparison to HEU strategies [34].

Research is therefore underway to yield more efficient LEU target designs [29]. Furthermore, existing test/research reactors as well as power reactors [35] are being considered and/or have recently been approved for production of ^{99}Mo . Examples include the MURR reactor in the USA, and the MARIA reactor in Poland [29]. Nevertheless, the growing demand for ^{99m}Tc -radiopharmaceuticals

[18, 23] leaves concern with regards to sustaining a long-term reliable source of $^{99}\text{Mo}/^{99\text{m}}\text{Tc}$. This has prompted recent interest in exploring alternative strategies which could result in the large-scale supply of $^{99\text{m}}\text{Tc}$.

1.5. Alternative production strategies

Although alternative strategies for $^{99}\text{Mo}/^{99\text{m}}\text{Tc}$ production have been discussed previously including Beaver and Hupf's cyclotron based strategy proposed in 1971 [36], or the IAEA's technical document on alternative production strategies published in 1999 [37], the development of alternative large-scale production strategies appears to have only gained global interest following the recent interruptions in the availability of reactor-based $^{99\text{m}}\text{Tc}$. Examples of alternative reaction schemes include, but are not limited to, the $^{100}\text{Mo}(p,2n)^{99\text{m}}\text{Tc}$, $^{100}\text{Mo}(\gamma,n)^{99}\text{Mo}$, $^{238}\text{U}(\gamma,f)^{99}\text{Mo}$, and $^{100}\text{Mo}(n,2n)^{99}\text{Mo}$ reactions. Details regarding an array of alternative reaction schemes are summarized in several recent publications [23, 24, 34, 38, 39].

As a world-leader in the supply of $^{99}\text{Mo}/^{99\text{m}}\text{Tc}$, Canada was eager to seek out alternative $^{99}\text{Mo}/^{99\text{m}}\text{Tc}$ production strategies. In June of 2009, an expert review panel was established for the purposes of advising the Government of Canada on the most viable strategies for maintaining a reliable supply of $^{99\text{m}}\text{Tc}$ in the medium to long-term [23]. Many technologies were investigated, and the panel made three technology-specific recommendations including: (i) making policy decisions on the requirement for a new research reactor, (ii) supporting a research and development program for cyclotron-based $^{99\text{m}}\text{Tc}$ production, and (iii) achieving better use of $^{99\text{m}}\text{Tc}$ supply through advanced medical imaging technologies. With these recommendations forming the basis for the Non-reactor-based Isotope Supply Contribution Program (NISP), the Government of Canada committed \$35M to funding four projects to investigate non-reactor-based production of $^{99\text{m}}\text{Tc}$. Two of these projects use linear accelerators to produce ^{99}Mo via the $^{100}\text{Mo}(\gamma,n)^{99}\text{Mo}$ reaction. In this scheme, the linear accelerator is used to accelerate electrons onto a high-Z target which subsequently produces the

necessary Bremsstrahlung photons for irradiation of the ^{100}Mo target. In contrast, the remaining two projects use cyclotrons for the direct production of $^{99\text{m}}\text{Tc}$ via the $^{100}\text{Mo}(p,2n)^{99\text{m}}\text{Tc}$ reaction. This dissertation focuses on technical challenges related to the direct cyclotron-based production scheme.

1.6. Cyclotron production of technetium

Cyclotron production of technetium is not a new concept. As noted above, E. O. Lawrence's cyclotron-based deuteron irradiation of molybdenum led to discovery of "Element 43" [3]. The cyclotron-based production of $^{99\text{m}}\text{Tc}$ for nuclear medicine using the $^{100}\text{Mo}(p,2n)^{99\text{m}}\text{Tc}$ reaction was proposed by Beaver and Hupf forty years ago [36], but has never been used for production of large quantities of $^{99\text{m}}\text{Tc}$. Cyclotron-produced $^{99\text{m}}\text{Tc}$ has never been used clinically, and the first animal studies were only presented in 2010 [39].

The use of cyclotron produced technetium is, however, not foreign to nuclear medicine. Technetium-94m ($^{94\text{m}}\text{Tc}$) is another radioisotope which has gained popularity over the past two decades [13]. Unlike $^{99\text{m}}\text{Tc}$, $^{94\text{m}}\text{Tc}$ with a half-life, $t_{1/2}$, of 52 minutes is a positron emitting isotope with a positron branching ratio of 70%. $^{94\text{m}}\text{Tc}$ is used with the nuclear medicine imaging technique of positron emission tomography or PET; an imaging strategy which makes use of the back-to-back annihilation photons that arise during the decay of positron emitting isotopes. While several reaction schemes are possible, the standard production strategy for $^{94\text{m}}\text{Tc}$ is through the use of a cyclotron via the $^{94}\text{Mo}(p,n)^{94\text{m}}\text{Tc}$ reaction.

The cyclotron production of $^{99\text{m}}\text{Tc}$ and $^{94\text{m}}\text{Tc}$ are similar in that $^{99\text{m}}\text{Tc}$ production entails the proton irradiation of enriched ^{100}Mo , whereas $^{94\text{m}}\text{Tc}$ production entails the proton irradiation of enriched ^{94}Mo . That said, the technology is not directly transferrable as $^{94\text{m}}\text{Tc}$ has only ever been produced on a small scale (e.g. typical beam currents of 5 μA [13]) using oxide-based targets. Large scale production of technetium poses many new challenges. First, with the large power deposition into the target during irradiation, the poor thermal

conductivity and the low melting point of 795 °C for existing molybdenum oxide targets severely limits the amount of beam current that can be applied. It would thus appear that only metallic molybdenum targets will be amenable to the high currents of 100–500 μA needed for the large-scale production of $^{99\text{m}}\text{Tc}$. Next, while the oxide-based targets used for $^{94\text{m}}\text{Tc}$ production allowed for straightforward recycling of the enriched and expensive ^{94}Mo target material, by moving away from oxide-based targets for large-scale $^{99\text{m}}\text{Tc}$ production, new strategies for recycling of the enriched metallic ^{100}Mo need to be developed. An additional factor which must also be addressed with regards to the cyclotron-based production of $^{99\text{m}}\text{Tc}$ is how the quality of the cyclotron-based product compares to that of the long-standing reactor-based $^{99}\text{Mo} \rightarrow ^{99\text{m}}\text{Tc}$ production strategies.

1.7. Thesis overview

As a starting point to understanding the current status of cyclotron production of technetium by irradiation of molybdenum, Chapter 2 of this dissertation reviews the present strategies for cyclotron production of $^{94\text{m}}\text{Tc}$. To predict $^{99\text{m}}\text{Tc}$ yields, excitation functions for the $^{100}\text{Mo}(\text{p},2\text{n})^{99\text{m}}\text{Tc}$ and $^{100}\text{Mo}(\text{p},\text{x})^{99}\text{Mo}$ reactions are presented in Chapter 3 along with a comparison to previously published values. The first experimental measurement of the $^{100}\text{Mo}(\text{p},2\text{n})^{99\text{g}}\text{Tc}$ excitation function is also presented in this chapter. Since these above reactions are energy dependent, knowledge of these excitation functions will allow for selection of an optimal irradiation time and energy depending on the tolerable level of $^{99\text{g}}\text{Tc}$, desired yields, etc. A simple strategy for experimental measurement of the proton energy of a cyclotron is presented in Chapter 4. Considering the molybdenum itself, Chapter 5 evaluates a strategy for recycling of metallic ^{100}Mo following extraction of $^{99\text{m}}\text{Tc}$. While the initial studies of Chapter 5 were performed at low currents using pressed ^{100}Mo metal powder, striving for Curie quantity production of $^{99\text{m}}\text{Tc}$, Chapter 6 describes a method for preparing metallic ^{100}Mo targets capable of tolerating beam powers in excess of 1 kW. With the goal of using the cyclotron-produced $^{99\text{m}}\text{Tc}$ clinically, Chapter 7

discusses aspects of the quality of cyclotron-produced ^{99m}Tc including animal biodistribution studies with $[\text{}^{99m}\text{Tc}]\text{TcO}_4^-$ and $[\text{}^{99m}\text{Tc}]\text{disofenin}$. Finally, using the strategies and results presented throughout this dissertation, Chapter 8 concludes by presenting preliminary results obtained as part of a Phase I Clinical Trial [40] with cyclotron-produced $[\text{}^{99m}\text{Tc}]\text{TcO}_4^-$. Future areas of research related to the cyclotron production of ^{99m}Tc are also discussed.

1.8. References

1. D.P. Nowotnik, Physico-Chemical concepts in the preparation of technetium radiopharmaceuticals in Textbook of Radiopharmacy, Theory and Practice, Ed: C.B. Sampson, Gordon and Breach Science Publishers, (1990) 53–72.
2. M. Weeks, The discovery of the elements – chronology, J. Chem. Educ. 10 (1933) 223–227.
3. C. Perrier, E. Segrè, Some chemical properties of element 43, J. Chem. Phys. 5 (1937) 712–716.
4. G.T. Seaborg, E. Segrè, Nuclear isomerism in element 43, Phys. Rev. 55 (1939) 808–814.
5. E. Segrè, C.S. Wu, Some fission products of uranium, Phys. Rev. 57 (1940) 552–552.
6. G.E. Boyd, J.R. Sites, Q.V. Larson, C.R. Baldock, Production and identification of long-lived technetium isotopes at masses 97, 98, and 99, Phys. Rev. 99 (1955) 1030–1031.
7. E. Anders, The radiochemistry of technetium, National Research Council, Nuclear Science Series, NAS-NS #3021, (1960).

8. P. Richards, Technetium-99m: The early days, Brookhaven National Lab Report # 43197, (1989), <http://www.osti.gov/bridge/servlets/purl/5612212-IkoOXX/5612212.pdf> (accessed 2011).
9. A.T. Elliott, Radionuclide Generators in Textbook of Radiopharmacy, Theory and Practice, Ed: C.B. Sampson, Gordon and Breach Science Publishers, (1990) 33–51.
10. Z. Alfassi, F. Groppi, M. Bonardi, J. Goeij, On the “artificial” nature of Tc and the “carrier-free” nature of ^{99m}Tc from $^{99}\text{Mo}/^{99m}\text{Tc}$ generators, Appl. Radiat. Isot. 63 (2005) 37–40.
11. W. Eckelman, Unparalleled contribution of technetium-99m to medicine over 5 decades, J. Am. Coll. Cardiol. Img. 2 (2009) 364–368.
12. K. Schwochau, Technetium – Chemistry and Radiopharmaceutical Applications, Wiley-VCH, Weinheim, Germany (2000).
13. K. Gagnon, S. McQuarrie, D. Abrams, A.J.B. McEwan, F. Wuest, Radiotracers based on technetium-94m, Current Radiopharmaceuticals 4 (2011) 90–101.
14. W. Eckelman, P. Richards, Instant ^{99m}Tc -DTPA, J. Nucl. Med. 11 (1970) 761.
15. W. Eckelman, P. Richards, W. Hauser, H. Atkins, Technetium-labeled red blood cells, J. Nucl. Med. 12 (1971) 22–24.

16. N. Urbano, S. Modoni, M. Guerra, M. Chinol, Evaluation of fresh and old eluate of $^{99}\text{Mo}/^{99\text{m}}\text{Tc}$ generators used for labeling of different pharmaceutical kits, *J. Radioanal. Nucl. Chem.* 265 (2005) 7–10.
17. G.T. Krishnamurthy, S. Krishnamurthy, *Nuclear hepatology: A textbook of hepatobiliary diseases*, 2nd Ed. Springer-Verlag, Berlin, (2009).
18. Technetium-99m radiopharmaceuticals: Manufacture of kits. IAEA Technical Report Series No. 466, IAEA, Vienna, (2008).
19. Technetium-99m radiopharmaceuticals: Status and trends. IAEA Radioisotope and Radiopharmaceuticals Series No. 1, IAEA, Vienna, (2009).
20. Y. Arano, Recent advances in $^{99\text{m}}\text{Tc}$ radiopharmaceuticals, *Annl. Nucl. Med.* 16 (2002) 79–93.
21. G. Bandoli, F. Tisato, A. Dolmella, S. Agostini, Structural overview of technetium compounds (2000-2004). *Coord. Chem. Rev.* 250 (2006) 561–573.
22. T.J. Ruth, The uses of radiotracers in the life sciences, *Rep. Prog. Phys.* 72 (2009) 016701.
23. Report of the expert review panel on medical isotope production, Presented to the Minister of Natural Resources Canada, 30 November, (2009), <http://www.nrcan.gc.ca/eneene/sources/uranuc/pdf/panrep-rapexp-eng.pdf> (accessed 2011).
24. Making medical isotopes: Report of the task force on alternatives for medical-isotope production, TRIUMF, University of British Columbia,

Advanced Applied Physics Solutions with support from Natural Resources Canada, (2008) <http://www.triumf.ca/sites/default/files/Making-Medical-Isotopes.pdf> (accessed 2011).

25. M. Asif, A. Mushtaq, Evaluation of highly loaded low specific activity ^{99}Mo on alumina column as $^{99\text{m}}\text{Tc}$ generator, *J. Radioanal. Nucl. Chem.* 284 (2010) 439–442.
26. D.R. McAlister, E.P. Horwitz, Automated two column generator systems for medical radionuclides, *Appl. Radiat. Isot.* 67 (2009) 1985–1991.
27. J.D. Christian, D.A. Petti, R.J. Kirkham, R.G. Bennett, Advances in Sublimation separation of technetium from low-specific-activity molybdenum-99, *Ind. Eng. Chem. Res.* 39 (2000) 3157–3168.
28. S. Chattopadhyay, S.S. Das, L. Barua, A simple rapid technique for recovery of $^{99\text{m}}\text{Tc}$ from low specific activity $(n,\gamma)^{99}\text{Mo}$ based on solvent extraction and column chromatography, *Appl. Radiat. Isot.* 68 (2010) 1–4.
29. Nuclear and Radiation Studies Board – Division of Earth and Life Sciences, Medical isotope production without highly enriched uranium, The National Academies Press, Washington, DC, (2009).
30. T. J. Ruth, Accelerating production of medical isotopes, *Nature*, 457 (2009) 536–537.
31. D. Lewis, ^{99}Mo supply—the times they are a-changing, *Eur. J. Nucl. Med. Mol. Imaging.* 36 (2009) 1371–1374.
32. N. Knight, Return of the radionuclide shortage, *J. Nucl. Med.* 50 (2009) 13N–14N.

33. American Medical Isotope Production Act of 2009. 111th Congress, 1st Session, HR 3276, US House of Representatives, (2009). http://hps.org/govtreations/documents/house_hr3276_isotope-production.pdf (accessed 2011).
34. The supply of medical radioisotopes: Review of potential Molybdenum-99/Techneium-99m production technologies, Nuclear Energy Agency, Organisation for Economic Co-Operation and Development, (2010) <http://www.oecd-nea.org/med-radio/reports/Med-Radio-99Mo-Prod-Tech.pdf> (accessed 2011).
35. A.C. Morreale, D.R. Novog, J.C. Luxat, A strategy for intensive production of molybdenum-99 isotopes for nuclear medicine using CANDU reactors, *Appl. Radiat. Isot.* doi:10.1016/j.apradiso.2011.07.007, In Press, (2011).
36. J. Beaver, H. Hupf, Production of ^{99m}Tc on a medical cyclotron: A feasibility study, *J. Nucl. Med.* 12 (1971) 739–741.
37. Production technologies for molybdenum-99 and technetium-99m, TECDOC-1065, IAEA, Vienna, (1999).
38. C. Ross, R. Galea, P. Saull, W. Davidson, P. Brown, D. Brown, J. Harvey, G. Messina, R. Wassenaar, M. de Jong, Using the ¹⁰⁰Mo photoneutron reaction to meet Canada's requirement for ^{99m}Tc, *La Physique au Canada*, 66 (2010) 19–24.
39. B. Guérin, S. Tremblay, S. Rodrigue, J.A. Rousseau, V. Dumulon-Perreault, R. Lecomte, J.E. van Lier, A. Zyuzin, E.J. van Lier, Cyclotron production of ^{99m}Tc: An approach to the medical isotope crisis, *J. Nucl. Med.* 51 (2010) 13N–16N.

40. A Prospective Phase I Study of Cyclotron-Produced Tc-99m Pertechnetate (CPERT) in Patients With Thyroid Cancer. ClinicalTrials.gov Identifier: NCT01437254, <http://www.clinicaltrials.gov/ct2/show/NCT01437254?term=cyclotron&rank=1> (accessed 2011).

2. A starting point – Cyclotron production of ^{94m}Tc

A version of this chapter was published as a section in:

K. Gagnon, S. McQuarrie, D. Abrams, A. J. B. McEwan and F. Wuest, Radiotracers based on technetium-94m, *Current Radiopharmaceuticals*, 4 (2011) 90–101.

2.1. Introduction

While the standard production method for ^{99m}Tc does not currently use the $^{100}\text{Mo}(p,2n)^{99m}\text{Tc}$ reaction scheme, the standard technique for the clinically-relevant ^{94m}Tc is, in contrast, based on the cyclotron irradiation of enriched ^{94}Mo . In considering the cyclotron production of ^{99m}Tc , existing ^{94m}Tc production strategies must be evaluated to determine if these techniques might be applicable to the cyclotron production of ^{99m}Tc . Therefore, the goal of this chapter is to establish the current status of cyclotron produced technetium by reviewing the existing cyclotron-based ^{94m}Tc production strategies.

2.2. ^{94m}Tc as an alternative to ^{99m}Tc

For decades, ^{99m}Tc has dominated radionuclide molecular imaging as the workhorse of nuclear medicine. The physical characteristics ($t_{1/2} = 6.0$ hr, $E_{\gamma} = 140.5$ keV) and its widespread availability through the $^{99}\text{Mo}/^{99m}\text{Tc}$ generator system make the γ -emitting ^{99m}Tc an ideal radionuclide for single-photon emission computed tomography (SPECT). Recent progress in technetium coordination and radiopharmaceutical chemistry, as well as SPECT molecular imaging techniques, has significantly broadened ^{99m}Tc applications in biomedical research and nuclear medicine. However, quantitative investigation of the

physiological mechanisms of radiopharmaceuticals labelled with the γ -emitting ^{99m}Tc by means of SPECT is challenging. Compared to SPECT, positron emission tomography (PET) provides higher sensitivity, superior spatial resolution, and improved activity quantitation. In recent years, PET has become a powerful non-invasive molecular imaging technique which provides functional information regarding physiological, biochemical and pharmacological processes in laboratory animals and humans. The possibility of observing molecular interactions in living organisms and determining absolute values of physiological parameters places PET in a unique position among other molecular imaging techniques. Therefore, it would be meaningful to use PET imaging with a positron-emitting technetium isotope to quantify the biodistribution of respective ^{99m}Tc -radiopharmaceuticals in animals and humans.

Technetium-94m (^{94m}Tc) is a cyclotron-produced positron-emitting technetium isotope with a 52 minute physical half-life with $E_{\beta+\text{max}}$ of 2.44 MeV. With its relatively high positron branching of 70% and the fact that ^{94m}Tc shares the same well-established coordination chemistry as ^{99m}Tc , this radionuclide is a suitable candidate for the synthesis of technetium-based radiopharmaceuticals for PET imaging.

The present review gives a survey on the production schemes, target design strategies, and extraction strategies of ^{94m}Tc as a non-conventional positron emitting radionuclide for PET molecular imaging. A more thorough discussion of ^{94m}Tc imaging challenges and a review of radiopharmaceutical labelling strategies is presented in the complete review article noted above [1].

2.3. Production and processing of ^{94m}Tc

2.3.1. ^{94m}Tc Production

To produce ^{94m}Tc , a selection of reaction schemes on molybdenum targets has been studied. These include, but are not limited to, $^{94}\text{Mo}(p,n)^{94m}\text{Tc}$ [2, 3, 4, 5, 6, 7], $^{94}\text{Mo}(d,2n)^{94m}\text{Tc}$ [8, 9, 10, 11], $^{92}\text{Mo}(\alpha,pn)^{94m}\text{Tc}$ [12, 13], and $^{92}\text{Mo}(\alpha,2n)^{94}\text{Ru} \rightarrow ^{94m}\text{Tc}$ [4, 13]. When selecting a nuclear reaction for the

production of ^{94m}Tc , parameters to consider include the purity, yield, material costs, and access to projectiles such as p, d, α , etc. of an appropriate energy and intensity.

Discussing impurities, we use as an example the $^{94}\text{Mo}(p,n)^{94m}\text{Tc}$ reaction to demonstrate that impurities may arise from two sources. First, we note that natural abundance molybdenum is comprised of the following seven stable isotopes: 14.84% ^{92}Mo , 9.25% ^{94}Mo , 15.92% ^{95}Mo , 16.68% ^{96}Mo , 9.55% ^{97}Mo , 24.13% ^{98}Mo , and 9.63% ^{100}Mo . Considering the relatively low natural abundance of ^{94}Mo , nuclear reactions with the $A \neq 94$ molybdenum isotopes will give rise to contaminant technetium. With half-lives ranging from 4 minutes to 61 days, Christian et al. [4] list ^{92g}Tc , ^{94g}Tc , ^{95g}Tc , ^{95m}Tc , ^{96g}Tc , and ^{99m}Tc as the six major technetium contaminants which occur following irradiation of natural abundance molybdenum, $^{\text{nat}}\text{Mo}$, at 11 MeV. When purity is of importance for decreasing patient dose, these sources of contamination may be mitigated by employing isotopically enriched molybdenum. The use of enriched molybdenum provides the additional benefit of increased ^{94m}Tc production yields.

As a second potential source of contaminants, we note that even for a 100% enriched ^{94}Mo target, competing reactions may nevertheless give rise to undesired technetium contaminants. These competing reactions may, for example, include $^{94}\text{Mo}(p,n)^{94g}\text{Tc}$, $^{94}\text{Mo}(p,2n)^{93m}\text{Tc}$, or $^{94}\text{Mo}(p,2n)^{93g}\text{Tc}$. As each of these reactions depends on the proton energy, this source of contaminants may be minimized, although not eliminated, through optimal selection of the irradiation energy window and irradiation time. As an example, Rösch et al. [3] suggest an optimal proton energy window of 13→7 MeV for this reaction and Nickles et al. [14] limit the irradiation time to one half-life.

While the use of enriched molybdenum is essential when high purity ^{94m}Tc is desired, the increased costs associated with using enriched material imposes the necessity of target recycling. For example, an increase from approximately \$0.08 to \$1500 for 250 mg is noted by Smith et al. [15] for ^{94}Mo . To decrease target costs, several studies have examined ^{94m}Tc production using the

$^{93}\text{Nb}(^3\text{He},2\text{n})^{94\text{m}}\text{Tc}$ [4, 16, 17, 18], and $^{93}\text{Nb}(\alpha,3\text{n})^{94\text{m}}\text{Tc}$ [4, 8, 19, 20, 21, 22] reactions. As niobium is a naturally mono-isotopic element, the first source of impurities noted above is eliminated. Impurities resulting from competing energy-dependent reactions following the irradiation of niobium must however still be considered. As indicated by Faßbender et al. [18], when considering material costs, readers are reminded that the price of ^3He must also be taken into account.

A selection of published yields and impurities is given in Table 2-1. Examining these values, we note that the $^{94}\text{Mo}(\text{p},\text{n})^{94\text{m}}\text{Tc}$ reaction stands out as having a high yield and reasonable radionuclidic purity. Furthermore, this reaction scheme is perhaps the most widely accessible reaction as it may be achieved on a small medical cyclotron. For these reasons, it is of little surprise that the $^{94}\text{Mo}(\text{p},\text{n})^{94\text{m}}\text{Tc}$ reaction is the most widely reported production strategy. Although less accessible given that most medical cyclotrons are limited to proton and sometimes deuteron irradiation, we note that the $^{92}\text{Mo}(\alpha,2\text{n})^{94}\text{Ru} \rightarrow ^{94\text{m}}\text{Tc}$ generator production route is a clever production scheme whereby $^{94\text{m}}\text{Tc}$ of the highest purity may be achieved as ^{94}Ru selectively decays to the $^{94\text{m}}\text{Tc}$ metastable isomer [13].

While efforts to investigate $^{94\text{m}}\text{Tc}$ production using the low-cost mono-isotopic niobium are certainly a worthwhile endeavour, the low yields, high impurity levels from competing reaction pathways, and limited access to ^3He and α as projectiles deter the use of niobium as a target material for $^{94\text{m}}\text{Tc}$ production. We have therefore limited this following discussion on target preparation and processing to molybdenum targets. Readers interested in the extraction of $^{94\text{m}}\text{Tc}$ from niobium targets are referred to Matuszek et al. [8] and Faßbender et al. [18].

Table 2-1. Selection of published data on ^{94m}Tc production.

Reaction	Energy ^a [MeV]	Enrich- ment [%]	Yield [MBq/ μAh]	Impurities [%]	Reference
$^{94}\text{Mo}(\text{p},\text{n})^{94m}\text{Tc}$	13→7	93.9	2000	^{93m}Tc (0.04), $^{93m,g}\text{Tc}$ (0.17), ^{94g}Tc (5.5)	[3]
	11	Nat	141	^{92}Tc (53), ^{94g}Tc (8.7), ^{95m}Tc (0.04), ^{95g}Tc (8.9), ^{96g}Tc (2.3)	[14] ^b
	13.8	91–94	--	^{93}Tc (3.3 ± 2.4), ^{94g}Tc (10.0 ± 1.5), ^{95}Tc (0.3 ± 0.1)	[15]
	13.8	Nat	--	^{93}Tc (1.4 ± 0.6), ^{94g}Tc (10.1 ± 0.8), ^{95}Tc (11.0 ± 0.6), ^{96m}Tc (255.8 ± 28.2), ^{96g}Tc (1.5 ± 1.4), ^{99m}Tc (7.2 ± 0.4)	[15]
	14.7	91.0	1295	^{94g}Tc (< 7), All other impurities (< 0.4)	[23]
	≤ 13	91.01	1000 ± 100	^{94g}Tc (5.9), ^{95m}Tc (0.27), ^{95g}Tc (0.002), ^{96g}Tc (0.01)	[24]
$^{94}\text{Mo}(\text{d},2\text{n})^{94m}\text{Tc}$	11.7	Nat	28	^{93m}Tc (86), ^{93g}Tc (90), ^{94g}Tc (20), ^{95g}Tc (56), ^{96g}Tc (12), ^{99m}Tc (25), ^{101}Tc (439)	[9] ^b
	17→12	100 ^c	2435	--	[10] ^b
$^{92}\text{Mo}(\alpha,\text{pn})^{94m}\text{Tc}$	26→18	97.37	98 ^d	^{94g}Tc (30)	[13]
$^{92}\text{Mo}(\alpha,2\text{n})^{94}\text{Ru} \rightarrow ^{94m}\text{Tc}$	26→18	97.37	35	Not relevant at EOB, however ^{95g}Tc (7) noted after 90 min due to coproduced ^{95}Ru .	[13]
$^{93}\text{Nb}(\text{}^3\text{He},2\text{n})^{94m}\text{Tc}$	18→10	Nat/100	33	^{94g}Tc (25), $^{93,95,96}\text{Tc}$ (14)	[18]
	53	Nat/100	93	^{94g}Tc (63)	[4] ^a
$^{93}\text{Nb}(\alpha,3\text{n})^{94m}\text{Tc}$	39	Nat/100	42	^{94g}Tc (127), ^{95g}Tc (128), ^{96}Tc (6)	[4] ^a

^a The arrow denotes a specified energy range based on the target thickness. For example, 13→7 MeV denotes an entrance energy of 13MeV and an exit energy of 7 MeV. For many publications, an exit energy was not specified.

^b For purpose of comparison, yields and impurities in this review were calculated from published saturated and/or physical yield data assuming an irradiation time of 1 hr

^c Although experiments were performed on $^{\text{nat}}\text{Mo}$, the published data was extrapolated to 100% enrichment

^d Includes contribution from cumulative $^{94}\text{Ru} \rightarrow ^{94m}\text{Tc}$ decay during a 1 hr irradiation

2.3.2. ^{94m}Tc Target preparation

While the use of a $^{\text{nat}}\text{Mo}$ foil is the simplest target design employed for ^{94m}Tc production [4, 14, 25, 26], thick foils of enriched molybdenum are not readily available. Several alternative strategies for target preparation using different forms of molybdenum have been investigated to overcome this limitation.

One of the most common methods for thick target preparation is the pressing of an enriched MoO_3 pellet into a recessed aluminum or platinum target holder covered by a thin aluminum or tantalum foil [4, 23, 24, 27]. Since these metal-oxide pellets are fragile and may be damaged when transferred from the pressing-tool to the target head, Blessing et al. [28] have introduced a device which applies a steady counter pressure when the pellet is removed. Irradiations on the metal-oxide targets are typically carried out with beam currents on the order of 5 μA . Qaim [29] notes, however, that although the $^{94}\text{Mo}(p,n)^{94m}\text{Tc}$ reaction can yield GBq quantities of ^{94m}Tc with these low beam currents, target modifications may be required to allow for sufficient heat removal when irradiating at higher beam currents.

A second common strategy for target preparation is that of sedimentation. This method first employs the suspension of very fine Mo metal or MoO_3 powder [3, 13, 30] in water-free acetone and colophonium [13], water-free acetone and nitrocellulose [3, 30], or water and methylcellulose [30]. The suspension is transferred into a vertical cylindrical polytetrafluoroethylene (PTFE) column, and allowed to evaporate onto a nickel [13] or copper [3, 30] foil. The importance of cleaning the copper backing foil to prevent blistering, cracking, gas pits, and peeling off of the MoO_3 layer has been noted [30]. Sadeghi et al. [30] present a thorough study evaluating solvent volumes and report optimal nitrocellulose and methylcellulose concentrations of 2.00 % and 13.36%, respectively. Their study resulted in successful proton irradiation of a $^{\text{nat}}\text{MoO}_3$ target up to 30 μA .

While not as common, several groups have investigated the chemical preparation of molybdate targets. As examples, Christian et al. [4] formed a crusty surface of hydrated ammonium molybdate by dissolving MoO_3 in concentrated NH_4OH , Graf et al. [12] produced CuMoO_4 by heating a mixture of MoO_3 and CuO powders, and Rösch et al. [27] investigated several molybdate target systems by mixing alkali or alkaline earth compounds with MoO_3 both pre- and post-irradiation. Challenges noted with these targets include thickness inhomogeneities [4], and poor thermochromatographic technetium recovery [27].

As a final method, and perhaps future direction for molybdenum target preparation, we note a conceptual target design proposed by Illan and Wieland [31]. The proposed strategy is based on the irradiation of thin molybdenum fibres whereby the recoil technetium nuclei escape from the molybdenum fibres into a liquid or gas. In this design, the technetium can be transported out of the target while leaving behind the molybdenum fibres. This target would immediately be ready for re-irradiation without the need for further processing/modification. Although this design is attractive in that it eliminates the need for repeated target preparation and technetium extraction, the major challenge of this concept-based design is the acquisition and construction an enriched molybdenum fibre target matrix.

Regardless of the target preparation strategy employed, it is important to consider the safe removal and handling of the irradiated solid target and potential dose to personnel. Thus, when considering production of $^{94\text{m}}\text{Tc}$, a solid target delivery system may prove beneficial [32].

2.2.3. $^{94\text{m}}\text{Tc}$ Target processing

We discuss in detail the two primary strategies which have been employed for recovery of $^{94\text{m}}\text{Tc}$. These include the thermochromatographic separation of the $^{94\text{m}}\text{Tc}$ from a solid molybdenum matrix, as well as solvent-extraction of $^{94\text{m}}\text{Tc}$. The goal in both of these strategies is to yield a final product of $[\text{}^{94\text{m}}\text{Tc}]\text{TcO}_4^-$

which may be used in place of $[\text{}^{99\text{m}}\text{Tc}]\text{TcO}_4^-$ for radiopharmaceutical labelling using commercially available kits.

2.3.3.1. Thermochromatographic separation

A conventional thermochromatographic setup entails the heating of an irradiated target under gas flow in a quartz tube. This strategy relies on volatilization of the technetium followed by adsorption onto the quartz walls. Separation of technetium and molybdenum can be achieved if their respective chemical species adsorb at temperatures which are significantly different in comparison to the quartz temperature gradient. In optimizing the thermochromatographic separation scheme, Rösch et al. [27] noted that use of a moist air sweep gas as opposed to dry air resulted in a greater difference in adsorption temperatures between the Mo/Tc species. The improved separation was attributed to the increased differences in adsorption temperatures for the $\text{MoO}_3/\text{H}^{94\text{m}}\text{TcO}_4$ system when compared to the $\text{MoO}_3/^{94\text{m}}\text{TcO}_x$ system. In the latter system, Rösch et al. presumed that $x = 3$ [27]. When using metallic molybdenum targets, similar thermochromatographic behaviour to the MoO_3/air -systems was noted when 60–80% oxygen-enhanced air was employed [27].

In an attempt to further enhance the separation efficiency by decreasing the volatility of the Mo-species, several metallic molybdate species were investigated [27]. While experimental yields of 99% technetium were obtained, this could only be achieved when the molybdate forming compound was added to MoO_3 post-irradiation. In contrast, almost no release of technetium was observed when the metallic molybdate was irradiated directly. Recycling the enriched target material using this strategy would therefore require quantitative conversion of the metallic molybdate species back to molybdenum(VI) oxide. As this conversion adds an additional level of complexity and potential for loss of the enriched target material, the $\text{MoO}_3/\text{H}^{94\text{m}}\text{TcO}_4$ separation procedure was deemed preferable.

Thermochromatographic separation was employed by Rösch et al. [27] to separate $^{94\text{m}}\text{Tc}$ from a 300 mg pressed, proton-irradiated, $[\text{}^{94}\text{Mo}]\text{MoO}_3$ target. This

procedure entailed a 15 minute distillation at a maximum temperature of 1090 °C in a vertical quartz apparatus and washing of the ^{94m}Tc from the quartz wall using 5 mL hot 10^{-4} M NaOH. A final purification with a minimized alumina column is reported [27]. The entire separation procedure was completed in approximately 25 minutes. Decay-corrected separation efficiencies of 80–85%, or 40–45% non-decay corrected, and a radiochemical pertechnetate purity of > 99% are reported. The reported losses of the enriched MoO_3 target material were less than 5% per separation cycle.

While the thermochromatographic separation procedures discussed in the literature are generally similar [4, 23, 33] to the methods presented by Rösch et al. [27], subtle differences can be identified. For example, to separate molybdenum, technetium, and ruthenium, Denzler et al. [13] employ a chlorine sweep gas of 80–340 mL/min. In contrast, Christian et al. [4] do not employ a sweep gas other than the natural convection of air through the open tube. Recovery of the technetium activity from the quartz tube has been reported using rinses of 30% H_2O_2 and 5 M NaOH [4] as well as hot methanol [24]. While Bigott et al. [24] observed 60% $^{94}\text{Mo}] \text{MoO}_3$ recovery yields for a single distillation, improved recovery was noted when the $^{94}\text{Mo}] \text{MoO}_3$ was allowed to build-up on the quartz tube for several consecutive separations. Finally, we note an alternative setup proposed by Nickles et al. [34]. In this version, they have resourcefully attempted to apply the thermochromatographic separation strategy to achieve on-line *in situ* separation of technetium using a molten target and vertical beam-line. The primary difficulty of this approach however is the challenge of maintaining exquisite temperature control of the target during irradiation.

2.3.3.2. Solvent extraction

The first step in wet chemical separation is the dissolution of the irradiated target. Electrolytic dissolution of irradiated $^{\text{nat}}\text{Mo}$ metal foil in HCl and H_2O_2 has been reported [4, 14, 25, 26]. Nickles et al. [25] give a detailed schematic of the ultrasonically agitated glassy carbon electrochemical cell employed for the foil dissolutions. Following dissolution, the solution is made basic with NaOH [14,

25], upon which methyl ethyl ketone (MEK) is then added. The technetium-containing organic layer may be further washed with fresh NaOH to reduce the MoO_4^- and peroxide concentrations to ppm levels [4]. The MEK fraction is blown to dryness in, for example, a helium stream and the pertechnetate is taken up in physiological saline and passed through a 0.22 μm Millipore filter [4, 25]. A critical detail noted by Christian et al. [4] is that normal glassware should be avoided as boron contamination of the basic medium may cause problems with some of the pharmaceutical kit preparations.

Reuse of an enriched molybdenum target was reported by Christian et al. [4] by employing solvent extraction on a target of hydrated ammonium molybdate. For this setup, the target is irradiated at $< 1 \mu\text{A}$ for several minutes to cause dehydration and drive off NH_3 . Following the period of outgassing, the irradiation current is then increased to $8 \mu\text{A}$. Post irradiation the MoO_3 target is dissolved with 30% H_2O_2 and made basic with NH_4OH . The technetium is extracted into MEK as above which entailed washing with base, blowing to dryness, and reconstituting in saline. The ammonium molybdate of the aqueous fraction is later blown to dryness in a glassy carbon target and can be re-used for a subsequent irradiation. Technetium radioisotope yields of 80% and ^{94}Mo mass recoveries of 95% are reported with this processing strategy. While these values were an improvement over the thermochromatographic-based separation noted in the same study, which reported activity yields and mass recoveries of 70% and 84%, respectively, the authors note that the chemical preparation of the ammonium molybdate resulted in an inhomogeneous target which thus complicated thickness estimates.

2.3.3.3. *Comparison of thermochromatography and solvent extraction*

The limited investigations and wide variability noted throughout the literature including the thermochromatographic ^{94}Mo mass recovery yields ranging from 60% [24] to greater than 95% [27] make it difficult to draw a conclusion as to which of these two strategies is optimal. In comparing these two strategies however, parameters to keep in mind include the separation efficiency,

processing time which consequently affects the yield and purity, dose to personnel, complexity of the setup which is a parameter that may depend on local expertise, and recovery of the expensive enriched molybdenum target material.

These are not, however, the only two strategies which may be employed for separation of technetium from an irradiated molybdenum target. As an example, Denzler et al. [13] transfer a [^{92}Mo]MoO₃ target dissolved in ammonia onto an alumina column and [$^{94\text{m}}\text{Tc}$]TcO₄⁻ is selectively eluted using acetone based on the different chromatographic behaviours of molybdenum, ruthenium, and technetium. Furthermore, while the total number of studies on $^{94\text{m}}\text{Tc}$ separation is perhaps limited, there are numerous studies that investigate the separation of $^{99\text{m}}\text{Tc}$ from molybdenum targets including the $^{98}\text{Mo}(n,\gamma)^{99}\text{Mo} \rightarrow ^{99\text{m}}\text{Tc}$ or $^{100}\text{Mo}(p,2n)^{99\text{m}}\text{Tc}$ reactions [35, 36, 37]. A thorough investigation of alternative $^{99\text{m}}\text{Tc}$ separation strategies may provide additional insight into strategies for further optimization of $^{94\text{m}}\text{Tc}$ recovery.

2.4. References

1. K. Gagnon, S. McQuarrie, D. Abrams, A.J.B. McEwan, F. Wuest, Radiotracers based on technetium-94m, *Current Radiopharmaceuticals* 4 (2011), 90–101.
2. E.A. Skakun, V.S. Batiĭ, Y.N. Rakivnenko, O.A. Rastrepin, Excitation functions and isomeric ratios for the interaction of protons of less than 9 MeV with Zr and Mo isotopes, *Sov. J. Nucl. Phys.* 46 (1987) 17–24.
3. F. Rösch, S.M. Qaim, Nuclear data relevant to the production of the positron emitting technetium isotopes $^{94\text{m}}\text{Tc}$ via the $^{94}\text{Mo}(p,n)$ -reaction, *Radiochim. Acta.* 62 (1993) 115–121.
4. B.T. Christian, R.J. Nickles, C.K. Stone, T.L. Mulnix, J. Clark, Improving the radionuclidic purity of $^{94\text{m}}\text{Tc}$ for PET imaging, *Appl. Radiat. Isot.* 46 (1995) 69–73.

5. M.U. Khandaker, M.S. Uddin, K.S. Kim, Y.S. Lee, G.N. Kim, Measurement of cross-sections for the (p,xn) reactions in natural molybdenum, *Nucl. Instrum. Meth. B.* 262 (2007) 171–181.
6. M.S. Uddin, M. Baba, Proton-induced activation cross-sections of the short-lived radionuclides formation on molybdenum, *Appl. Radiat. Isot.* 66 (2008) 208–214.
7. O. Lebeda, M. Pruszyński, New measurement of excitation functions for (p,x) reactions on ^{nat}Mo with special regard to the formation of ^{95m}Tc , $^{96m+g}\text{Tc}$, ^{99m}Tc and ^{99}Mo , *Appl. Radiat. Isot.* 68 (2010) 2355–2365.
8. J.M. Matuszek Jr., T.T. Sugihara, The decay of 293 min Tc^{94} , *Nucl. Phys.* 42 (1963) 582–591.
9. Z. Řanda, K. Svoboda, Excitation functions and yields of (d,n) and (d,2n) reactions on natural molybdenum, *J. Inorg. Nucl. Chem.* 38 (1976) 2289–2295.
10. M. Sonck, S. Takács, F. Szelecsényi, A. Hermanne, F. Tárkányi, In: Production technologies for molybdenum-99 and technetium-99m (TECDOC-1065); International Atomic Energy Agency, Vienna (1999) pp. 113–131.
11. O. Lebeda, M. Fikrle, New measurement of excitation functions for (d,x) reactions on ^{nat}Mo with special regard to the formation of ^{95m}Tc , $^{96m+g}\text{Tc}$, ^{99m}Tc and ^{99}Mo , *Appl. Radiat. Isot.* 68 (2010) 2425–2432.
12. H.P. Graf, H. Münzel, Excitation functions for α -particle reactions with molybdenum isotopes, *J. Inorg. Nucl. Chem.* 36 (1974) 3647–3657.

13. F.-O. Denzler, F. Rösch, S.M. Qaim, Excitation functions of α -particle induced nuclear reactions on highly enriched ^{92}Mo : Comparative evaluation of production routes for $^{94\text{m}}\text{Tc}$, *Radiochim. Acta.* 68 (1995) 13–20.
14. R.J. Nickles, A.D. Nunn, C.K. Stone, S.B. Perlman, R.L. Levine, Tc-94m flow agents: Bridging PET and SPECT, *J. Nucl. Med.* 32 (1991) 925.
15. M.F. Smith, M.E. Daube-Witherspoon, P.S. Plascjak, L.P. Szajek, R.E. Carson, J.R. Everett, S.L. Green, P.R. Territo, R.S. Balaban, S.L. Bacharach, W.C. Eckelman, Device-dependent activity estimation and decay correction of radionuclide mixtures with application to Tc-94m PET studies, *Med. Phys.* 28 (2001) 36–45.
16. H.H. Bissem, R. Georgi, W. Scobel, J. Ernst, M. Kaba, J.R. Rao, H. Strohe, Entrance and exit channel phenomena in d- and ^3He -induced preequilibrium decay, *Phys. Rev. C.* 22 (1980) 1468–1484.
17. L.T. Auler, A.G. Da Silva, G.W.A. Newton, Excitation functions and isomer ratios in $^{93}\text{Nb}(^3\text{He},\text{xn})$ reactions with $X = 2$ and 3 , *J. Inorg. Nucl. Chem.* 43 (1981) 2611–2615.
18. M. Faßbender, A.F. Novgorodov, F. Rösch, S.M. Qaim, Excitation functions of $^{93}\text{Nb}(^3\text{He},\text{xn})^{93\text{m,g}, 94\text{m,g}, 95\text{m,g}}\text{Tc}$ -processes from threshold up to 35 MeV: Possibility of production of $^{94\text{m}}\text{Tc}$ in high radiochemical purity using a thermochromatographic separation technique, *Radiochim. Acta.* 65 (1994) 215–221.
19. T. Matsuo, J.M. Matuszek Jr., N.D. Dudey, T.T. Sugihara, Cross-section ratios of isomeric nuclides produced in medium-energy (α,xn) reactions, *Phys. Rev.* 139 (1965) B886–B895.

20. P. Bond, S. Jha, Nuclear-structure and hyperfine-field studies with Mo⁹⁵, Phys. Rev. C. 2 (1970) 1887–1897.
21. C.L. Branquinho, S.M.A. Hoffmann, G.W.A. Newton, V.J. Robinson, H.-Y. Wang, I.S. Grant, J.A.B. Goodall, Excitation functions and isomer ratios in the reactions ⁹³Nb(α,xn) (x = 1-4), J. Inorg. Nucl. Chem. 41 (1979) 617–623.
22. E. Gadioloi, E. Gadioloi-Erba, J.J. Hogan, B.V. Jacak, Model for alpha particle induced nuclear reactions: ⁹³Nb(α,xαypzn) from 40-140 MeV, Phys. Rev. C. 29 (1984) 76–92.
23. B.E. Rogers, J.J. Parry, R. Andrews, P. Cordopatis, B.A. Nock, T. Maina, MicroPET imaging of gene transfer with Somatostatin receptor-based reporter gene and ^{94m}Tc-Demotate 1, J. Nucl. Med. 46 (2005) 1889–1897.
24. H.M. Bigott, R. Laforest, X. Liu, A. Ruangma, F. Wuest, M.J. Welch, Advances in the production, processing and microPET image quality of technetium-94m, Nucl. Med. Biol. 33 (2006) 923–933.
25. R.J. Nickles, A.D. Nunn, C.K. Stone, B.T. Christian, Technetium-94m-Teboroxime: Synthesis, dosimetry and initial PET imaging studies, J. Nucl. Med. 34 (1993) 1058–1066.
26. C.K. Stone, B.T. Christian, R.J. Nickles, S.B. Perlman, Technetium 94m-labeled methoxyisobutyl isonitrile: Dosimetry and resting cardiac imaging with positron emission tomography, J. Nucl. Cardiol. 1 (1994) 425–433.
27. F. Rösch, A.F. Novgorodov, S.M. Qaim, Thermochromatographic separation of ^{94m}Tc from enriched molybdenum targets and its large scale

- production for nuclear medical applications, *Radiochim. Acta.* 64 (1994) 113–120.
28. G. Blessing, F.-O. Denzler, S.M. Qaim, Improved target systems for irradiation of solids and gases at the compact cyclotron in Jülich, *Proceedings of the 7th International Workshop on Targetry and Target Chemistry*, Heidelberg, Germany, June 8-11 (1997) pp. 184–185.
29. S.M. Qaim, Production of high purity ^{94m}Tc for positron emission tomography studies, *Nucl. Med. Biol.* 27 (2000) 323–328.
30. M. Sadeghi, T. Kakavand, M. Aref, P. Sarabadani, Targetry of MoO_3 on a copper substrate for the no-carrier-added ^{94m}Tc production via $^{94}\text{Mo}(p,n)^{94m}\text{Tc}$ reaction, *Nucl. Sci. Tech.* 20 (2009) 22–26.
31. C.D. Illan, B.W. Wieland, Evaluation of a recoil-escape fiber target using $^{94}\text{Mo}(p,n)^{94m}\text{Tc}$ to produce $^{94}\text{TcO}_4^-$ precursor for radiolabeled compounds useful in positron emission tomography. *Proceedings of the 23rd Annual EMBS International Conference*, Istanbul, Turkey Oct 25–28 (2001) pp. 2347–2350.
32. G. Gaehle, P. Margenau, D. McCarthy, D. Rowland, B. Hughey, R. Klinkowstein, R. Shefer, A. Dart, R. Ledoux, M. Welch, The installation of a solid target system produced by Newton Scientific on a 168 JSW baby cyclotron capable of loading and delivering multiple solid targets with a single setup. *Proceedings of the 17th International Conference on Applications of Accelerators in Research and Industry* Denton, Texas, Nov 12–16, 2002; J.L. Duggan, L.L. Morgan, Eds.; American Institute of Physics, (2003) pp. 785–787.

33. L.G. Luyt, H.M. Bigott, M.J. Welch, J.A. Katzenellenbogen, 7 α - and 17 α -Substituted estrogens containing tridentate tricarbonyl rhenium/technetium complexes: Synthesis of estrogen receptor imaging agents and evaluation using microPET with technetium-94m, *Bioorg. Med. Chem.* 11 (2003) 4977–4989.
34. R.J. Nickles, B.T. Christian, C.C. Martin, A.D. Nunn, C.K. Stone, Tc-94m radionuclide purity requirements for pharmacokinetic studies with PET, *J. Nucl. Med.* 33 (1992) 850.
35. N. Dallali, M. Ghanbari, Y. Yamini, B. Fateh, Y.K. Agrawal, Liquid-liquid extraction of ultra-trace amounts of technetium produced by $^{100}\text{Mo}(p,2n)^{99\text{m}}\text{Tc}$ nuclear reaction in cyclotron, *Indian. J. Chem. A.* 46A (2007) 1615–1617.
36. S. Chattopadhyay, S.S. Das, L. Barua, A simple and rapid technique for recovery of $^{99\text{m}}\text{Tc}$ from low specific activity $(n,\gamma)^{99}\text{Mo}$ based on solid-liquid extraction and column chromatography methodologies, *Nucl. Med. Biol.* 37 (2010) 17–20.
37. R. Chakravarty, A. Dash, M. Venkatesh, A novel electrochemical technique for the production of clinical grade $^{99\text{m}}\text{Tc}$ using $(n,\gamma)^{99}\text{Mo}$, *Nucl. Med. Biol.* 37 (2010) 21–28.

3. $^{100}\text{Mo}(\text{p},\text{x})$ Cross sections

A version of this chapter was published in:

K. Gagnon, F. B nard, M. Kovacs, T.J. Ruth, P. Schaffer, J.S. Wilson and S.A. McQuarrie, Cyclotron production of $^{99\text{m}}\text{Tc}$: Experimental measurement of the $^{100}\text{Mo}(\text{p},\text{x})^{99}\text{Mo}$, $^{99\text{m}}\text{Tc}$, and $^{99\text{g}}\text{Tc}$ excitation functions from 8 to 18 MeV, Nucl. Med. Biol. 38 (2011) 907–916.

3.1. Introduction

Knowledge of nuclear cross sections and theoretical yields are essential for optimizing the high current irradiation conditions and verifying the processing and recovery strategies when producing large scale quantities of $^{99\text{m}}\text{Tc}$ for clinical use.

A review of existing published cross section data for the direct $^{100}\text{Mo}(\text{p},2\text{n})^{99\text{m}}\text{Tc}$ reaction reveals large discrepancies in the measured values. Thus, the first goal of this work was to re-evaluate the excitation function for this reaction. In measuring this excitation function, evaluation of the $^{100}\text{Mo}(\text{p},\text{x})^{99}\text{Mo}$ excitation function was also warranted so that any $^{99\text{m}}\text{Tc}$ produced indirectly from ^{99}Mo decay could be accounted for.

A schematic illustrating a select subset of competing reactions which occur during proton irradiation of ^{100}Mo is given in Figure 3-1. This figure illustrates how concomitant $^{99\text{g}}\text{Tc}$ production may result from the decay of ^{99}Mo , decay of $^{99\text{m}}\text{Tc}$, or via the (p,2n) transformation of ^{100}Mo . Given the numerous reaction pathways that yield $^{99\text{m}}\text{Tc}$ and $^{99\text{g}}\text{Tc}$, coupled with the suggestion by Scholten et al. that the coproduction of the long-lived $^{99\text{g}}\text{Tc}$ contaminant may be a limiting factor in the cyclotron production of $^{99\text{m}}\text{Tc}$ [1], the next major goal of this

work was to experimentally evaluate the ^{99g}Tc excitation function and compare the level of ^{99g}Tc present in the cyclotron-produced ^{99m}Tc with the ^{99g}Tc levels of the current $^{99}\text{Mo}/^{99m}\text{Tc}$ generator technology.

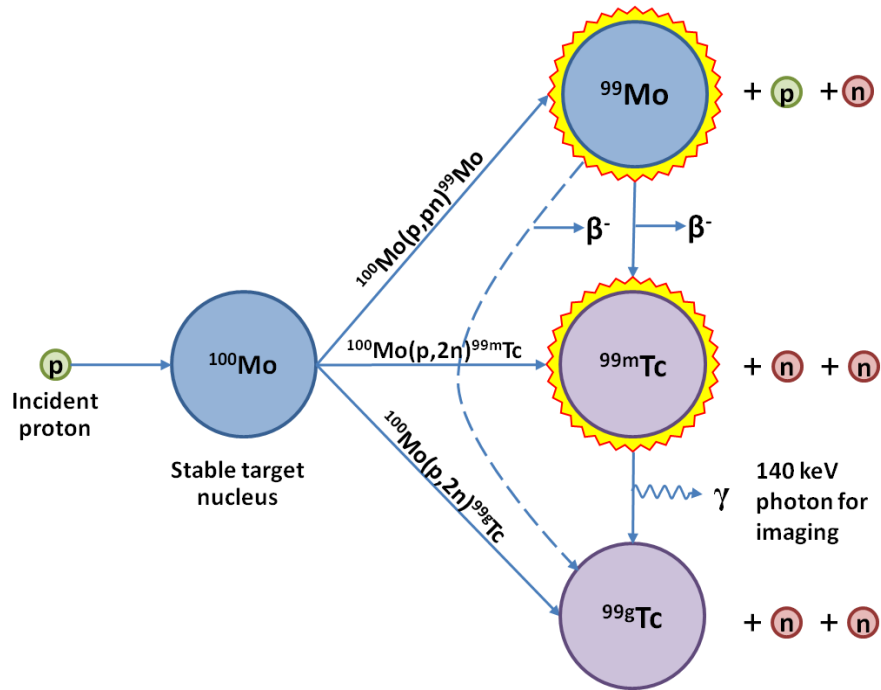


Figure 3-1. Select subset of reactions following the proton irradiation of ^{100}Mo which give rise both to the direct and indirect production of both ^{99m}Tc and ^{99g}Tc .

The production of ^{99m}Tc and ^{99}Mo may be quantified via γ -ray spectroscopy using a high purity germanium (HPGe) detector. In contrast, this method is not ideal for quantifying ^{99g}Tc due to its low overall radioactivity and the low, $6.5 \times 10^{-4} \%$, abundance of its single 89.5 keV γ -ray. This mandated an alternative strategy for evaluating the ^{99g}Tc content, and ultimately the excitation function. Several methods exist that would enable ^{99g}Tc determination including low background gas flow counting, (n,γ) and (n,n') neutron activation analysis, liquid scintillation counting, inductively coupled plasma mass spectrometry (ICP-MS), as well as others. We utilized ICP-MS for this study as this strategy presented the lowest detection limit [2] and was not influenced by the presence of

low-level contaminant technetium radioactivity such as that produced by the $^{95}\text{Mo}(p,n)^{95m}\text{Tc}$ reaction. The direct ^{99g}Tc excitation function was thus determined using ICP-MS in combination with γ -ray spectroscopy to correct for the indirect ^{99g}Tc contributions following decay of ^{99m}Tc and ^{99}Mo .

3.2. Materials and methods

3.2.1. Foil irradiations

To minimize the corrections required when accounting for the formation of ^{99m}Tc from ^{99}Mo decay, as well as investigate the effects of using $^{\text{nat}}\text{Mo}$ versus enriched ^{100}Mo , a series of short 10 minute irradiations were performed. In contrast, optimization of statistics for the ICP-MS measurements led to 10 hr irradiations on 97.42% enriched ^{100}Mo foils. The two irradiation protocols are discussed below. All irradiations were performed on the variable energy TR-19/9 Cyclotron (Advanced Cyclotron Systems Inc., Richmond, BC) at the Edmonton PET Centre.

3.2.1.1. Short ^{99m}Tc irradiation protocol

During the proton irradiation of $^{\text{nat}}\text{Mo}$ for which secondary neutrons are also considered, ^{99m}Tc may arise from the following reactions:

- (i) $^{100}\text{Mo}(p,2n)^{99m}\text{Tc}$
- (ii) $^{100}\text{Mo}(p,pn)^{99}\text{Mo} \rightarrow ^{99m}\text{Tc}$
- (iii) $^{100}\text{Mo}(n,2n)^{99}\text{Mo} \rightarrow ^{99m}\text{Tc}$
- (iv) $^{100}\text{Mo}(p,2p)^{99}\text{Nb} \rightarrow ^{99}\text{Mo} \rightarrow ^{99m}\text{Tc}$
- (v) $^{98}\text{Mo}(n,\gamma)^{99}\text{Mo} \rightarrow ^{99m}\text{Tc}$
- (vi) $^{98}\text{Mo}(p,\gamma)^{99m}\text{Tc}$.

This work seeks to determine the cross section for (i), the direct (p,2n) production of ^{99m}Tc . Although reactions (ii)–(v) also give rise to ^{99m}Tc , the direct ^{99m}Tc production cross section may be isolated by subtracting out any indirect ^{99m}Tc contributions produced from the decay of ^{99}Mo . Despite such corrections, we further minimized contributions (ii)–(v) by employing short irradiation times

of 600 seconds and evaluating the ^{99m}Tc production within a few hours post-irradiation. While contributions (v) and (vi) may be eliminated by employing enriched ^{100}Mo , it has been suggested that these contributions are negligible with regards to the direct production route [3, 4, 5], and that it should be possible to extrapolate the $^{100}\text{Mo}(p,2n)^{99m}\text{Tc}$ excitation function using natural abundance molybdenum. To verify this hypothesis, we employed both natural abundance (7.5 mg/cm²) and enriched ^{100}Mo foils (7.4–11.1 mg/cm², Trace Sciences International). Upon correcting for the isotopic composition of ^{100}Mo , contributions from (vi) can be identified by noting differences in the direct production cross sections for ^{99m}Tc when comparing irradiations on $^{\text{nat}}\text{Mo}$ and enriched ^{100}Mo foils. The isotopic compositions of the $^{\text{nat}}\text{Mo}$ and enriched ^{100}Mo foils are summarized in Table 3-1.

Table 3-1. Isotopic compositions of natural abundance and enriched molybdenum foils.

	Natural Abundance	^{100}Mo Enriched
^{100}Mo [%]	9.63	97.42
^{98}Mo [%]	24.13	0.96
^{97}Mo [%]	9.55	0.28
^{96}Mo [%]	16.68	0.34
^{95}Mo [%]	15.92	0.29
^{94}Mo [%]	9.25	0.18
^{92}Mo [%]	14.84	0.53
Molar mass [g/mol]	95.94	99.80

Foils were individually irradiated to allow for maximum flexibility for the HPGe detector assay times. Stable beam currents of approximately 1 μA were achieved by first tuning the beam on a secondary target prior to irradiation of the molybdenum foils. Since the minimum extraction energy of the TR-19/9 cyclotron is approximately 13.7 MeV, an aluminum degrader was necessary

whenever lower energies were desired. When used, the degrader was always placed directly adjacent and upstream of the molybdenum foil. The beam energy and irradiation current were also evaluated for all irradiations by using a copper monitor foil. The copper foil was located directly next to and upstream of the aluminum degrader or next to the Mo foil in the absence of a degrader.

3.2.1.2. Long ^{99g}Tc irradiation protocol

Since the ^{99g}Tc excitation function was evaluated using ICP-MS, significantly longer irradiation times were required so that the number of nuclei produced was at a level which was well above the detection limit of the Perkin Elmer Elan 6000 ICP-MS system which we measured to be 2.7 ppt. The 97.42% enriched ^{100}Mo foils were therefore irradiated for 10 hr at a beam current of ~ 20 μA . Under these conditions the ^{99g}Tc content was predicted [6] to be on the order of 1–5 ppb.

The enriched ^{100}Mo foils used for these ^{99g}Tc measurements were recovered from the ^{99m}Tc irradiations described in Section 3.2.1.1. The reuse of the foils posed no concern for interfering ^{99g}Tc contributions as the total integrated current employed for the ^{99m}Tc measurements was less than 0.1% of those employed for the ^{99g}Tc irradiations. Due to the long irradiation times, stacks of four or five ^{100}Mo foils were irradiated. An aluminum foil degrader was placed between each ^{100}Mo foil, and two copper monitor foils were also positioned within the stack.

Following the HPGe detector assaying of ^{99m}Tc and ^{99}Mo , foils were left to decay for two months to allow for complete decay of the ^{99m}Tc and ^{99}Mo reaction products prior to analysis by ICP-MS. Long irradiations were not performed on natural abundance molybdenum as the long-lived technetium by-products such as ^{95m}Tc would have exceeded exemption limits for transport to the ICP-MS facility.

3.2.2. Activity assay

3.2.2.1. Assays for the short (10 minute) irradiations

All samples were assayed for radionuclidic products via γ -ray spectroscopy using an HPGe detector (Ortec model GEM35P4-S). The detector was calibrated using NIST traceable calibration sources (Eckert and Ziegler) of ^{22}Na , ^{54}Mn , ^{57}Co , ^{60}Co , ^{109}Cd , ^{133}Ba and ^{137}Cs . A rigid stand was employed to ensure consistent placement of the samples at a distance of either 25 or 50 cm from the detector end cap. A separate detector calibration was performed for each of these two configurations. In other words, geometric interpolation was not employed. A sample detector efficiency calibration curve is provided in Figure 3-2.

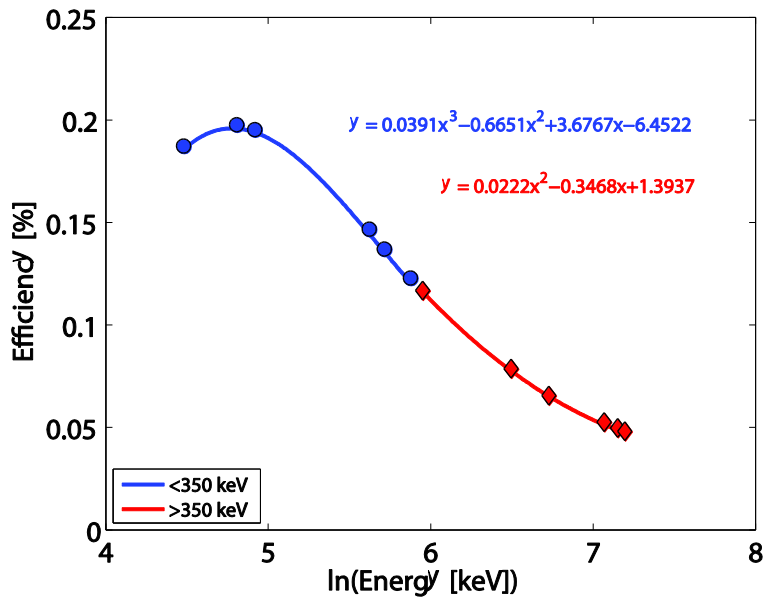


Figure 3-2. HPGe detector efficiency calibration curve measured for a 25 cm sampling distance. Efficiency data is plotted against the natural log of energy for ease of curve fitting. Two separate polynomial curves are given; the blue curve is used for $E_\gamma < 350$ keV while the red curve is used for $E_\gamma > 350$ keV.

In evaluating the direct ^{99m}Tc cross section, it was necessary to consider contributions from the presence of ^{99}Mo which undergoes beta decay to form ^{99m}Tc . These contributions may occur: (i) during irradiation, (ii) post irradiation, or (iii) during the sample activity assay. Efforts were made to limit this indirect production of ^{99m}Tc arising from decay of ^{99}Mo by minimizing the above three times. First, irradiation times were limited to ten minutes. Next, the ^{99m}Tc assays were performed 1–2 hr post-end-of-bombardment (EOB) for the ^{100}Mo foils, and 5–7 hr post-EOB for $^{\text{nat}}\text{Mo}$. Finally, typical assay live times were 5–15 min, although a few samples were assayed for a maximum of 1 hr. Dead times for all assays were less than 6.5%, and counting errors were less than 2%. Counting errors were calculated by adding the statistical error, whereby Poisson statistics was assumed, in quadrature to the peak fitting uncertainty given by the Ortec Gamma Vision v. 6.01 software.

The ^{99}Mo assays were performed 0–1 day post-EOB for the ^{100}Mo foils and 1–5 days post-EOB for $^{\text{nat}}\text{Mo}$. The length of the assays varied from 1–33 hr and dead times were always less than 5%. Activities were calculated using a weighted average of the 181 and 739 keV peaks. A maximum weighted counting error of 2.5% was observed for ^{100}Mo . The low activation cross sections and low ^{100}Mo abundance of 9.63% in $^{\text{nat}}\text{Mo}$ resulted in counting errors for the $^{\text{nat}}\text{Mo}$ foils as high as 60% for the lowest energy evaluated.

3.2.2.2. Assays for the long (10 hour) irradiations

Due to the long irradiation times required for the ^{99g}Tc cross sections measurements, these foils were too radioactive to be assayed within a few hours post-EOB at our standard 25/50 cm HPGe detector counting geometries. Despite waiting 24 hr post-EOB and placing the foils at the maximum possible counting distance of approximately 2 m for our setup, dead times were upwards of 30%. As these dead times were undesirably high, this problem was ameliorated by maintaining the ~2 m counting distance and placing a 10 mm brass attenuator between the detector and the foils. With this setup and performing the ^{99m}Tc activity assays between 25–29 hr post-EOB, the sample dead times were reduced

to the range of 1–11%. The counting error for all ^{99m}Tc assays was less than 2% and the activity assay live time was maintained at five minutes.

The aluminum degraders used in these irradiations were also assayed for the presence of ^{99m}Tc from recoiled reaction products. With count rates on these aluminum foils demonstrating a maximum of 0.6% when compared with the upstream adjacent ^{100}Mo foil, this small contribution was considered negligible and well within the scope of our experimental error.

The ^{99}Mo activity assays were performed 7–8 days post-EOB with no attenuator present. Dead times for these assays were less than 4%, and the assay lengths varied from 30 min to 45 hr. Similar to Section 3.2.2.1, activities were calculated using a weighted average of the 181 and 739 keV peaks. The weighted counting error was less than 2.5% for all but the 10 MeV foil, where a 10% counting error was noted.

In the absence of an attenuator, the HPGe detector efficiency was calibrated using the seven standard sources noted in Section 3.2.2.1. This efficiency calibration was used for quantifying the ^{99}Mo activity. Use of the seven standard sources for efficiency calibration of the detector at 140 keV in the presence of the brass attenuator plate proved problematic for two reasons. First, the activities of these standard sources are on the order of a few hundred kBq at most. Although this activity is ideal for our 25/50 cm calibrations, the ~2 m sampling distance and use of an attenuator resulted in undesirably low count rates particularly at energies less than 300 keV. Taking as an example, ^{57}Co , the counting error observed for the 136 keV peak in the presence of a brass attenuator was 4.5% after nearly 5 days of counting. Second, due to the presence of an attenuator, the change in efficiency at energies less than 300 keV was quite large. As such, interpolation between a limited number of data points in this high gradient region posed a concern for the introduction of further error.

The following approach was therefore employed for calibration of the detector at 140 keV in the presence of the brass attenuator. First, we measured the detector efficiency in the presence of the attenuator in the energy range of 350–

1335 keV using the ^{54}Mn , ^{60}Co , ^{133}Ba and ^{137}Cs standard sources. We then used the ^{99}Mo activation of one of the foils of this experiment to cross-calibrate the 140 keV and 739 keV efficiencies. The foil was assayed for 30 minutes live time with the dead time and counting errors maintained below 1%. The efficiency was taken as the average of four replicate counts. This cross-calibration was performed 11 days post-EOB to ensure complete decay of the directly produced $^{99\text{m}}\text{Tc}$ and transient equilibrium of the $^{99\text{m}}\text{Tc}$ born from ^{99}Mo . In cross-calibrating the two peaks, the intensity of the 739 keV peak was taken as 12.13% (see Table 3-2, [7]). With ^{99}Mo and $^{99\text{m}}\text{Tc}$ in transient equilibrium [8], the intensity of the 140 keV peak, I_{Eq}^{140} , was given as a combination of the $^{99\text{m}}\text{Tc}$ and ^{99}Mo 140 keV peak intensities of Table 3-2:

$$I_{Eq}^{140} = f \left(\frac{\lambda_{mTc}}{\lambda_{mTc} - \lambda_{Mo}} \right) (I_{mTc}^{140}) + (I_{Mo}^{140}) = 90.38\% , \quad (3.1)$$

where f is the branching ratio of 87.6% [9] for $^{99}\text{Mo} \rightarrow ^{99\text{m}}\text{Tc}$ decay, and λ_{mTc} and λ_{Mo} are the decay constants for $^{99\text{m}}\text{Tc}$ and ^{99}Mo respectively.

3.2.2.3. Activity calculations

All activities were corrected for decay during counting time, decay to EOB, detector efficiency, and γ -ray intensity [10]. The decay data utilized to calculate the activity of the produced radionuclides for this study are reported in Table 3-2.

Although the activity quantification was generally straightforward, in calculating the $^{99\text{m}}\text{Tc}$ activity, corrections were required to subtract out: (i) interference of the 140 keV peaks arising directly from decay of ^{99}Mo , $I_{Mo}^{140} = 4.52\%$, and (ii) indirect production of $^{99\text{m}}\text{Tc}$ as a result of ^{99}Mo decay, both during and post-irradiation. The following presents the corrections applied in this work. We felt such extended detail was warranted as we suspect the source of discrepancy amongst the literature may arise from not correctly executing this step.

Table 3-2. Summary of nuclear decay data obtained from the NNDC NuDat database [7].

Radionuclide	$t_{1/2}$	E_γ [keV]	I_γ [%]
^{99m}Tc	6.01 h	140.511	89.08 ^a
^{99}Mo	65.94 h	140.511	4.52
		181.068	5.99
		739.500	12.13
^{95m}Tc	61 d	204.117	63.2
^{62}Zn	9.26 h	548.35	15.3
		596.56	26.0
^{63}Zn	38.47 m	669.62	8.2
		962.06	6.5
^{65}Zn	243.66 d	1115.539	50.60

^a Includes 0.02% contribution from the 142.63 keV γ -ray

In addressing the first of these two corrections, we note that our total measured 140 keV net peak area, C_{Total}^{140} , is a combination of counts from both ^{99}Mo and ^{99m}Tc ,

$$C_{Total}^{140} = C_{Mo}^{140} + C_{mTc}^{140}, \quad (3.2)$$

where C_{mTc}^{140} is taken to include both the direct ^{99m}Tc and indirect $^{99}\text{Mo} \rightarrow ^{99m}\text{Tc}$ contributions. To determine C_{mTc}^{140} , we calculate the number of expected 140 keV counts arising directly from ^{99}Mo decay, C_{Mo}^{140} , and subtract this value from C_{Total}^{140} . The C_{Mo}^{140} term was calculated using the EOB activity of ^{99}Mo , A_{Mo}^{EOB} , which was determined using the independent 181 and 739 keV peaks:

$$C_{Mo}^{140} = \frac{A_{Mo}^{EOB} e^{-\lambda_{Mo} t_A} (1 - e^{-\lambda_{Mo} t_R}) \epsilon_{140} I_{Mo}^{140} t_L}{\lambda_{Mo} t_R}. \quad (3.3)$$

In equation (3.3), λ_{Mo} is the ^{99}Mo decay constant, t_A is the elapsed time between EOB and the start of counts (SOC), t_L is the detector live time, t_R is the

detector real time, ε_{140} is the detector efficiency at 140 keV, and I_{Mo}^{140} is the 140 keV γ -ray intensity of ^{99}Mo . The total ^{99m}Tc activity at SOC, $[A_{mTc}^{SOC}]_{Total}$, is then given by:

$$[A_{mTc}^{SOC}]_{Total} = \frac{(C_{Total}^{140} - C_{Mo}^{140})\lambda_{mTc}t_R}{(1 - e^{-\lambda_{mTc}t_R})\varepsilon_{140}I_{mTc}^{140}t_L}, \quad (3.4)$$

where I_{mTc}^{140} is the 140 keV γ -ray intensity of ^{99m}Tc . As indicated above, $[A_{mTc}^{SOC}]_{Total}$ includes contributions from both the direct production of ^{99m}Tc , and indirect production of ^{99m}Tc arising from $^{99}Mo \rightarrow ^{99m}Tc$,

$$[A_{mTc}^{SOC}]_{Total} = [A_{mTc}^{SOC}]_{Indirect} + [A_{mTc}^{SOC}]_{Direct}. \quad (3.5)$$

Since one of the goals of this work is to evaluate the cross section for the direct production of ^{99m}Tc , we must subtract out the activity contribution from the indirect formation of ^{99m}Tc . This is the second of the two corrections performed for determining the ^{99m}Tc activity. Lebeda and Pruszyński [5] give the activity of the indirect production of ^{99m}Tc born from ^{99}Mo as,

$$[A_{mTc}^{SOC}]_{Indirect} = \left(\frac{\lambda_{mTc}}{\lambda_{mTc} - \lambda_{Mo}} \right) f A_{Mo}^{EOB} (e^{-\lambda_{Mo}t_\Delta} - e^{-\lambda_{mTc}t_\Delta}) + [A_{mTc}^{EOB}]_{Indirect} e^{-\lambda_{mTc}t_\Delta}. \quad (3.6)$$

In this equation, the first term corresponds to $^{99}Mo \rightarrow ^{99m}Tc$ production post-EOB, while the second term corresponds to $^{99}Mo \rightarrow ^{99m}Tc$ production during bombardment. For an irradiation time, t_b , $[A_{mTc}^{EOB}]_{Indirect}$ is given as [5],

$$[A_{mTc}^{EOB}]_{Indirect} = f \frac{A_{Mo}^{EOB}}{(1 - e^{-\lambda_{Mo}t_b})} \left(1 - \frac{\lambda_{mTc}}{\lambda_{mTc} - \lambda_{Mo}} e^{-\lambda_{Mo}t_b} + \frac{\lambda_{Mo}}{\lambda_{mTc} - \lambda_{Mo}} e^{-\lambda_{mTc}t_b} \right). \quad (3.7)$$

Using equations (3.3)–(3.7), the direct ^{99m}Tc activity at EOB, $[A_{mTc}^{EOB}]_{Direct}$ is given as:

$$\left[A_{mTc}^{EOB} \right]_{Direct} = \left(\left[A_{mTc}^{SOC} \right]_{Total} - \left[A_{mTc}^{SOC} \right]_{Indirect} \right) e^{\lambda_{mTc} t_{\Delta}} \quad (3.8)$$

The direct ^{99m}Tc production cross sections for this work were thus calculated using $\left[A_{mTc}^{EOB} \right]_{Direct}$ of equation (3.8). The ^{99m}Tc corrections described above were employed for both the short and long irradiations in this study. Calculations were verified by repeating the ^{99m}Tc assays of the short-irradiation protocol one day post-EOB. An average absolute difference of 2% and a maximum difference of 6% were observed in the $\left[A_{mTc}^{EOB} \right]_{Direct}$ calculated within a few hours post-EOB, versus one day post-EOB for these foils.

Of the two terms in equation (3.6), the first is by far the most important. This is evident when examining the foils irradiated for 10 hr and measured one day post-EOB. Absence of the $^{99}\text{Mo} \rightarrow ^{99m}\text{Tc}$ correction post irradiation (i.e. the first term) resulted in a maximum 185% increase in the evaluated ^{99m}Tc activity, while absence in correcting for the ^{99m}Tc born from ^{99}Mo during irradiation (i.e. the second term) led to a maximum 2% increase.

3.2.3. Monitor reactions

The IAEA recommended $^{nat}\text{Cu}(p,x)^{62,63,65}\text{Zn}$ cross section data [11] were used to monitor the proton energy and irradiation current. The expected activity ratio for a given energy was calculated using

$$\frac{A_i}{A_j} = \frac{\sigma_i (1 - e^{-\lambda_i t_b})}{\sigma_j (1 - e^{-\lambda_j t_b})}, \quad (3.9)$$

where A , σ , λ and t_b represent the EOB activity, cross section, decay constant, and bombardment time for isotopes i and j . The energy of the short irradiations was evaluated by comparing the measured ratio of $^{62}\text{Zn}/^{63}\text{Zn}$ to the predicted ratios of equation (3.9). In contrast, the energy of the long irradiation protocol was evaluated using the $^{62}\text{Zn}/^{65}\text{Zn}$ measured activity ratio. The short-lived ^{63}Zn could not be employed for the long irradiation protocol as the foils were not removed from the target station until 1 day post-EOB. All evaluated energies were taken to

correspond to the centre of the 25.6 μm copper monitor foil. The energy at the centre of the molybdenum foil was determined by simulation of 1000 ions in the TRIM module of SRIM [12]. As the measured activity ratio is independent of both foil thickness and beam current, the error in the measured energy was obtained by adding the counting errors of ^{62}Zn and ^{63}Zn for the short irradiations or ^{62}Zn and ^{65}Zn for the long irradiations in quadrature.

Following energy determination, the proton irradiation current was evaluated by comparing the ^{63}Zn activity for the short irradiations, or the ^{62}Zn and ^{65}Zn activities for the long irradiations, with activities predicted using the IAEA recommended cross section data [11].

3.2.4. ICP-MS

3.2.4.1. ICP-MS setup/facility

ICP-MS was performed using a Perkin Elmer Elan 6000 at the University of Alberta's Radiogenic Isotope Facility. Measurements employed 35 sweeps per reading, a 20 ms dwell time, 3 reading replicates, and a two minute wash between all samples. Samples were analyzed for $m/z = 99, 100, 101, 102$ and 104 . The $^{99\text{g}}\text{Tc}$ concentrations were determined using a four-point calibration curve at 0, 1, 2, and 5 ppb, an ^{115}In internal standard correction, and a blank subtraction. The final concentrations were taken as an average of the 3 replicates. The standard deviation of the three replicates was less than 1% for all irradiated foils.

3.2.4.2. Technetium extraction

Chemical separation of the technetium from the bulk of the ^{100}Mo was necessary prior to measurement of the $^{99\text{g}}\text{Tc}$ contribution. This step was deemed essential as the ICP-MS $m/z = 99$ count rate of a non-irradiated ^{100}Mo foil which was dissolved in 0.5 mL 30% H_2O_2 /1.5 mL 8 N HNO_3 at 70 °C was determined to be ~20 ppb. This blank count rate was much higher than the expected count rate of ~1–5 ppb for the irradiated foils. The $m/z = 101$ count rate for the non-irradiated foil was on the same order of magnitude as $m/z = 99$. In contrast, the

$m/z = 102$ and 104 count rates were several orders of magnitude lower. Given the isotopic composition of ruthenium, the high count rates noted at $m/z = 99$ and 101 were attributed to a broadening of the $m/z = 100$ peak, and not to the presence of ruthenium in the sample.

Technetium was extracted from the bulk molybdenum of the irradiated foils by dissolution using 1 mL 30% H_2O_2 (Fisher, Reagent grade) and 3 mL 8 N HNO_3 (Fluka, Trace select grade diluted with 18 M Ω -cm Barnstead H_2O) at 70 °C. Solutions were then basified by the slow addition of ~3.0–3.5 mL 10 N KOH (Sigma-Aldrich, 85%, Reagent grade) until the solution was colorless. Liquid-liquid extraction was carried out by addition of 6 mL MEK (Anachemia, Reagent grade), shaking of the solution, and subsequent removal and nitrogen dry-down of the top 3 mL of the organic layer. This process was repeated by adding/removing an additional: 5mL/5mL, 5mL/5mL, and 3mL/3mL of MEK. The final dried sample was then reconstituted by addition of 1.3 mL of 18 M Ω -cm Barnstead H_2O . From each reconstituted sample, 980 μL was employed for ICP-MS. The ICP-MS sample was diluted to 1 mL by addition of 10 μL HNO_3 , and 10 μL of an ^{115}In internal standard. To identify possible solution matrix effects, ICP-MS was carried out on a 100 μL aliquot similarly diluted to 1 mL of the irradiated foil sample solution presenting the highest $^{99\text{g}}\text{Tc}$ concentration which was 7.6 ppb. Solution matrix effects were considered negligible as the difference between the X1 and X10 dilutions was less than 2%.

The above extraction procedure was found to reduce the $m/z = 99$ and 101 count rates to less than 1 ppt for non-irradiated ^{100}Mo . Efficient separation of the technetium was confirmed by monitoring the $m/z = 101$ count rate throughout the experiments on the irradiated foils. For all irradiated foils, the ratio of the $m/z = 101$ to $m/z = 99$ count rate was an average of 0.02%. A maximum ratio of 0.06% was observed. For the purpose of illustrating the low $m/z = 99$ count rate for non-irradiated foils, sample m/z count rates are presented in Figure 3-3 for both a non-irradiated 15.5 mg foil, and a 19.9 mg foil irradiated at 13.5 MeV, each of which were processed as described above.

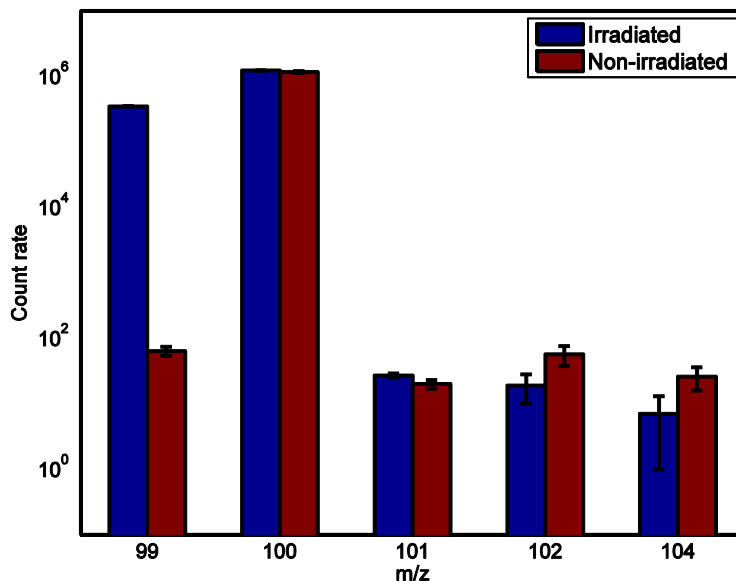


Figure 3-3. Sample m/z count rates for both a non-irradiated and an irradiated enriched ^{100}Mo foil. Each foil underwent chemical extraction to separate the bulk ^{100}Mo . Error bars are given as the standard deviation of the three replicate readings.

Prior to extraction, all foils were assayed for $^{95\text{m}}\text{Tc}$ so that the technetium extraction efficiency could be determined. Aliquots of the reconstituted solution were removed and prepared as thin samples for HPGe analysis by pipetting 25 μL of solution onto a $< 1 \text{ cm}^2$ piece of filter paper sealed within adhesive tape. Extraction efficiencies of 83–92% with standard deviations of 1–5% were noted in this work.

3.2.4.3. ICP-MS calibration

A calibration sample for ICP-MS was obtained by making use of the well-characterized $^{99\text{m}}\text{Tc}$ to $^{99\text{m}+99\text{g}}\text{Tc}$, $(N_{m\text{Tc}}/N_{m+g\text{Tc}})$ nuclei ratio for a $^{99}\text{Mo}/^{99\text{m}}\text{Tc}$ generator. This relationship is well characterized for the generator assuming: (i) knowledge of the elapsed time between elutions, t_{el} , and (ii) 100% removal of $^{99\text{m}}\text{Tc}$ and $^{99\text{g}}\text{Tc}$ in the previous elution [9],

$$\frac{N_{mTc}}{N_{m+gTc}} = \frac{f\lambda_{Mo} \left(e^{-\lambda_{Mo}t_{el}} - e^{-\lambda_{mTc}t_{el}} \right)}{\left(\lambda_{mTc} - \lambda_{Mo} \right) \left(1 - e^{-\lambda_{Mo}t_{el}} \right)} \quad (3.10)$$

To reduce the on-column technetium to negligible levels, a generator was eluted with 100 mL 0.9% NaCl. The generator was then left to decay for 45.5 hr and again re-eluted using 10 mL 0.9% NaCl. Approximately 100 GBq of ^{99m}Tc was eluted. The efficiency of the second elution was not of importance since we were only concerned with the ratio of ^{99m}Tc to $^{99m+99g}\text{Tc}$ nuclei. Assuming an error of 15 minutes as the 10 and 100 mL generator elution procedures occupy a finite length of time, the N_{mTc}/N_{m+gTc} ratio was determined from equation (3.10) to be $14.2 \pm 0.1\%$.

For consistency, the technetium obtained from the $^{99}\text{Mo}/^{99m}\text{Tc}$ generator was processed using a single MEK extraction (Section 3.2.4.2). This extracted calibration sample was dried under a stream of nitrogen and reconstituted using 1.6 mL of 18 M Ω -cm Barnstead water. Five 20 μL aliquots were prepared as thin samples and assayed to quantify the ^{99m}Tc activity. After decay correction to the extraction time, the total number of ^{99m}Tc nuclei in the aliquot was calculated using the standard $A = \lambda N$ relationship. This value was then scaled to account for the 14.2% ratio noted above to yield a total chemical technetium concentration of 148 ± 12 ppb. The error in the reported concentration is calculated by adding, in quadrature, the 15 minute time error noted above (0.7%), the standard deviation of the five sample aliquots (3.2%), the assumed error in the HPGe detector efficiency calibration (5%), and an assumed additional error to account for incomplete extraction of all chemical technetium despite the initial 100 mL elution (5%). As the ^{99}Mo breakthrough prior to the extraction step was measured to be 2 Bq/MBq, contributions of ^{99m}Tc and ^{99g}Tc arising from decay of breakthrough ^{99}Mo were considered negligible with regards to calculating the total technetium concentration.

3.2.5. Cross section calculations

The direct ^{99m}Tc and ^{99}Mo cross sections, $[\sigma_{mTc}]_{Direct}$ and $[\sigma_{Mo}]$, were calculated from the measured activities of Section 3.2.2.3 using the standard activation formula [13],

$$\sigma_{Direct} = \frac{[A^{EOB}]_{Direct}}{\eta\Phi(1 - e^{-\lambda t_b})}, \quad (3.11)$$

where $[A^{EOB}]_{Direct}$ is the EOB activity of the respective radionuclide due to direct production, η is the number of ^{100}Mo target nuclei per unit area, Φ is the proton current, σ_{Direct} is the energy dependent cross-section for the direct production route, λ is the decay constant for the nuclide and t_b is the bombardment time. To determine the error in the calculated cross sections, errors in foil thickness (5%), HPGe detector efficiency calibration (5%), beam current (5%) and nuclear decay data (1%) were assumed. These errors were added in quadrature to the counting errors described in Section 3.2.2.1.

To evaluate the direct ^{99g}Tc cross section, $[\sigma_{gTc}]_{Direct}$, the total ^{99g}Tc cross section, $[\sigma_{gTc}]_{Total}$ must first be determined. In addition to the direct ^{99g}Tc contribution, the total cross section also includes interfering $^{99m}\text{Tc} \rightarrow ^{99g}\text{Tc}$, $^{99}\text{Mo} \rightarrow ^{99m}\text{Tc} \rightarrow ^{99g}\text{Tc}$, and $^{99}\text{Mo} \rightarrow ^{99g}\text{Tc}$ contributions. This total cross section can be calculated using the total number of ^{99g}Tc nuclei, N_{gTc} in the 1.3 mL sample volume as measured using ICP-MS,

$$[\sigma_{gTc}]_{Total} = \frac{N_{gTc}}{\eta\Phi t_b \epsilon_{ext}}, \quad (3.12)$$

where η and Φ are as described above, and ϵ_{ext} is the technetium extraction efficiency measured using ^{95m}Tc . The $[\sigma_{gTc}]_{Direct}$ was calculated by subtracting the direct ^{99m}Tc and ^{99}Mo cross sections from $[\sigma_{gTc}]_{Total}$,

$$[\sigma_{gTc}]_{Direct} = [\sigma_{gTc}]_{Total} - [\sigma_{mTc}]_{Direct} - [\sigma_{Mo}]. \quad (3.13)$$

In assessing the error for $[\sigma_{^{95}\text{Tc}}]_{\text{Direct}}$, the absolute errors rather than the relative percent error of the three separate terms of equation (3.13) were added in quadrature. Errors in beam current and foil thickness were excluded in this initial calculation. The absolute error of $[\sigma_{^{95}\text{Tc}}]_{\text{Total}}$ was calculated by adding the relative errors, in quadrature, of the ICP-MS calibration error (8%), standard deviation of the three ICP-MS replicate readings (< 1%), nuclear decay data error (1%), and standard deviation of the $^{95\text{m}}\text{Tc}$ monitored extraction efficiency aliquots (1–5%). The absolute errors of $[\sigma_{^{99}\text{Tc}}]_{\text{Direct}}$ and $[\sigma_{\text{Mo}}]$ were determined from the combination of their counting error, HPGe detector efficiency error (5% each), and nuclear decay data error (1% each). Following the addition of the absolute errors for the three terms of equation (3.13), the relative error in foil thickness (5%) and beam current (5%) were then added in quadrature.

3.3. Results and discussion

The cross sections measured in this work for 100% enrichment of ^{100}Mo are reported in Table 3-3.

3.3.1. $^{100}\text{Mo}(\text{p,x})^{99}\text{Mo}$

Figure 3-4 summarizes the $^{100}\text{Mo}(\text{p,x})^{99}\text{Mo}$ cross sections measured in this work. Error bars are included in this figure for the short ^{100}Mo irradiations. Error bars for the long ^{100}Mo and short $^{\text{nat}}\text{Mo}$ irradiations were omitted for clarity. General agreement is noted when comparing with Takács et al. [3], Khandaker et al. [4], Lebeda and Pruszyński [5], and Levkovskij [14]. The cross sections of this work are somewhat higher than the values of Scholten et al. [1] and Lagunas-Solar [15]. The source of this disagreement is unknown.

Table 3-3. Experimental cross sections (in mb) measured in this work assuming 100% ^{100}Mo enrichment.

E_p [MeV]	$^{100}\text{Mo}(p,x)^{99}\text{Mo}$	$^{100}\text{Mo}(p,2n)^{99m}\text{Tc}$	$^{100}\text{Mo}(p,2n)^{99g}\text{Tc}$
8.5 ± 0.1^a	–	37 ± 3	92 ± 14
10.0 ± 0.1^a	0.264 ± 0.036	173 ± 15	317 ± 46
11.3 ± 0.1^a	3.14 ± 0.28	252 ± 22	536 ± 79
12.5 ± 0.1^a	9.89 ± 0.87	282 ± 25	681 ± 92
13.5 ± 0.2^a	20.3 ± 1.8	276 ± 24	630 ± 90
14.6 ± 0.2^a	35.7 ± 3.1	288 ± 25	689 ± 97
15.6 ± 0.2^a	52.1 ± 4.6	293 ± 26	749 ± 107
16.6 ± 0.2^a	74.1 ± 6.5	307 ± 27	807 ± 112
17.5 ± 0.2^a	87.9 ± 7.7	293 ± 26	812 ± 112
10.9 ± 0.6^b	2.47 ± 0.22	254 ± 22	–
11.9 ± 0.2^b	5.81 ± 0.51	270 ± 24	–
12.9 ± 0.5^b	14.1 ± 1.2	299 ± 26	–
14.0 ± 0.2^b	24.1 ± 2.1	283 ± 25	–
14.0 ± 0.2^b	26.4 ± 2.3	312 ± 27	–
15.0 ± 0.2^b	39.3 ± 3.4	294 ± 26	–
16.3 ± 0.2^b	62.7 ± 5.5	310 ± 27	–
17.0 ± 0.3^b	76.0 ± 6.6	281 ± 24	–
17.2 ± 0.8^b	79.7 ± 7.0	266 ± 23	–
17.6 ± 0.8^b	85.4 ± 7.5	249 ± 22	–
17.8 ± 0.4^b	98.1 ± 8.6	315 ± 27	–
8.0 ± 0.2^c	–	11.3 ± 1.2	–
8.9 ± 0.4^c	–	94.1 ± 8.3	–
10.0 ± 0.2^c	–	176 ± 15	–
10.5 ± 0.6^c	–	236 ± 21	–
12.0 ± 0.3^c	–	271 ± 24	–
12.7 ± 0.3^c	10.3 ± 6.2	262 ± 23	–
14.0 ± 0.3^c	18.7 ± 5.4	293 ± 26	–
15.1 ± 0.4^c	37.7 ± 6.0	305 ± 27	–
16.3 ± 0.5^c	55.1 ± 7.6	286 ± 25	–
17.4 ± 0.7^c	71.8 ± 9.6	273 ± 24	–
17.9 ± 0.8^c	82 ± 10	250 ± 22	–

^aLong irradiations on ^{100}Mo ; ^bShort irradiations on ^{100}Mo ; ^cShort irradiations on $^{\text{nat}}\text{Mo}$

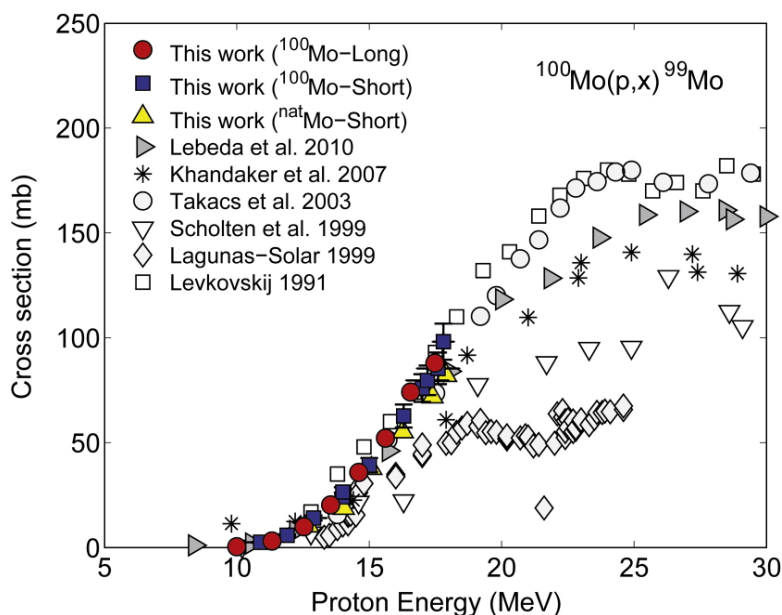


Figure 3-4. Experimental excitation function for the $^{100}\text{Mo}(p,x)^{99}\text{Mo}$ reaction. Error bars for the short ^{100}Mo irradiations are included.

3.3.2. $^{100}\text{Mo}(p,2n)^{99m}\text{Tc}$

Given the reasonable agreement of the $^{100}\text{Mo}(p,x)^{99}\text{Mo}$ cross sections reported in the literature, we do not believe that the large discrepancies noted in the literature for the direct ^{99m}Tc production are a result of errors in beam current or foil thickness. Furthermore, given the good agreement noted in this work for the irradiations of ^{100}Mo and $^{\text{nat}}\text{Mo}$, we have discarded the $^{98}\text{Mo}(p,\gamma)^{99m}\text{Tc}$ reaction pathway when using $^{\text{nat}}\text{Mo}$ as the source for disagreement across the literature. Rather, we suggest that the major source of discrepancy between literature may be attributed to the corrections, or lack thereof, employed in subtracting out the 140 keV contributions which arise both from the decay of ^{99}Mo and the indirect $^{99}\text{Mo} \rightarrow ^{99m}\text{Tc}$ pathway.

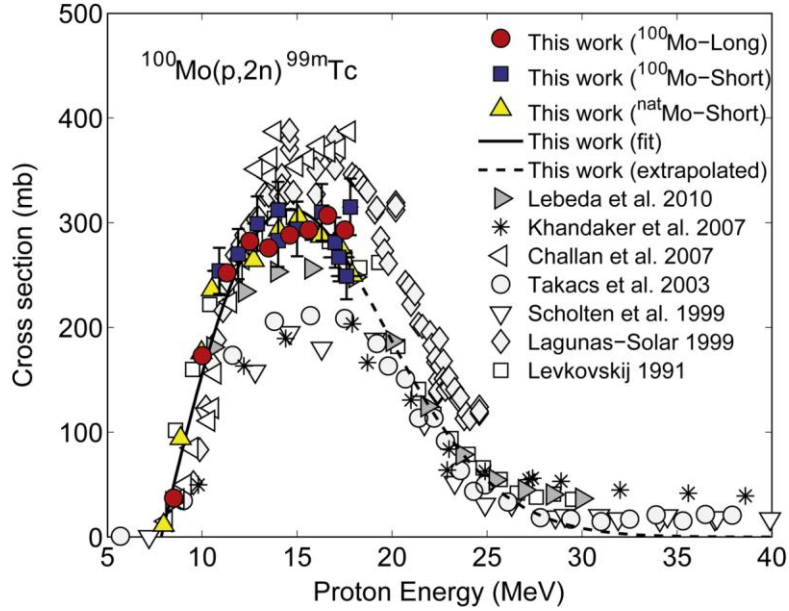


Figure 3-5. Experimental excitation function for the $^{100}\text{Mo}(p,2n)^{99m}\text{Tc}$ reaction. Error bars for the short ^{100}Mo irradiations are included.

Figure 3-5 compares the evaluated $^{100}\text{Mo}(p,2n)^{99m}\text{Tc}$ cross sections of this work to previously published cross section data. Similar to Figure 3-4, error bars for the long ^{100}Mo and short $^{\text{nat}}\text{Mo}$ irradiations were omitted for clarity. For comparison, we have normalized the ^{99m}Tc data of Challan et al. [16] to 100% ^{100}Mo by dividing by 9.63%. A weighted fit combining the three ^{99m}Tc datasets measured in this work was performed using the following function:

$$\sigma = \kappa \left((E_p - E_0) e^{-(E - E_0)^2 / 2s^2} \right). \quad (3.14)$$

κ , E_0 , and s were fitting parameters, and σ and E_p were the measured cross sections and energies, respectively. Weights were taken as the inverse of the cross section variance. The fitting coefficients of ^{99m}Tc are as follows: $\kappa = 75.83 \pm 3.16$ mb/MeV, $E_0 = 7.846 \pm 0.023$ MeV, and $s = 6.801 \pm 0.227$ MeV. This fit is shown as the solid line of Figure 3-5. While we could not evaluate reaction cross sections at $E_p > 18$ MeV for our setup, we were nevertheless interested in gaining insight into the ^{99m}Tc yields at higher energies. The fitting parameters above were

therefore used to extrapolate the fit curve to higher energies as indicated by the dashed line of Figure 3-5.

Working downwards from the highest published cross section data, we observe good agreement with Lagunas-Solar [15] and Challan et al. [16] up to $E_p \sim 12$ MeV. We believe that the elevated ^{99m}Tc cross sections of Lagunas Solar for $E_p > \sim 12$ MeV may be attributed to the incomplete subtraction of the ^{99}Mo 140 keV peak contributions due to the underestimated ^{99}Mo cross sections observed in Figure 3-4. Although Challan et al. mention that they have corrected for the growth and decay of the metastable and ground states, since decay data and cross section information is not provided for ^{99}Mo , it is unclear if corrections were performed to account for interfering ^{99}Mo 140 keV γ -rays or $^{99}\text{Mo} \rightarrow ^{99m}\text{Tc}$ contributions post-EOB. The absence of such corrections would similarly explain the elevated ^{99m}Tc cross sections for $E_p > \sim 12$ MeV.

Excellent agreement is noted between the cross sections measured in this work and the values presented by Levkovskij [14]. The cross sections from this work are however slightly higher, but within two standard deviations, when compared to the values presented by Lebeda and Pruszyński [5].

The results of this work are significantly higher than the cross sections presented by Scholten et al. [1], Takács et al. [3], and Khandaker et al. [4]. Although all authors have noted that corrections were performed to isolate the direct and indirect ^{99m}Tc contributions, since calculation details were not provided within these publications, we cannot identify whether or not the source of discrepancy arose from differences in the calculation procedures.

We describe however two potential correction-related scenarios which may result in decreased ^{99m}Tc cross sections. First, we note that it is important to highlight the distinction between two different ^{99}Mo 140 keV γ -ray intensities: (i) the 4.52% contribution arising from ^{99}Mo itself, and (ii) the overall 140 keV intensity of ^{99}Mo in equilibrium with ^{99m}Tc which was calculated from equation (3.1) to be 90.38%. If the latter intensity were employed in equation (3.3), the total ^{99m}Tc peak contribution would correspondingly be underestimated as per

equation (3.2). While the tabulated nuclear decay data of Khandaker et al. give this intensity as 4.52%, Scholten et al. do not list this intensity although they do make mention of this interfering γ -ray, and Takács et al. list an intensity of 89.43%. A second possible scenario which could give rise to lower calculated cross sections is the assumption that the ^{99m}Tc born from ^{99}Mo is in equilibrium at the time of measurement. At equilibrium, considering only the ^{99m}Tc generated from ^{99}Mo , the $^{99m}\text{Tc}/^{99}\text{Mo}$ activity ratio is 96%. At 4, 8, and 12 hr however, this ratio is 33%, 55%, and 69%, respectively. As such, if equilibrium at the time of measurement were assumed, the indirect contribution of ^{99m}Tc would be overestimated. Consequently, as per equation (3.5), the direct ^{99m}Tc contribution would be underestimated.

Similar to the recent study by Lebeda and Pruszyński [5], we have outlined in extensive detail the corrections and calculations performed in this work for separating the interfering γ -ray contributions. We feel that it is essential to include this information so that correction strategies can be compared in order to resolve discrepancies across the literature.

3.3.3. $^{100}\text{Mo}(p,2n)^{99g}\text{Tc}$

The direct experimental $^{100}\text{Mo}(p,2n)^{99g}\text{Tc}$ cross sections measured in this work are summarized in Figure 3-6. To the best of our knowledge, this is the first experimental measurement of this excitation function. With a peak $^{99m+g}\text{Tc}$ cross section of ~ 1100 mb, the results of this work are in reasonable agreement with the peak cross section noted from the figure of Lambrecht et al., [17] to be on the order of ~ 1100 – 1200 mb. The excitation function of [17] was predicted using the ALICE nuclear model code.

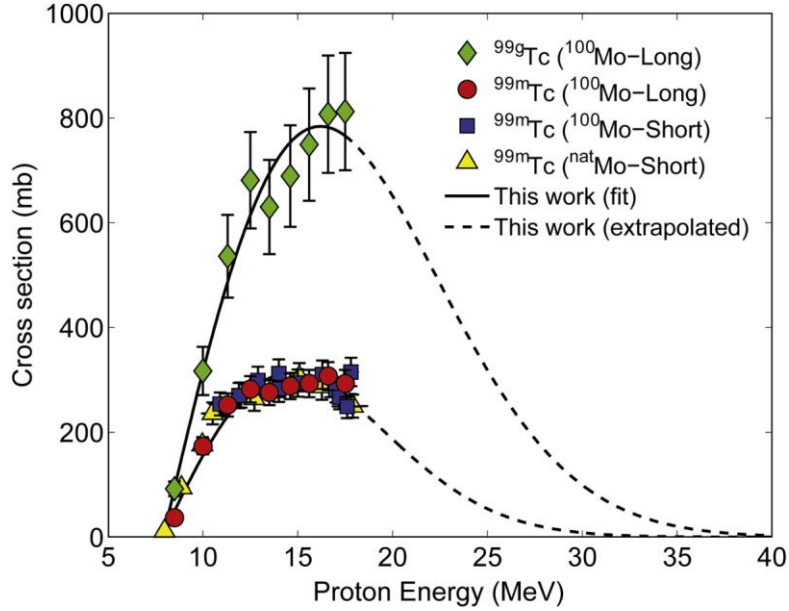


Figure 3-6. Experimental excitation function for the $^{100}\text{Mo}(p,2n)^{99g}\text{Tc}$ and $^{100}\text{Mo}(p,2n)^{99m}\text{Tc}$ reactions.

The curves shown for the ^{99m}Tc data of Figure 3-6 are identical to the curves shown in Figure 3-5. A weighted fit and extrapolation was similarly performed on the ^{99g}Tc data using the fitting function of equation (3.14). The fitting coefficients of ^{99g}Tc are given by: $\kappa = 155.7 \pm 13.4$ mb/MeV, $E_0 = 7.901 \pm 0.095$ MeV, and $s = 8.299 \pm 0.876$ MeV.

The $N_{m\text{Tc}}/N_{m+g\text{Tc}}$ ratio was evaluated by calculating the thick target yields of ^{99m}Tc and ^{99g}Tc using the standard yield formula [18]. In calculating this ratio, we have included contributions from $^{100}\text{Mo}(p,2n)^{99g}\text{Tc}$, $^{100}\text{Mo}(p,2n)^{99m}\text{Tc}$, and $^{100}\text{Mo}(p,2n)^{99m}\text{Tc} \rightarrow ^{99g}\text{Tc}$ during irradiation. All tabulated values were calculated using the fitting coefficients noted above and discrete energy step sizes of 0.1 MeV. Although we have only performed experimental evaluation of the cross sections up to 18 MeV and acknowledge that further experimental studies at higher energies are warranted, we have nevertheless calculated the thick target yields up to 24 MeV based on the extrapolated curves. Given that extrapolation of the ^{99m}Tc data shows generally good agreement with previously published values

at higher energies, as well as the fact that we have used fitting functions of the same form for both ^{99m}Tc and ^{99g}Tc , we feel that extrapolation of the yields is a tenable approach to estimating the yields for higher incident proton energies. Table 3-4 reports the $N_{m\text{Tc}}/N_{m+g\text{Tc}}$ ratio at EOB as well as the ^{99m}Tc thick target yield for the proton irradiation of ^{100}Mo for eight irradiation conditions.

When comparing with yields reported in the literature, the extrapolated thick target yields of 712 MBq/ μAh for $22\rightarrow 10$ MeV calculated in this work are higher than the values of 415 MBq/ μAh for $22\rightarrow 12$ MeV and 629 MBq/ μAh for $25\rightarrow 5$ MeV reported by Scholten et al. [1] and Takács et al. [3], respectively. In examining the $N_{m\text{Tc}}/N_{m+g\text{Tc}}$ ratio, we note that this value varies from 19–31% for the irradiation conditions of Table 3-4. In comparing this ratio with the standard $^{99}\text{Mo}/^{99m}\text{Tc}$ generator setup, we use equation (3.10) along with a correction to account for retention [9] and note that the cyclotron produced ^{99m}Tc shows a similar $N_{m\text{Tc}}/N_{m+g\text{Tc}}$ ratio to a generator eluted at a 24 hr frequency with 5% retention which has $N_{m\text{Tc}}/N_{m+g\text{Tc}} = 26\%$.

Table 3-4. Summary of the EOB thick target $N_{m\text{Tc}}/N_{m+g\text{Tc}}$ ratio and the ^{99m}Tc yields for eight irradiation conditions.

Energy [MeV]	1 Hour Irradiation		3 Hour Irradiation		6 Hour Irradiation	
	Ratio [%]	^{99m}Tc Yield [MBq/ μA]	Ratio [%]	^{99m}Tc Yield [MBq/ μA]	Ratio [%]	^{99m}Tc Yield [MBq/ μA]
11\rightarrow10	31	38	28	103	24	176
12\rightarrow10	30	86	27	232	23	396
14\rightarrow10	30	213	26	571	23	974
16\rightarrow10	29	359	26	964	22	1646
18\rightarrow10	27	502	25	1347	21	2299
20\rightarrow10^a	26	622	24	1670	20	2851
22\rightarrow10^a	25	712	23	1911	19	3262
24\rightarrow10^a	24	771	22	2070	19	3535

^a Results based on extrapolation of measured cross section data

For optimization purposes, saturated thick target ^{99m}Tc yields are reported visually in Figure 3-7 for incident proton energies up to 24 MeV. In attempting to select a target thickness which maximizes yield, but minimizes the enriched ^{100}Mo material costs, contours for the metallic ^{100}Mo thickness required to degrade the respective energy assuming a perpendicular beam orientation have been overlaid on this figure. Looking, for example, at the different energy windows giving rise to a saturated yield of 5 GBq/ μA , the thickness contours of Figure 3-7 suggest that it would be more cost-effective with regards to ^{100}Mo usage to irradiate the target using an energy window of approximately 19→12 MeV rather than an energy window of, for example, 18→10 or 24→15 MeV. Similar energy grid plots could also be produced to compare ^{99m}Tc yields to such parameters as power deposition or ^{99g}Tc coproduction.

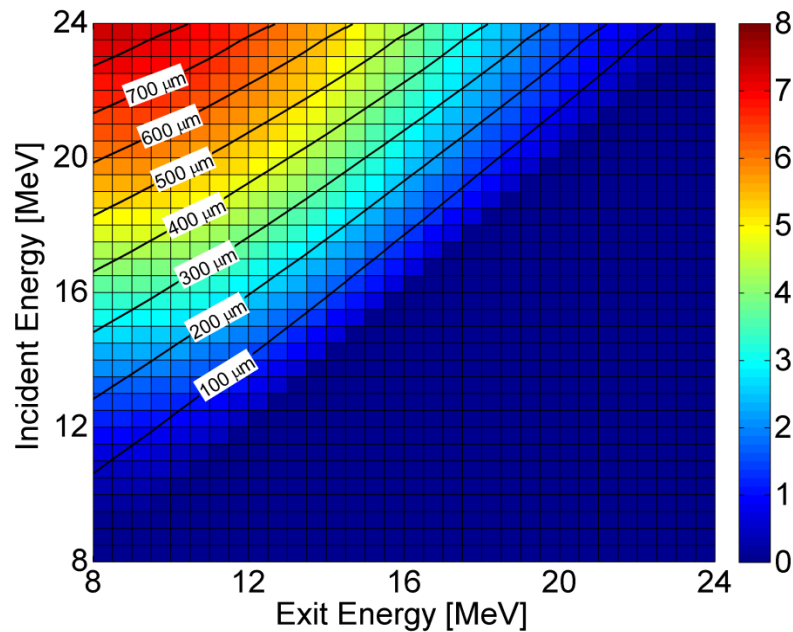


Figure 3-7. Saturated thick target ^{99m}Tc yields [GBq/ μA]. Yields have been calculated based on a 1 MeV step size, and coincide with the line intersections. In other words, the color represents an average of the yield calculated at the four respective intersections. The thickness of metallic ^{100}Mo required to degrade the respective energy assuming a perpendicular beam orientation is also reported.

3.4. Conclusion

This study presents an experimental evaluation of the $^{100}\text{Mo}(p,x)^{99}\text{Mo}$, $^{100}\text{Mo}(p,2n)^{99m}\text{Tc}$ and $^{100}\text{Mo}(p,2n)^{99g}\text{Tc}$ excitation functions in the 8–18 MeV range, measured on the TR-19/9 cyclotron at the Edmonton PET Centre. To the best of our knowledge, this work represents the first experimental cross section measurements for the $^{100}\text{Mo}(p,2n)^{99g}\text{Tc}$ reaction.

Thick target yields calculated from these cross sections suggest that large quantities of cyclotron produced ^{99m}Tc may be possible. For example, a 6 hr irradiation at 500 μA with an energy window of 18 \rightarrow 10 MeV is expected to yield 1.15 TBq of ^{99m}Tc . We have further demonstrated that the ratio of ^{99m}Tc to $^{99m+99g}\text{Tc}$ nuclei is on par with the current $^{99}\text{Mo}/^{99m}\text{Tc}$ generator standard eluted at a 24 hr frequency. These findings thus suggest that the cyclotron production of ^{99m}Tc may be a feasible alternative to the current reactor-based production strategy.

3.5. References

1. B. Scholten, R. Lambrecht, M. Cogneau, H. Ruiz, S. Qaim, Excitation functions for the cyclotron production of ^{99m}Tc and ^{99}Mo , *Appl. Radiat. Isot.* 51 (1999) 69–80.
2. S. Morita, C. Kim, Y. Takaku, R. Seki, N. Ikeda, Determination of technetium-99 in environmental samples by inductively coupled plasma mass spectrometry, *Appl. Radiat. Isot.* 42 (1991) 531–534.
3. S. Takács, Z. Szűcs, F. Tárkányi, A. Hermanne, M. Sonck, Evaluation of proton induced reactions on ^{100}Mo : New cross sections for production of ^{99m}Tc and ^{99}Mo , *J. Radioanal. Nucl. Chem.* 257 (2003) 195–201.

4. M. Khandaker, M. Uddin, K. Kim, Y. Lee, G. Kim, Measurement of cross-sections for the (p,xn) reactions in natural molybdenum, Nucl. Instr. Meth. Phys. Res. B. 262 (2007) 171–181.
5. O. Lebeda, M. Pruszyński, New measurement of excitation functions for (p,x) reactions on ^{nat}Mo with special regard to the formation of ^{95m}Tc , $^{96m+g}\text{Tc}$, ^{99m}Tc and ^{99}Mo , Appl. Radiat. Isot. 68 (2010) 2355–2365.
6. K. Gagnon, S.A. McQuarrie, Investigating the quality of cyclotron-produced technetium-99m: Empire II nuclear cross section modelling, Poster presentation at the 3rd annual Alberta Cancer Research Institute Research Meeting, Banff, AB (2009).
7. National Nuclear Decay Center, Nuclear structure and decay Data (NuDat 2.5) <http://www.nndc.bnl.gov/nudat2/> (accessed 2009).
8. F. Attix, Introduction to radiological physics and radiation dosimetry, Weinheim, Germany: WILEY-VCH Verlag GmbH & Co. KGaA, (2004).
9. Z. Alfassi, F. Groppi, M. Bonardi, J. Goeij, On the “artificial” nature of Tc and the “carrier-free” nature of ^{99m}Tc from $^{99}\text{Mo}/^{99m}\text{Tc}$ generators, Appl. Radiat. Isot. 63 (2005) 37–40.
10. R. Selwyn, R. Nickles, B. Thomadsen, L. DeWerd, J. Micka, A new internal pair production branching ratio of ^{90}Y : The development of a non-destructive assay for ^{90}Y and ^{90}Sr , Appl. Radiat. Isot. 65 (2007) 318–327.
11. IAEA Charged-particle cross section database for medical radioisotope production, Monitor reactions, http://www-nds.iaea.org/medical/monitor_reactions.html (accessed 2009).

12. J.F. Ziegler, M.D. Ziegler, J.P. Biersack, The stopping and range of ions in matter (SRIM code, version 2008.04), <http://www.srim.org/> (accessed 2009).
13. K. Krane, Introductory Nuclear Physics, NJ: John Wiley & Sons, Inc., (1988).
14. V. Levkovskij, Activation cross section nuclides of average masses (A=40-100) by protons and alpha-particles with average energies (E=10-50 MeV), 1991. Data accessed from the NNDC EXFOR database, <http://www.nndc.bnl.gov/exfor/> (accessed 2010).
15. M. Lagunas-Solar, Accelerator production of ^{99m}Tc with proton beams and enriched ^{100}Mo targets, IAEA-TECDOC-1065, IAEA, Vienna, (1999) 87.
16. M. Challan, M. Comsan, M. Abou-Zeid, Thin target yields and EMPIRE-II predictions on the accelerator production of technetium-99m, Nucl. Rad. Phys. 2 (2007) 1–12.
17. R. Lambrecht, T. Sekine, H. Ruiz, ALICE predictions on the accelerator production of molybdenum-99, Appl. Radiat. Isot. 51 (1999) 177–182.
18. S. Qaim, Nuclear data for medical applications: an overview, Radiochim. Acta. 89 (2001) 189–196.

4. Energy evaluation

A version of this chapter was published in:

K. Gagnon, M. Jensen, H. Thisgaard, J. Publicover, S. Lapi, S.A. McQuarrie, and T.J. Ruth, A new and simple calibration-independent method for measuring the beam energy of a cyclotron, *Appl. Radiat. Isot.* 69 (2011) 247–253.

4.1. Introduction

When used for medical radionuclide production, both new and old cyclotrons need to have their beam energy checked periodically. This is not only part of good manufacturing practice and quality assurance, but is also necessary for optimizing target yields and minimizing the radiation dose associated with radionuclide production. There is a need to minimize undesired by-products which result from competing energy-dependent reactions. When producing ^{94m}Tc from the $^{94}\text{Mo}(p,n)^{94m}\text{Tc}$ reaction, the production of contaminant ^{93}Tc via the energy-dependent (p,2n) reaction is an example in which energy validation is important. Although it is often claimed by cyclotron operators that the energy of their machines “never change,” were “locked-in at the factory,” or were “carefully determined at acceptance testing,” from our experience based on periodic evaluation of the proton energy, this is not valid for the majority of present day negative ion cyclotrons. The extraction of negative ion beams by a stripper foil can give useful beam on targets even with substantial orbit centre offsets. Changes in magnet shim or in the distribution of the RF field along the *dees* can cause the orbital centre to drift. Furthermore, the loss of position calibration or damage to extractors and stripper foils can also substantially affect the beam energy. While cyclotrons in nuclear physics institutions often have analyzing magnets with well

characterised energy definition, this diagnostic tool is not feasible for most medical cyclotron configurations as the production targets sit more or less straight on the exit beam port of the cyclotron with little or no further collimation. As such, an off-line approach for evaluating the beam energy of a medical cyclotron is required.

For most applications the simple method of beam range determination will not be accurate enough due to straggling. Long stacks increase straggling, and it can be difficult by conventional “burn” methods to discriminate the Bragg peak end from thermal damage. We therefore investigated a new, simple-to-perform method for evaluating the cyclotron beam energy. By using the universally available dose calibrator, a re-entrant ion chamber used in every nuclear medicine facility, the method we propose is sufficiently sensitive to achieve the necessary precision of a few tenths of an MeV. Furthermore, the proposed method requires neither energy nor efficiency calibration of the detector system being used. The method works for an arbitrary dose calibrator setting. The proposed method was extensively evaluated and tabulated for protons in the 11 to 19 MeV energy range, but it should be straightforward to extend the general principle to protons, deuterons and alphas of other energies.

4.2. Theory

Beam monitor reactions have been extensively published, evaluated, and used for many years, including for example, http://www-nds.iaea.org/medportal/monitor_reactions [1]. The reliable use of these methods however requires access to, and knowledge of, a well calibrated detector system which typically entails an HPGe γ -ray spectroscopy system. When irradiating a single, thin foil, the production of a radionuclide is given by,

$$A = \eta\Phi\sigma(1 - e^{-\lambda t_b}), \quad (4.1)$$

where A is the activity of the nuclide at EOB, η is the number of target nuclei per unit area, Φ is the proton current (protons per unit time), σ is the energy dependent cross-section, λ is the decay constant for the nuclide and t_b is the

bombardment time. If the cross-sections for the reaction of interest are well characterized, then the beam energy may be determined by measuring A and having an accurate knowledge of the η , Φ , λ , and t_b terms.

Due to variations in the foil thickness and/or beam current, an examination of the activity ratio of two isotopes produced simultaneously via competing reactions (e.g. (p,n) and (p,2n)) within a single foil can be beneficial [2, 3],

$$\frac{A_j}{A_k} = \frac{\sigma_j(1 - e^{-\lambda_j t_b})}{\sigma_k(1 - e^{-\lambda_k t_b})}. \quad (4.2)$$

The primary drawback in evaluating the beam energy using either equation (4.1) or (4.2) is that both require absolute quantification of the produced radioactivity. Incorrect or offset efficiency calibration for the detector in question can therefore seriously compromise the results.

As opposed to irradiating a single monitor foil, it has been previously proposed to use a stack of copper foils and then analyse every single foil by high resolution γ -ray spectroscopy for the isotopes ^{62}Zn and/or ^{65}Zn [2, 3, 4, 5]. To overcome the need for γ -ray spectroscopy or high quality efficiency calibrations, this study suggests the irradiation of two monitor foils of the same material interspaced by an energy degrader as illustrated in Figure 4-1. By carefully choosing both the monitor foil material and degrader thickness, the differential activation of the two monitor foils may be used to determine the beam energy.

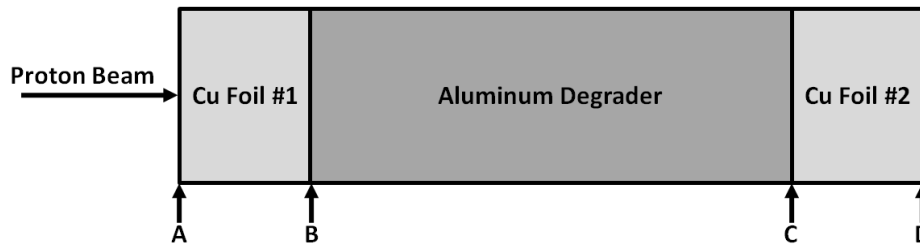


Figure 4-1. The configuration of the two copper foils and aluminum energy degrader irradiated in this experiment. The above figure is not to scale – the copper foil thicknesses have been exaggerated for the purpose of illustration.

The major advantage of examining the ratio of two identical isotopes produced in the two foils, for example, $^{63}\text{Zn}/^{63}\text{Zn}$ as opposed to the $^{63}\text{Zn}/^{62}\text{Zn}$ ratio resulting from proton irradiation of a single copper monitor foil, is that all detector efficiency calibration requirements are eliminated. Furthermore, the exponential factors in equation (4.2) will also cancel as $\lambda_j = \lambda_k$ for the proposed method,

$$\frac{A_{j\text{ Foil1}}}{A_{j\text{ Foil2}}} = \frac{\sigma_{j\text{ Foil1}}}{\sigma_{j\text{ Foil2}}} . \quad (4.3)$$

Through careful selection of the energy degrader thickness, this method can be used efficiently and with high precision. Since this activity ratio may be predicted using well known published recommended cross-section data and the SRIM software package [6], we have developed and included a simple lookup table (Table 4-1) which may be used for monitoring the proton energy given experimental evaluation of the activity ratio.

As an example, we take two 25 μm copper foils which sandwich an 875 μm aluminum degrader. We then compare the differential activation in the two copper foils when we start with an incident proton energy of 15.0 MeV versus starting with an incident proton energy of 15.5 MeV. For these two incident energies, the proton energy at locations B, C, and D of Figure 4-1 were evaluated using the SRIM software package [6]. Overlaid on a plot of the IAEA recommended cross section data for the $^{\text{nat}}\text{Cu}(p,x)^{63}\text{Zn}$ reaction [1], the shaded areas of Figure 4-2 represent the energy loss in the first copper foil, $A \rightarrow B$, the aluminum degrader, $B \rightarrow C$, and the second copper foil, $C \rightarrow D$. As illustrated, the small change in the incident energy from 15.0 to 15.5 MeV yields a measurable change in the ^{63}Zn activity ratio.

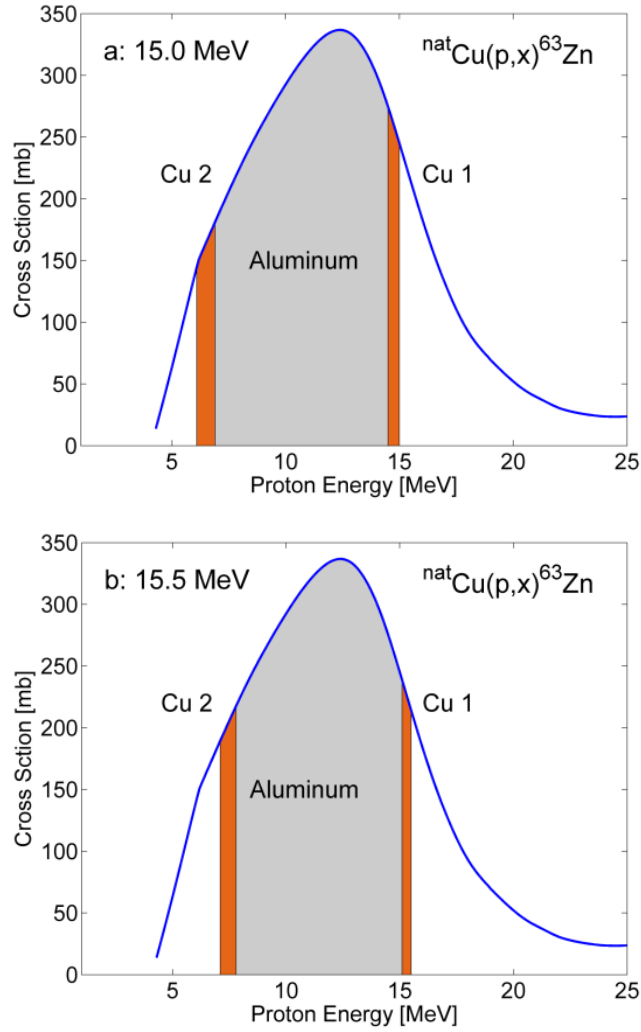


Figure 4-2. A comparison of the ^{63}Zn activation for two 25 μm copper foils and an 875 μm aluminum degrader given incident proton energies of (a) 15.0 MeV, and (b) 15.5 MeV using the IAEA recommended cross-section data [1]. Calculated using the SRIM software package [6], the shaded regions represent the finite energy loss in each of the two copper foils and the aluminum degrader.

4.3. Materials and methods

The proposed method was evaluated by measuring the ^{63}Zn activity ratio produced during the proton irradiation of two copper foils interspaced by an aluminum energy degrader. Initial measurements were performed at the

Edmonton PET Centre (EPC) using a TR-19/9 negative ion variable energy cyclotron (Advanced Cyclotron Systems Inc., Richmond, BC). A set of six additional measurements were also performed using the tandem Van de Graaff at Brookhaven National Lab (BNL) in New York. As the incident proton energy is known with greater accuracy when using an electrostatic accelerator as compared to a cyclotron, the measurements at BNL were performed to serve as a further validation of the proposed method.

4.3.1. Monitor foils

Copper foils were the preferred choice for evaluating the proton energy for this study as the $^{nat}\text{Cu}(p,x)^{63}\text{Zn}$ excitation function is well characterized (IAEA, 2009), and copper foils of sufficient quality and purity ($\geq 99.99\%$) can be purchased from many commercial suppliers including, for example, Alfa Aesar or Goodfellow. As long as the monitor foils are kept relatively thin, so as to minimize the finite energy loss through the foil, the actual thickness of the foils is not of great importance as it may be measured and corrected for. All recommended values given in this manuscript are however based on the use of 25 μm copper monitor foils. To minimize the foil-to-foil variations in purity and thickness and ensure that the two foils are of equal thickness, it is essential that the two foils are cut from the same manufactured sheet or roll. The foil thicknesses in this study, both of aluminum and copper, were found by weight determination to the nearest 0.1 mg using a 10.0 cm x 10.0 cm square of foil. Although the thickness variations across the foils were not measured, we have investigated the impact of small variations in the average thickness by utilizing both the measured and nominal foil thicknesses to determine the proton energy.

4.3.2. Degradation thickness

As noted in Figure 4-3, as the degrader thickness is increased, an increased range in the ^{63}Zn expected activity ratio is observed which thereby increases the sensitivity of the technique.

Striving to achieve a reasonably thick aluminum degrader, it is immediately noted that a single degrader thickness will not be suitable for the entire 11–19 MeV energy range of interest. For example, if we consider a degrader which is sufficiently thick to drop ~10 MeV given $E_p = 17$ MeV, such a degrader would certainly be too thick to allow for activation of the second copper foil given an incident energy of 11 MeV. As such, we have proposed the set of recommended thicknesses given in Table 4-1. These have been broken into nine energy windows between the range of 11–19 MeV. Consequently, to use the recommended data of Table 4-1, it is assumed that there is a rough idea, within approximately 1 MeV, of the proton energy in question.

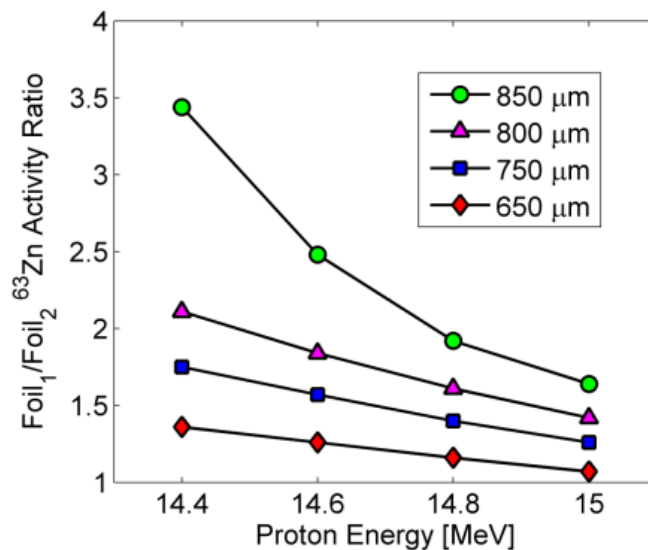


Figure 4-3. The expected ^{63}Zn activity ratio calculated from equation (4.3) as a function of proton energy for aluminum degraders ranging in thickness from 650–850 μm .

In developing the set of recommended degrader thicknesses of Table 4-1, the goal was to utilize, as noted above, a reasonably thick degrader for increased sensitivity. What makes a thickness “reasonable”? If the degrader is too thick, there will be a large difference in the proton energy between the entrance and exit

surface of the second copper foil. Due to large non-linearities in the proton stopping power at low energies, a large difference in energy across the foil is undesired as the technique becomes increasingly susceptible to both thickness non-uniformities and errors in the thickness measurements.

Table 4-1. The recommended aluminum degrader thicknesses and second order curve fitting terms^a.

Aluminum Thickness [μm]	Energy Range [MeV]	Second Order Term “A”	First Order Term “B”	Constant Term “C”	Expected Activity Ratio Range
350	10.8–12.0	1.3811	-6.8958	19.408	1.55–2.50
500	12.0–13.0	0.7058	-4.0449	17.795	1.65–2.85
625	13.0–14.0	0.5352	-3.1150	17.527	1.50–2.85
750	14.0–15.0	0.5223	-2.7947	17.696	1.30–2.40
875	15.0–15.8	0.5254	-2.5192	17.837	1.05–1.80
1000	15.8–16.6	0.7218	-2.8021	18.380	0.80–1.50
1125	16.6–17.4	1.1060	-3.3724	19.029	0.60–1.20
1250	17.4–18.2	2.1607	-4.7938	19.934	0.45–0.85
1375	18.2–18.8	4.5682	-7.3352	21.028	0.35–0.65

^a E_p (MeV) = A r^2 + B r + C, where r is the ⁶³Zn activity ratio between front and back copper foil. The straggling and the energy loss of a nominal 25 μm aluminum vacuum window is included in the calculations. The energy calculated is the energy incident on this vacuum foil.

Using combinations of commercially available nominal aluminum foil thicknesses of 25, 125, and 250 μm , the recommended degrader thicknesses were selected so that the average proton exit energy of the second copper foil was expected to be no less than 5.2 MeV as determined using simulations in SRIM [6]. This value of 5.2 MeV was selected for two reasons. Firstly, this value is 1.0 MeV above the ⁶³Cu(p,n)⁶³Zn reaction threshold [7]. Thus, despite any energy straggling, all protons should have sufficient energy to ensure a suitable interaction probability within the foil. Next, for a 25 μm copper foil, this

minimum exit energy ensures an average energy drop of no greater than 1 MeV between the entrance and exit surface of the second copper foil. We considered this 1 MeV energy drop acceptable, as the IAEA recommended cross-sections (reported in steps of 0.1 MeV) for the $^{nat}\text{Cu}(p,x)^{63}\text{Zn}$ reaction are highly linear ($R^2 > 0.98$) over any floating 1 MeV interval in the energy range of interest for the second copper foil.

4.3.3. Expected activity ratio

A plot of proton energy as a function of the expected activity ratio is required to evaluate the proton energy from the measured activity ratio. In calculating the expected activity ratio, it is first necessary to determine the effective energy within the two copper monitor foils for a given incident energy. This was achieved by simulating 1000 ions in the TRIM module of the SRIM software package [6]. As the copper foils were of finite thickness, the effective energy within the foil was taken as the average between the entrance and exit foil energy. These effective energies were then employed to evaluate the corresponding effective cross-sections within the two monitor foils. This was achieved using polynomial interpolation of the IAEA recommended cross-section data for the $^{nat}\text{Cu}(p,x)^{63}\text{Zn}$ reaction [1]. Finally, the activity ratio was then calculated from equation (4.3) using the effective ^{63}Zn cross-sections of the two copper foils. While uncertainties in the ^{63}Zn activity ratios could not be calculated as there are no uncertainties reported for the IAEA recommended cross section data [1], error in the magnitude of the IAEA cross-section data will not impact the results as it is the shape of the excitation function which dictates the cross-section ratio.

For comparison, the expected activity ratios were determined by simulating the proton energy both using (i) the nominal foil thicknesses reported by the manufacturer, and (ii) the measured foil thicknesses. It is important to note that in addition to the Cu/Al/Cu foil sandwich, a 25 μm aluminum vacuum window is employed as part of the TR-19/9 cyclotron target system. As this

vacuum foil was included in all energy simulations, the energy calculated using the data from Table 4-1 represents the energy incident on this vacuum foil.

4.3.4. Irradiation parameters

A total of twelve irradiations were performed on the TR-19/9 cyclotron. All foils were positioned normal to the incident beam and electrically isolated from the target nose-piece. Foils were irradiated for 300 s with approximately 1 μ A of proton beam current. Since the TR-19/9 cyclotron has a minimum proton extraction energy of 13.7 MeV, the proposed method was evaluated in the 11 MeV range by installing a 375 μ m nominal thickness aluminum degrader adjacent to the target's vacuum window. As good agreement between the nominal cyclotron energy and the measured energy as determined via HPGe spectroscopy methods had been noted previously for a thorough study of the extractor foil in question [8], the proton energies evaluated in this experiment were compared directly with the nominal cyclotron energy.

A total of six proton irradiations were performed using the tandem at BNL. Of these, two of the accelerator's proton energies were blind controls. Since the choice of the aluminum energy degrader thickness requires some idea as to the irradiation energy, it was decided prior to irradiation that one of the blind studies would be performed in the 12.0–12.8 MeV energy range while the other would be performed in the 14.0–14.8 MeV energy range. All BNL irradiations were 300 s in duration and were performed with the foils mounted normal to the incident beam. The irradiation current was set to ~400 nA and was measured just prior to irradiation using a Faraday cup. In contrast to the cyclotron configuration at the EPC, the BNL target station did not require the use of an aluminum vacuum window. Nevertheless, to eliminate the need for applying corrections to the data in Table 4-1, an additional 25 μ m aluminum foil was installed prior to the Cu/Al/Cu sandwich so as to mimic the presence of a vacuum window for the BNL irradiations. The nominal proton energies along with the nominal and measured aluminum and copper thicknesses employed for both the EPC and BNL irradiations are reported in Table 4-2.

Table 4-2. The nominal proton irradiation energies and nominal/measured foil thicknesses.

Nominal Incident Energy	Thickness of Aluminum Vacuum Window and Degradar [μm]		Thickness of Each Copper Monitor Foil [μm]		Thickness of Aluminum Energy Degradar [μm]	
	Nominal	Measured	Nominal	Measured	Nominal	Measured
	10.9 ^{a, b}	400	403.3	25	23.7	350
11.1 ^{a, b}	400	403.3	25	23.7	350	352.2
11.3 ^{a, b}	400	403.3	25	23.7	350	352.2
11.6 ^{a, b}	400	403.3	25	23.7	350	352.2
11.8 ^{a, b}	400	403.3	25	23.7	350	352.2
13.8 ^b	25	25.5	25	23.7	625	628.0
14.6 ^b	25	25.5	25	23.7	750	750.6
15.4 ^b	25	25.5	25	23.7	875	878.2
16.2 ^b	25	25.5	25	23.7	1000	1000.8
17.0 ^b	25	25.5	25	23.7	1125	1128.4
17.8 ^b	25	25.5	25	23.7	1250	1251.0
18.6 ^b	25	25.5	25	23.7	1375	1378.6
11.00 ^c	25	25.5	25	25.6	350	352.2
13.50 ^c	25	25.5	25	25.6	625	628.0
16.00 ^c	25	25.5	25	25.6	1000	1000.8
18.00 ^c	25	25.5	25	25.6	1250	1251.0
(12.0–12.8) ^{c, d}	25	25.5	25	25.6	500	500.4
(14.0–14.8) ^{c, d}	25	25.5	25	25.6	750	750.6

^aEnergy achieved using additional aluminum degrader as minimum extractable energy in TR-19/9 is approximately 13.7 MeV, ^bCyclotron, ^cTandem, ^dBlind

4.3.5. Foil measurements

When irradiating natural copper foils up to 19 MeV, three radionuclide products require examination: ⁶²Zn ($t_{1/2} = 9.186$ hr), ⁶³Zn ($t_{1/2} = 38.47$ min), and ⁶²Cu ($t_{1/2} = 9.67$ min). Although ⁶⁵Zn ($t_{1/2} = 243.66$ d) is also produced during the irradiation of copper foil, given the irradiation conditions and assuming activity assays are performed within ~3 hr post-EOB, the activity of ⁶⁵Zn will be

negligible ($< \sim 1\%$) with respect to the large ^{63}Zn activity produced. Discrimination of the three isotopes only by their half-lives is possible, but somewhat time consuming. An examination of the published cross-sections for these reactions [1, 9] suggests that if we allow the 9.7 min half-life ^{62}Cu contribution to decay, the ^{63}Zn will dominate the dose calibrator readings for proton energies up to approximately 16 MeV. We therefore investigated the possibility of using a combination method whereby, for lower proton energies, we would let the ^{62}Cu decay, and the ratio of the dose calibrator readings at a single time point could be used. For higher proton energies, using multiple measurements obtained at several time points, half-life discrimination of ^{62}Cu , ^{62}Zn , and ^{63}Zn would be possible.

All foil radioactivities were read out using Capintec CRC-15PET and CRC-15W dose calibrators at the EPC and BNL, respectively. As the proposed method is independent of the calibration setting, an arbitrary setting of 100 was employed. All irradiated foils in this study were individually measured in the dose calibrator at approximately 20, 30, 40, 50, 60, 80, 100, 120, 150 and 180 minutes post-EOB with the measurement times recorded to the nearest second.

4.3.6. Calculating the measured activity ratio

Although the single time point evaluation of the ^{63}Zn activity ratio was expected to be applicable only for the lower energy irradiations, the ^{63}Zn activity ratio was calculated for all irradiations by directly using the dose calibrator readings obtained at the 1- and 2- hr time points. These time points were investigated, as opposed to the initial twenty minute measurements, in order to allow for ^{62}Cu decay. As the foil readings for a given irradiation were measured 1–2 minutes apart, a corresponding 1–2 minute ^{63}Zn decay correction was applied so that the readings coincided with a single time point. It is not necessary to decay correct the readings back to EOB as this factor will be the same for both foils, and will therefore cancel when examining the activity ratio.

To discriminate between the three isotopes according to their half-lives and acquire the isotope-corrected ^{63}Zn activity ratio, the ten serial time point readings underwent the following described fitting procedure:

Since the proton energy within the second foil was always expected to be below the threshold for production of ^{62}Cu (11.0 MeV) and ^{62}Zn (13.5 MeV) [7], the ten dose calibrator readings R for this foil were fit using the Curve Fitting Toolbox in MATLAB[®] and the following fitting function:

$$R(t) = K_1 e^{-\lambda_{63\text{Zn}} t} + B \quad (4.4)$$

where t represents the time elapsed since EOB and $\lambda_{63\text{Zn}}$ represents the decay constant for ^{63}Zn . The K_1 coefficient was taken to represent the ^{63}Zn contribution at EOB, while B was taken to represent any background activity. A first attempt at fitting the dose calibrator readings for the first foil was performed using the following double exponential:

$$R(t) = K_1 e^{-\lambda_{63\text{Zn}} t} + K_2 e^{-\lambda_{62\text{Cu}} t} + B \quad (4.5)$$

where K_1 and K_2 were fit parameters. These coefficients were taken to represent the EOB ^{63}Zn and ^{62}Cu contributions, respectively. Since the background term was not expected to vary greatly between the two foils, the B term in equation (4.5) was not a fitting parameter, but instead set to the value obtained for the second foil described by equation (4.4). While curve fitting was only deemed warranted at energies in which significant quantities of ^{62}Zn were produced, this first attempt at curve-fitting was performed without a ^{62}Zn term. This term was initially omitted for the purpose of comparison and assessment of the energy at which accounting for contributions of ^{62}Zn became important.

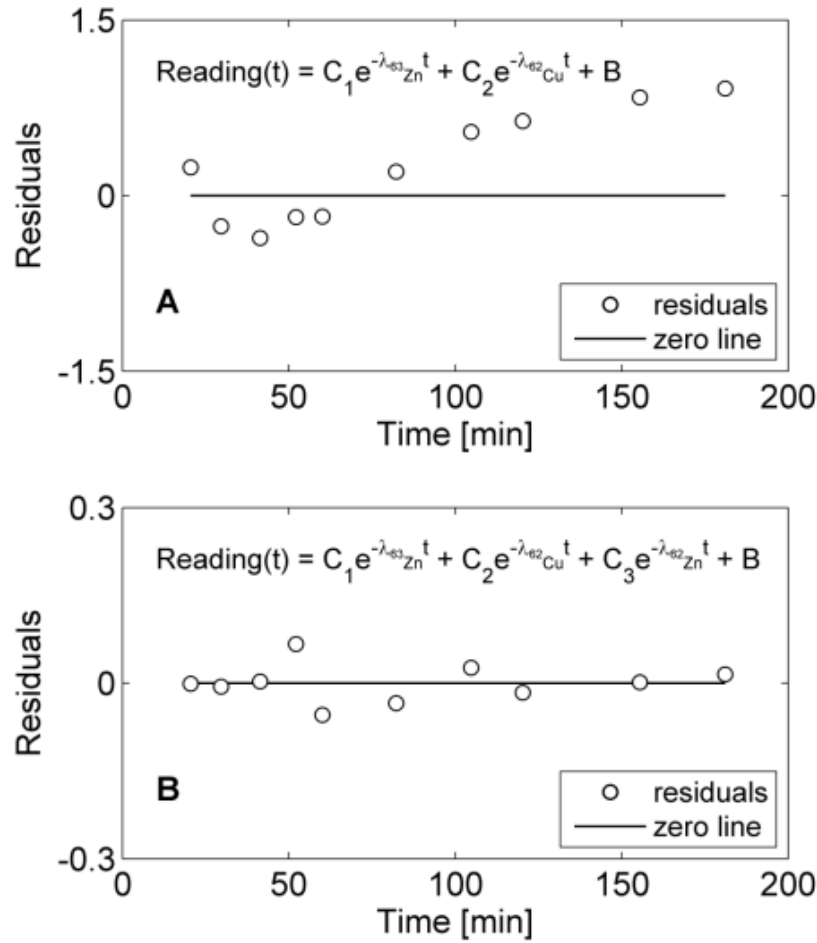


Figure 4-4. A plot of the residuals for the decay curve fitting of the ten dose-calibrator readings for the first copper foil for the 18.6 MeV cyclotron irradiation. Plot A was obtained using the fitting function described in equation (4.5), while B was obtained from the fitting function of equation (4.6).

As this fitting procedure led to undesired systematic trends in the residuals (Figure 4-4A), the data for the first foil were instead described by:

$$R(t) = K_1 e^{-\lambda_{63\text{Zn}} t} + K_2 e^{-\lambda_{62\text{Cu}} t} + K_3 e^{-\lambda_{62\text{Zn}} t} + B \quad (4.6)$$

where K_1 , K_2 and K_3 were fit parameters used to describe the ^{63}Zn , ^{62}Cu , and ^{62}Zn contribution at EOB, respectively. As before, the background B term was taken as

the value obtained by fitting the activity readings of the second foil. By adopting this latter fitting procedure, the systematic trends observed in the residuals were eliminated (Figure 4-4B). Using this fitting method, the ratio of the K_1 coefficients obtained using equations (4.6) and (4.4) was taken as the ratio of ^{63}Zn activity between first and second copper foils.

4.4. Results and discussion

A sample plot of the proton energy as a function of the expected ^{63}Zn ratio calculated from equation (4.3) is given in Figure 4-5 for a nominal 25 μm aluminum vacuum window, a nominal 350 μm aluminum energy degrader, and two nominal 25 μm copper monitor foils. This data was fit using a second order polynomial. The 350 μm aluminum degrader is the thickness recommended in this study for evaluation of proton energies in the 10.8–12.0 MeV range.

Assuming 25 μm copper monitor foils and the presence of a 25 μm aluminum vacuum foil, a list of suggested aluminum proton degrader thicknesses for a wide range of energies is presented in Table 4-1. Since the plots of the expected ^{63}Zn ratios for the other recommended aluminum foil thicknesses are similar in appearance to Figure 4-5, we have omitted the respective figures in this publication. The coefficients of the second order polynomial fits for each of these have, however, been included in Table 4-1. Since a second order polynomial will always have two activity ratios which give rise to a given energy –only one of which is physically meaningful, Table 4-1 also includes the corresponding range of activity ratios which are expected for the energy range of interest.

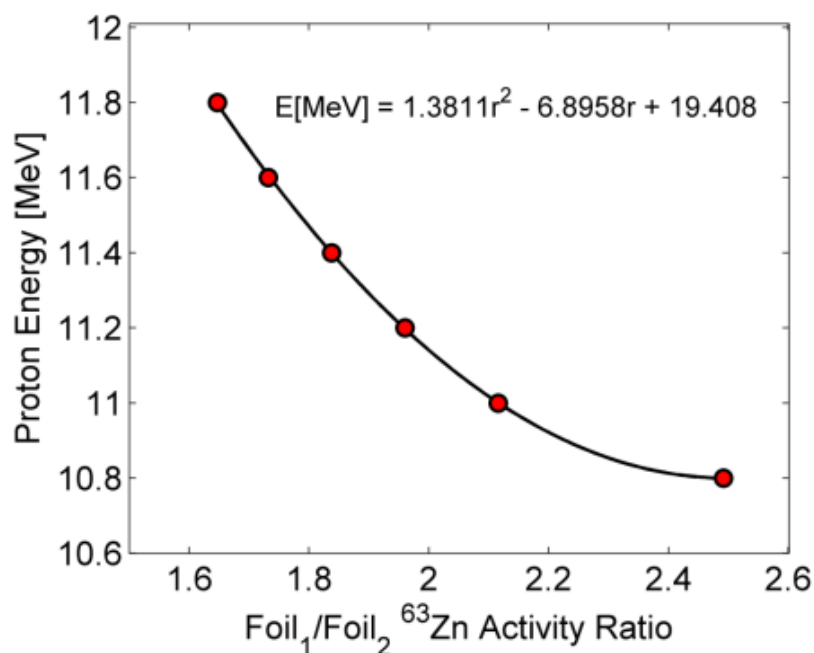


Figure 4-5. A sample plot of the proton energy, E_p , as a function of the expected ^{63}Zn ratio, r . The plot is made with the coefficients from Table 4-1, and assumes a nominal 350 μm aluminum foil and two nominal 25 μm copper monitor foils. The straggling and energy loss of a nominal 25 μm aluminum vacuum window is included in the calculations.

Table 4-3 summarizes the energies evaluated using (i) the half-life discriminated curve-fit based ^{63}Zn ratio, (ii) the single 1 hr time point ^{63}Zn ratio, and (iii) the single 2 hr time point ^{63}Zn ratio. Table 4-3 also includes both the energies evaluated assuming the nominal foil thicknesses as calculated using the second order polynomial data from Table 4-1, as well as the energies evaluated using the measured foil thicknesses.

When examining the blind experiments at 12.3 and 14.4 MeV all measurements agreed within 0.1 MeV of the nominal values. Excellent agreement between the measured and nominal energies was also noted regardless of the strategy employed for determining the ^{63}Zn ratio for proton energies up to 17.0 MeV. We therefore conclude that the half-life discrimination using the ^{63}Zn

curve-fitting method is only essential when the proton energy is greater than 17.0 MeV. We also note that the minor variations from the nominal foil thicknesses used in this study resulted in only minor variations (≤ 0.1 MeV) in the evaluated energy. This suggests that small thickness variations across a foil should similarly have a minor impact on the evaluated energy. Caution must be exercised when using the values from Table 4-1 if the measured foil thicknesses vary by an amount greater than those employed for this work.

Table 4-3. The proton energies evaluated in this experiment using the ^{63}Zn activity ratio.

Nominal Incident Energy	Curve-fit Energy Measurement		1 Hour Energy Measurement		2 Hour Energy Measurement	
	Nominal Thickness	Measured Thickness	Nominal Thickness	Measured Thickness	Nominal Thickness	Measured Thickness
	10.9 ^a	10.9	10.9	10.9	10.9	10.9
11.1 ^a	11.2	11.2	11.2	11.2	11.2	11.2
11.3 ^a	11.4	11.4	11.4	11.4	11.5	11.4
11.6 ^a	11.7	11.6	11.6	11.6	11.7	11.7
11.8 ^a	11.9	11.9	11.9	11.9	12.0	12.0
13.8 ^a	13.9	13.8	13.8	13.8	14.0	13.9
14.6 ^a	14.6	14.6	14.5	14.5	14.6	14.6
15.4 ^a	15.5	15.5	15.4	15.4	15.5	15.5
16.2 ^a	16.4	16.4	16.2	16.2	16.2	16.2
17.0 ^a	17.2	17.2	16.9	16.9	17.0	16.9
17.8 ^a	17.9	17.9	17.5	17.4	17.5	17.5
18.6 ^a	18.5	18.5	18.1	18.1	18.1	18.1
11.00 ^b	10.96	11.00	10.93	10.98	10.97	11.01
13.50 ^b	13.45	13.48	13.47	13.51	13.49	13.53
16.00 ^b	16.10	16.12	15.92	15.94	16.00	16.02
18.00 ^b	18.17	18.18	17.56	17.59	17.69	17.71
(12.0–12.8) 12.3 ^{b,c}	12.32	12.36	12.32	12.36	12.36	12.40
(14.0–14.8) 14.4 ^{b,c}	14.42	14.43	14.36	14.37	14.42	14.44

^aCyclotron, ^bTandem, ^cBlind

4.5. Conclusion

In this work, we have recommended and evaluated a new and simple-to-perform method for measuring the beam energy of a cyclotron. This method was developed with the cyclotron production of medical isotopes in mind, where the ability to easily verify the beam energy to an accuracy of a few tenths of an MeV is of great importance. The proposed method has been found to provide an accurate determination of proton energies in the 11–19 MeV range without the use of complex analytical methods or sophisticated equipment. To facilitate the adoption of this technique into routine evaluation of the cyclotron beam energy, we have included a list of recommended nominal aluminum degrader thicknesses as well as a list of the corresponding curve fit data for evaluation of the proton energy using the measured ^{63}Zn activity ratio. Further studies including the evaluation of $^{\text{nat}}\text{Cu}(p,x)^{62}\text{Zn}$ reaction and the selection of alternative activation foils are warranted for extending this technique into the 20–30 MeV range.

4.6. References

1. IAEA Charged-particle cross section database for medical radioisotope production, Monitor reactions, http://www-nds.iaea.org/medical/monitor_reactions.html (accessed 2009).
2. G. Blessing, W. Brautigam, H.G. Boge, N. Gad, B. Scholten, S.M. Qaim, Internal irradiation system for excitation function measurement via the stacked-foil technique, *Appl. Radiat. Isotop.* 46 (1995) 955–960.
3. B. Scholten, S.M. Qaim, G. Stöcklin, Radiochemical studies of proton induced ^7Be -emission reactions in the energy range of 40 to 100 MeV, *Radiochim. Acta.* 65 (1994) 81–86.

4. J.H. Kim, H. Park, S. Kim, J.S. Lee, K.S. Chun, Proton Beam Energy Measurement with the stacked Cu Foil Technique for Medical Radioisotope Production, *J. Korean Phys. Soc.* 48 (2006) p. 755–758.
5. J.W. Burrage, A.H. Asad, R.A. Fox, R.I. Price, A.M. Campbell, and S. Siddiqui, A simple method to measure the proton beam energy in a standard medical cyclotron, *Australas. Phys. Eng. Sci. Med.* 32 (2009) 92–97.
6. J.F. Ziegler, M.D. Ziegler, J.P. Biersack, The stopping and range of ions in matter (SRIM code, version 2008.03), <http://www.srim.org/> (accessed 2009).
7. National Nuclear Decay Center, Nuclear reaction and decay Q-values (QCalc), <http://www.nndc.bnl.gov/qcalc/> (accessed 2009).
8. M.A. Avila-Rodriguez, J. Rajander, J.-O. Lill, K. Gagnon, J. Schlesinger, J.S. Wilson, S.A. McQuarrie, O. Solin, Proton energy determination using activated yttrium foils and ionization chambers for activity assay, *Nucl. Instr. and Meth. B.* 267 (2009) 1867–1872.
9. S.N. Ghoshal, An Experimental Verification of the Theory of Compound Nucleus, *Phys. Rev.* 80 (1950) 939–942.

5. Recycling ^{100}Mo metal

A version of this chapter was submitted for review in:

K. Gagnon, J. S. Wilson, C. Holt, D. Abrams, A. J. B. McEwan, D. Mitlin, and S.A. McQuarrie, Cyclotron production of $^{99\text{m}}\text{Tc}$: Recycling of enriched ^{100}Mo metal targets, submitted to Applied Radiation and Isotopes (August, 2011).

5.1. Introduction

To achieve $^{99\text{m}}\text{Tc}$ of high radionuclidic purity, highly enriched ^{100}Mo must be employed [1]. The natural abundance of ^{100}Mo is 9.63%, and the high costs associated with the isotopic separation of ^{100}Mo from natural molybdenum makes target recycling very attractive. While the use and recycling of cyclotron-irradiated enriched molybdenum targets has been reported previously in the context of $^{94\text{m}}\text{Tc}$ production [2, 3, 4], to the best of our knowledge, previous recycling studies have been limited to the use of oxide targets. The poor thermal conductivity of molybdenum oxide severely limits the amount of beam current that can be applied to these targets and it would appear that only metallic Mo targets will be amenable to the high power irradiations needed for the large-scale production of $^{99\text{m}}\text{Tc}$. The use of metallic targets would also decrease the possibility of losing expensive target material through melting and volatilization. The challenge in recycling metallic targets using existing technetium extraction strategies is that conversion to molybdate is required before extraction can be performed. Recycling strategies therefore require isolation of the molybdate followed by subsequent conversion to molybdenum metal.

Extraction of technetium from irradiated molybdenum may be carried out using either “wet” or “dry” chemical processes. Wet separation techniques require

oxidative dissolution of the target. Separation of pertechnetate from the bulk molybdate can be achieved using one of many strategies including liquid-liquid extraction [5], ion-exchange chromatography [6], aqueous biphasic extraction chromatography, ABECTM, [7, 8], or electrochemistry [9]. In contrast, the dry thermochromatographic system entails heating of the target under a controlled atmosphere in a quartz tube [2, 3, 4]. The resulting volatile technetium and molybdenum species flow through the tube by addition of a gas and/or by natural convection. Due to the temperature gradient in the tube, and higher vapour pressure of the technetium species, separation is achieved as the two species adsorb at different locations on the quartz tube wall. While thermochromatographic separation of metal targets has been reported, volatility of the technetium was only observed following complete oxidation of the metallic molybdenum through addition of 60–80% O₂ gas [2].

This study presents a strategy to recycle enriched ¹⁰⁰Mo metal targets using ammonium molybdate purification which is based on a careful selection of the ions introduced during target dissolution and basification. Conversion to metallic ¹⁰⁰Mo is then achieved following hydrogen reduction of ammonium molybdate at elevated temperatures.

The isotopic composition of the new vs. recycled ¹⁰⁰Mo was measured using ICP-MS. We also determined the ^{99m}Tc radionuclidic purity, evaluated [^{99m}Tc]TcO₄⁻ quality control (QC) specifications, and compared [^{99m}Tc]MDP uptake images in a healthy rabbit using ^{99m}Tc from a generator and ^{99m}Tc extracted following proton irradiation of recycled ¹⁰⁰Mo. While it should be possible to adapt the proposed recycling methodology to a variety of separation strategies, the existing ABEC separation strategy was selected as this separation scheme was reported to give high ^{99m}Tc recovery, in high radiochemical purity, and did not require the use of organic solvents [7].

Although the present study employs pressed metal powder targets, in a parallel project at the University of Alberta, sintered ¹⁰⁰Mo metal targets are under development to achieve more efficient and structurally stable high power targets.

Since it has been reported that sintered molybdenum prepared from the reduction of ammonium molybdate showed an increased density over sintered molybdenum prepared following reduction of MoO₃ [10], the proposed recycling strategy focuses on isolation of the dissolved ¹⁰⁰Mo in the form of ammonium molybdate.

5.2. Materials and methods

5.2.1. Target irradiation

Four 99.27% enriched (Isoflex) ¹⁰⁰Mo metal targets were prepared by hydraulically pressing ¹⁰⁰Mo powder into a grade 6061 aluminum¹ target plate having an elliptical well with semi-axes of 5 mm x 10 mm. The target was oriented at 30 degrees to the beam, and irradiations were performed on the variable energy TR-19/9 Cyclotron (Advanced Cyclotron Systems Inc., Richmond, BC) at the Edmonton PET Centre (Edmonton, Alberta).

The goal of this study was to evaluate a strategy for metallic molybdenum recycling and not to produce large quantities of ^{99m}Tc. Since any coproduced ⁹⁹Mo cannot be chemically separated from ¹⁰⁰Mo, efforts were made to limit the production of ⁹⁹Mo by reducing the nominal proton extraction energy of 14.3 MeV to 12.1 MeV using an aluminum degrader. By reducing the irradiation energy, we were able to completely decay the samples within a few weeks post-irradiation rather than waiting a month, or more. This consequently expedited this preliminary recycling study as the reduction furnace used for these experiments was located off-site at the University of Alberta's Department of Chemical and Materials Engineering. The irradiation at 12 MeV, as opposed to a higher energy, is not expected to affect the recycling efficiency.

In considering the exit energy, based on the ¹⁰⁰Mo mass and effective thickness at an irradiation angle of 30 degrees, the target was sufficiently thick to degrade the proton energy to ~6.5 MeV as calculated using the SRIM software

¹ Percent by weight [11]: Si (0.40–0.8); Fe (≤ 0.7); Cu (0.15–0.40); Mn (≤ 0.15); Mg (0.8–1.2); Cr (0.04–0.35); Zn (≤ 0.25); Ti (≤ 0.15); Others each (≤ 0.05); Others total (≤ 0.15); Al (remainder)

package [12]. This value was well below the $^{100}\text{Mo}(p,2n)^{99\text{m}}\text{Tc}$ reaction threshold [13]. Thicker ^{100}Mo was not warranted as this would not have resulted in the production of any additional $^{99\text{m}}\text{Tc}$. The irradiation currents were verified using a titanium monitor foil which was located adjacent to the vacuum window.

Following recycling of the ^{100}Mo metal, three ^{100}Mo targets were once again prepared and irradiated as described above. A summary of the irradiation conditions and target masses of both the new and recycled ^{100}Mo targets is given in Table 5-1. Deviations from the irradiation conditions of 20 μA and 80 minutes occurred when rabbit imaging studies were performed as slightly higher currents were needed to achieve $^{99\text{m}}\text{Tc}$ yields of at least 2 GBq. This was the minimum yield required to adhere with the existing clinical standard operating procedures outlined by the Edmonton Radiopharmaceutical Centre for rabbit imaging of radiopharmaceuticals using generator-based $^{99\text{m}}\text{Tc}$.

Table 5-1. Irradiation conditions for new (N) and recycled (R) ^{100}Mo metal targets.

Sample ID	Irradiation Current [μA]	Irradiation Time [min]	Mass of ^{100}Mo [mg]
1-N	20	80	186
2-N	20	79	175
3-N	30	72	182
4-N	20	80	175
			Mean: 180 ± 5
1-R	20	80	174
2-R	30	60	177
3-R	25	80	178
			Mean: 176 ± 2

5.2.2. Target dissolution

Following irradiation, the pressed metallic molybdenum targets, including the Al plate, were heated in a beaker at 50–60 °C for 5 minutes. The molybdenum was then dissolved by adding 5 mL of fresh 29–32% w/w H₂O₂ (Alfa Aesar, ACS Grade). After leaving the H₂O₂ to react for five minutes without agitation, 1 mL of 3M (NH₄)₂CO₃ (Alfa Aesar, ACS Grade) was added to basify the solution. After ~1–2 minutes and visual inspection to ensure a pale yellow color of the solution, as opposed to dark red, the solution was removed from the heat and left to sit for ~1 minute. Since it is reported [14] that in low hydrogen peroxide concentrations a yellow diperoxomolybdate species is formed, while a large hydrogen peroxide excess leads to formation of a brownish-red tetraperoxomolybdate species, we have attributed the observed color change to decomposition of excess hydrogen peroxide. The solution was then poured into an open-ended 30 mL syringe preloaded with 1 mL of 3M (NH₄)₂CO₃. The dissolution beaker was further rinsed with 5 mL of 0.5 M (NH₄)₂CO₃ and poured into the 30 mL syringe.

The (NH₄)₂CO₃ salt was selected for two reasons. First, it was important to select a biphasic-forming anion such as CO₃²⁻ [8] for compatibility with the ABEC resin. Second, in developing a strategy for ^{99m}Tc extraction which is conducive to ¹⁰⁰Mo recycling, we have limited the solutes to volatile salts to facilitate evaporative purification of the ammonium molybdate.

5.2.3. ^{99m}Tc/¹⁰⁰Mo separation

ABEC resin is capable of differentiating between ionic species based on charge and size from strongly ionic solutions that favour biphasic properties [8]. It has been demonstrated that salts of pertechnetate and molybdate ions can be separated from strongly ionic solutions due to selective retention of the pertechnetate ion on the ABEC resin. The pertechnetate is subsequently washed off of the resin with water.

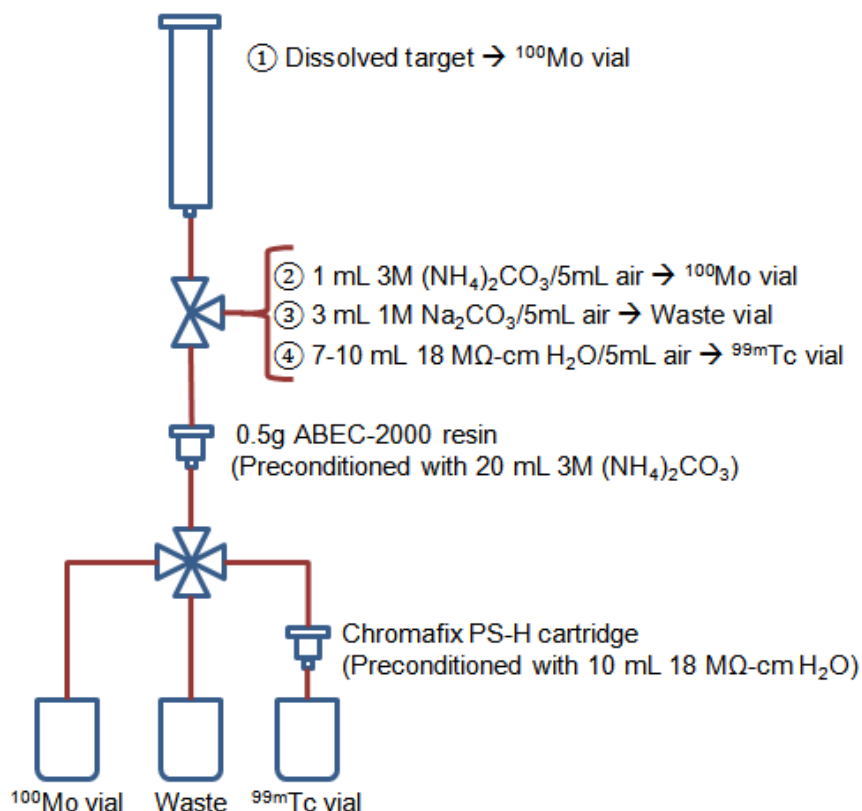


Figure 5-1. A schematic of the $^{99\text{m}}\text{Tc}$ separation strategy using ABEC-2000 resin.

Technetium was extracted by passing the dissolved, oxidized target solution through a cartridge of 100–200 mesh ABECTM-2000 resin (Eichrom) preconditioned with 20 mL of 3 M $(\text{NH}_4)_2\text{CO}_3$. A new resin cartridge was prepared for each separation and 484 ± 13 mg of resin was used for the new ^{100}Mo , while 484 ± 2 mg was used for the recycled ^{100}Mo . The ABEC resin retains the [$^{99\text{m}}\text{Tc}$]pertechnetate while the enriched [^{100}Mo]molybdate is eluted in the initial high ionic fraction. The line and resin were rinsed with 1 mL of 3 M $(\text{NH}_4)_2\text{CO}_3$ to maximize ^{100}Mo recovery and then cleared with 5 mL of air. Next, residual ammonia on the resin was removed by eluting with 3 mL of 1 M Na_2CO_3 (Aldrich, ACS Grade) followed by 5 mL of air into a waste vial. Finally, [$^{99\text{m}}\text{Tc}$]pertechnetate was eluted from the resin using 7–10 mL of 18 M Ω -cm H_2O followed by 5 mL of air and neutralized by passage through a Chromafix[®] PS-H

strong cation exchange (SCX) cartridge preconditioned with 10 mL 18 M Ω -cm H₂O. Process times from start of dissolution to final isolated [^{99m}Tc]pertechnetate solution were less than 30 minutes. A schematic of the separation strategy is given in Figure 5-1.

An aliquot of the extracted [^{99m}Tc]TcO₄⁻ was removed for QC evaluation. The remaining [^{99m}Tc]TcO₄⁻ which ranged from 1.5–2.5 GBq was used for radiopharmaceutical labelling studies.

An aliquot from the ¹⁰⁰Mo collection vial was also removed for radionuclidic impurity analysis. This primary ¹⁰⁰Mo collection vial was set aside to decay. For the purpose of maximizing the ¹⁰⁰Mo recovery, the original target dissolution beaker was once again rinsed, this time with 10 mL of 0.5 M (NH₄)₂CO₃. This secondary ¹⁰⁰Mo rinse vial was also set aside to decay.

5.2.4. Molybdate isolation

The four sets of primary collection and rinse vials were pooled for ¹⁰⁰Mo recycling. These samples were gravity-fed through a column of approximately 4 g of pre-conditioned ABEC-2000 resin to minimize any residual technetium. These empty collection and rinse vials were further rinsed with 5mL of 3M (NH₄)₂CO₃ and once again gravity-fed through the column. The solution was then passed through a 0.22 μ m (Millex[®]-GP) filter to eliminate any particulate matter.

A strategy for evaporating the water and volatile salts without heating was required as ammonium molybdate, the preferred form of ¹⁰⁰Mo for reduction prior to sintering [10], is reported to decompose in hot water [15]. This was accomplished effectively through lyophilisation of the ¹⁰⁰Mo ammonium molybdate solution (Labconco, 12 L, Model 77540).

Molybdenum solutions may be contaminated with additional cations such as aluminum, copper, cobalt, zinc, etc., resulting from impurities in the aluminum target plate and/or from the use of a different target backing such as copper. It may be possible to purify these contaminants via ion exchange chromatography. Another possible purification scheme that we propose includes the addition of

nitric acid, whereby separation may be achieved by filtration or centrifugation based on the relative solubility [15] of ammonium molybdate and contaminant nitrates in alcohol.

5.2.5. Molybdenum reduction

The isolated ammonium molybdate powder was divided into three tungsten boats (25.4 mm W x 58.8 mm L x 2.4 mm deep, Ted Pella, Inc.), and placed into a tube furnace (74 mm ID Carbolite, TZF 16/610). The reduction of ammonium molybdate to molybdenum metal at elevated temperatures, as described by Gupta [16], is a three-step process which includes decomposition of ammonium molybdate to MoO_3 , hydrogen reduction of MoO_3 to MoO_2 , and finally hydrogen reduction of MoO_2 to Mo metal. Gupta noted however that the conversion of MoO_3 to MoO_2 is an exothermic process, and if excessive heat evolution occurs, the local temperature may result in volatilization of MoO_3 . Significant losses of the enriched target material were avoided by limiting the reaction rate for the MoO_3 to MoO_2 step by using 1% H_2 gas in N_2 (Praxair certified standard) and maintaining a 2 °C/min temperature ramp rate. Once beyond 750 °C, the temperature whereby the MoO_3 to MoO_2 reduction was considered to be completed, the flow rates were increased, and the atmosphere set to Grade 5.0 UHP hydrogen.

Table 5-2 and Figure 5-2 outline the programmed and measured temperature profiles, respectively. Steps 1, 2, and 3, were designed to decompose the ammonium molybdate, and reduce both MoO_3 , and MoO_2 , respectively. Step 4 was in place to ensure complete reduction prior to cooling under hydrogen in Step 5, and finally argon in Step 6.

Table 5-2. Summary of reduction temperatures/atmospheres implemented in this ^{100}Mo study.

Step	Temperature Range[°C]	Programmed Temperature Rate [°C/min]	Atmosphere	Nominal Flow Rate [sccm] ^a
1	25→500	5	1% H ₂ in N ₂	500
2	500→750	2	1% H ₂ in N ₂	500
3	750→1100	5	100% H ₂	1000
4	1100 (hold x 1hr)	0	100% H ₂	1000
5	1100→400	-5	100% H ₂	1000
6	400→25	-5	100% Ar	1000

^a standard cubic centimetres per minute

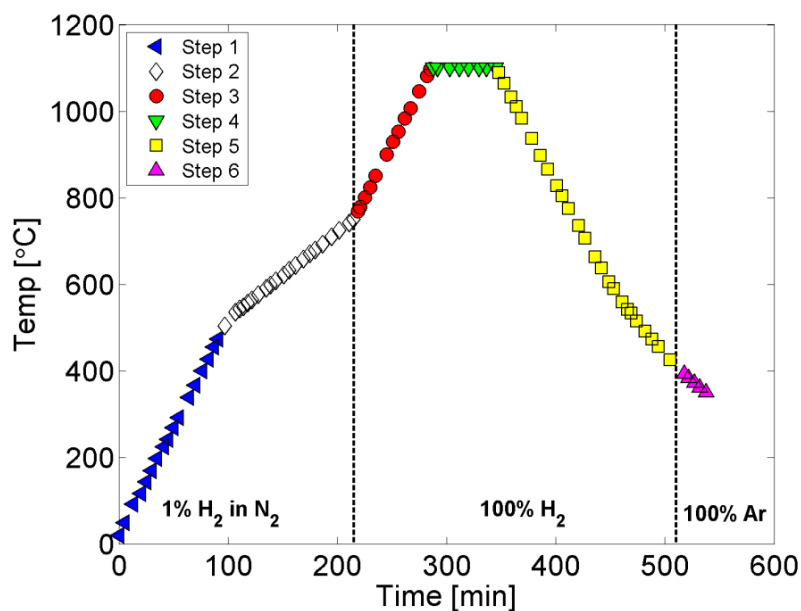


Figure 5-2. The temperature profile measured during the reduction of [^{100}Mo]ammonium molybdate to metal.

Reduction of the ammonium molybdate to molybdenum metal powder was confirmed by powder x-ray diffraction (XRD) on samples of the isolated ^{100}Mo

both pre/post reduction. XRD experiments were performed on a Bruker AXS diffractometer (Bruker Discover 8) using a Cu-K α radiation source ($\lambda = 1.5406\text{\AA}$) that was monochromated using a single Gobel mirror. The diffractometer is equipped with a HiStar general area 2-dimensional detection system (GADDs) with a sample–detector distance of 15 cm. The data from the XRD database on EVA software were used for peak identification. XRD was also performed on commercially available samples of ^{100}Mo metal (Isoflex), $^{\text{nat}}\text{MoO}_3$ (Alfa Aesar) and $^{\text{nat}}\text{MoO}_2$ (Alfa Aesar) for comparison.

5.2.6. Molybdenum isotopic composition

The molybdenum isotopic composition was evaluated via ICP-MS. The ^{100}Mo samples were prepared by dissolving approximately 1 mg of enriched ^{100}Mo metal in 0.5 mL 29–32% w/w H_2O_2 . These solutions were then diluted with 18 M Ω -cm H_2O to give final ^{100}Mo concentrations of approximately 1 $\mu\text{g/mL}$.

ICP-MS was performed using a Perkin Elmer Elan 6000 at the University of Alberta’s Radiogenic Isotope Facility. Measurements employed 35 sweeps per reading, a 20 ms dwell time, 3 replicates, and a one minute wash between all samples. The count rates were taken as the average of the 3 replicates followed by blank subtraction. ICP-MS analysis was repeated using a 100-fold sample dilution to identify possible saturation effects of the $m/z = 100$ reading. An ^{115}In internal standard was used to correct for system drift. Saturation effects were considered negligible as the difference between the ^{100}Mo count rate for the X1 and X100 dilutions was less than 2.5% which was in agreement with the relative standard deviation of the 3 reading replicates.

5.2.7. Radionuclidic analysis

The relative radionuclidic impurities in the $\sim 1\text{--}20\ \mu\text{L}$ ^{100}Mo and $^{99\text{m}}\text{Tc}$ aliquots were determined via γ -ray spectroscopy using an HPGe detector (Ortec model GEM35P4-S). Samples were placed on a rigid stand 25 cm from the detector end cap, and dead times maintained below 5%. In attempt to capture both shorter and longer lived impurities, aliquots were assayed according to the

following live time schedule: ^{100}Mo x 1 hr, $^{99\text{m}}\text{Tc}$ x 1 hr, $^{99\text{m}}\text{Tc}$ x 10 hr, $^{99\text{m}}\text{Tc}$ x 1 hr, and ^{100}Mo x 10 hr. Acquisitions typically commenced within 1–5 hr post-EOB. The detector was calibrated at the fixed 25 cm geometry using NIST traceable calibration sources (Eckert and Ziegler) of ^{22}Na , ^{54}Mn , ^{57}Co , ^{60}Co , ^{109}Cd , ^{133}Ba and ^{137}Cs . All sample activities were corrected for decay during counting time and decay to EOB as described by Selwyn et al. [17]. The decay data utilized to calculate the activity of the radionuclides was obtained from the NNDC NuDat database [18]. Errors in reported activity were taken by adding in quadrature a 5% assumed detector efficiency calibration error, counting error assuming Poisson statistics, and the peak fitting uncertainty as given by the Ortec Gamma Vision v. 6.01 software.

5.2.8. $^{99\text{m}}\text{Tc}$ Radiochemical analysis

The extracted $[\text{}^{99\text{m}}\text{Tc}]\text{TcO}_4^-$ was evaluated for pH, aluminum ion breakthrough via the aurintricarboxylic acid spot test, and radiochemical purity via silica gel instant thin layer chromatography, ITLC, in 0.9% saline.

The *in vivo* uptake of MDP labelled with $^{99\text{m}}\text{Tc}$ from the proton irradiation of recycled ^{100}Mo vs. generator produced $^{99\text{m}}\text{Tc}$ were compared by preparing 2 GBq of MDP (MDP-21, Edmonton Radiopharmaceutical Centre) from each of the $^{99\text{m}}\text{Tc}$ sources. Despite a previous report by Christian et al. [3] which noted that that normal glassware should be avoided during the separation of technetium from molybdenum as boron contamination of the basic medium may cause problems with some of the pharmaceutical kit preparations, standard borosilicate glassware was employed in these studies. QC of the $[\text{}^{99\text{m}}\text{Tc}]$ -labelled MDP included evaluation of colloidal technetium using silica gel ITLC in 0.9% saline, and free pertechnetate using Whatman 31 ET chromatography paper in acetone.

The same rabbit was used for both $^{99\text{m}}\text{Tc}$ scans and imaged 6 days apart. In each study, the rabbit was injected with 40 MBq of MDP in 0.2 mL, and imaged two hours post-injection. Just prior to imaging, the non-anesthetised rabbit was placed into a Plexiglas restraint, and the bladder uptake masked with a lead plate.

Images were acquired at 256 x 256 and 16 bits/pixel on an ADAC Argus single head gamma camera using a LEGP collimator. Corresponding to imaging times of 8.2 and 9.6 minutes for the generator and cyclotron ^{99m}Tc , respectively, acquisitions were terminated at 500 kCts. This time difference may be attributed to slight differences in the total injected activity and/or bladder uptake. All animal experiments were carried out in accordance with guidelines of the Canadian Council on Animal Care and were approved by the local animal care committee of the Cross Cancer Institute.

5.3. Results

5.3.1. Molybdenum reduction and recovery

After correcting for controlled sampling of 53.5 mg ammonium molybdate prior to reduction for the purpose of analysis by XRD, an overall ^{100}Mo metal to metal recovery of 87% was obtained in this study. The XRD results of Figure 5-3 confirm reduction to the metal as indicated by absence of peaks corresponding to the MoO_3 or MoO_2 intermediary products in the final reduced ^{100}Mo sample. No efforts were made to differentiate between the $(\text{NH}_4)_2\text{MoO}_4$, $(\text{NH}_4)_2\text{Mo}_2\text{O}_7$ or $(\text{NH}_4)_6\text{Mo}_7\text{O}_{24}\cdot 4\text{H}_2\text{O}$ forms of the starting ammonium molybdate powder, however reference peaks for the ammonium molybdate tetrahydrate (27-1013 Space Group P21/c, $a=8.39340$, $b=36.17$, $c=10.4715$, $\beta = 115.96$) are reported for comparison. Reference peaks for MoO_2 (32-0671 Space Group P21/n, $a=5.60680$, $b=4.85950$, $c=5.53730$, $\beta=119.37$), MoO_3 (05-0508 Space Group Pbnm, $a=3.962$, $b=13.858$, $c=3.697$), and Mo metal (42-1120 Space Group Im-3m, $a=3.1372$) are also reported. The high radiation fields of the irradiated targets, as well as the multiple potential forms of ammonium molybdate precluded the assessment of the efficiency of each individual step of the outlined cycle for this work. Nevertheless, based on the relative mass abundance of molybdenum in the various forms of ammonium molybdate, we conclude that the efficiency of the reduction step was greater than 95%.

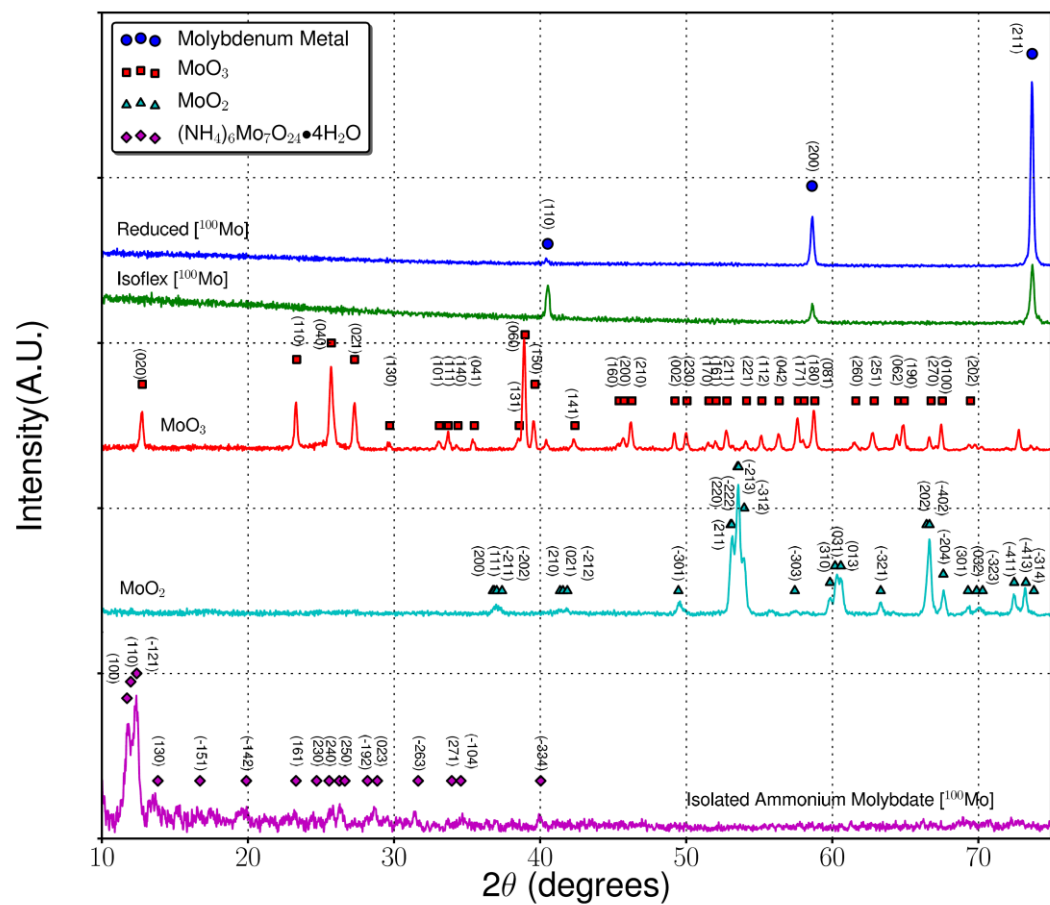


Figure 5-3. Powder XRD of the isolated and reduced [¹⁰⁰Mo] ammonium molybdate, with comparison XRD of commercially available ¹⁰⁰Mo metal (Isoflex), ^{nat}MoO₃ (Alfa Aesar) and ^{nat}MoO₂ (Alfa Aesar).

5.3.2. Molybdenum isotopic composition

Evaluation of the molybdenum isotopic composition was considered important for two reasons. First, due to the wide array of nuclear reaction schemes which may give rise to molybdenum isotopes a possibility exists that the molybdenum composition may change by virtue of the irradiation itself. These include, for example, the direct production routes such as the $^{100}\text{Mo}(p,t)^{98}\text{Mo}$ reaction (Q-value = -5.7 MeV) or indirect production routes such as the $^{100}\text{Mo}(p,\alpha)^{97}\text{Nb}\rightarrow^{97}\text{Mo}$ reaction (Q-value = 4.3 MeV). Second, we were concerned with the introduction of $^{\text{nat}}\text{Mo}$ impurities present in the solvents used for target dissolution and $^{99\text{m}}\text{Tc}$ extraction. As shown in Table 5-3, no changes in the molybdenum isotopic composition between new and recycled ^{100}Mo were observed. The reason for the discrepancies between our measured enrichment and the enrichment reported by the Isoflex certificate of analysis (COA) is unknown.

Table 5-3. The nominal (Isoflex COA) and measured percent isotopic composition for new and recycled ^{100}Mo .

	^{92}Mo	^{94}Mo	^{95}Mo	^{96}Mo	^{97}Mo	^{98}Mo	^{100}Mo
Measured (New)	0.03	0.02	0.04	0.05	0.04	0.45	99.37
Measured (Recycled)	0.03	0.02	0.04	0.05	0.04	0.45	99.37
Nominal – Isoflex COA (New)	0.06	0.03	0.04	0.05	0.08	0.47	99.27

5.3.3. $^{99\text{m}}\text{Tc}$ Radionuclidic analysis

While impurities of $^{94\text{g}}\text{Tc}$, $^{95\text{g}}\text{Tc}$, and $^{96\text{g}}\text{Tc}$ were observed, long-lived $^{95\text{m}}\text{Tc}$ and $^{97\text{m}}\text{Tc}$ could not be detected. The $^{94\text{g}}\text{Tc}$, $^{95\text{g}}\text{Tc}$, and $^{96\text{g}}\text{Tc}$ impurities were therefore evaluated to determine whether the technetium radionuclidic impurities in the $^{99\text{m}}\text{Tc}$ fraction changed following recycling. Table 5-4 reports the weighted average [19] of the decay corrected EOB activities for these three technetium impurities. Each impurity is individually reported as a percentage of the total

^{99m}Tc activity. As per Table 5-4, impurities of both new and recycled ^{100}Mo are in agreement within two standard deviations.

Table 5-4. Percent of impurity activity to ^{99m}Tc activity at EOB for new and recycled ^{100}Mo targets.

	^{94g}Tc	^{95g}Tc	^{96g}Tc
Half-life	293 min	20.0 hr	4.28 d
New (No. = 4) [%]	0.019 ± 0.002^a	0.040 ± 0.002	0.015 ± 0.001
Recycled (No. = 3) [%]	0.023 ± 0.002	0.043 ± 0.002	0.016 ± 0.001

^aNo. = 3 (^{94g}Tc not evaluated for sample 2-N [assayed > 24 hr post-EOB due to an untimely power outage]).

The photopeaks corresponding to the ^{97}Nb ($t_{1/2} = 72.1$ min) and ^{99}Mo ($t_{1/2} = 65.94$ hr) radionuclidic contaminants were clearly visible in the ^{100}Mo fractions (Figure 5-4), but were not observed in the final ^{99m}Tc fractions. This observation confirms that the chemical forms of niobium and molybdenum in this experiment are not retained by the ABEC resin. However, the contaminants ^{181}Re ($t_{1/2} = 19.9$ hr) and ^{182m}Re ($t_{1/2} = 12.7$ hr) which were < 0.05% and < 0.5% of the ^{99m}Tc EOB activity, respectively, were observed in the ^{99m}Tc extracted following irradiation of recycled ^{100}Mo , but not for the new ^{100}Mo . This source of Re is attributed to contamination and subsequent activation from the tungsten boats used for the reduction. No further non-technetium gamma emitting radionuclidic contaminants were identified in the ^{99m}Tc aliquots.

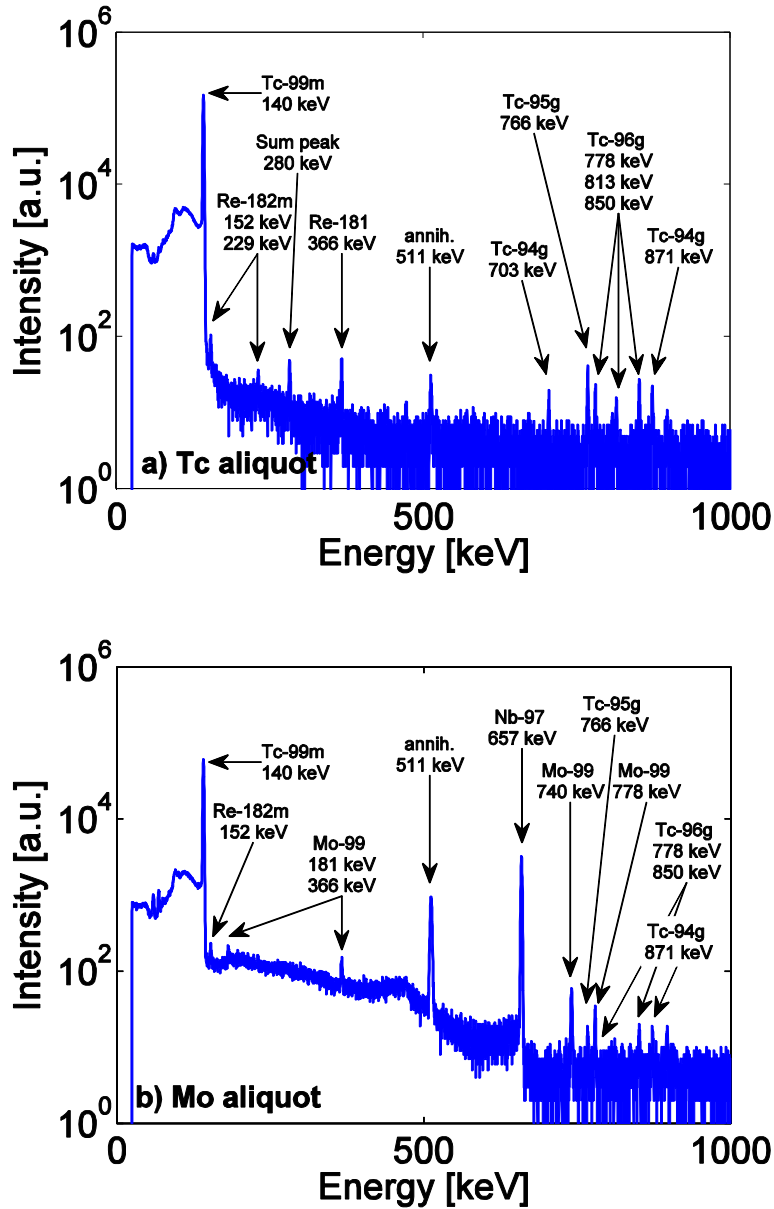


Figure 5-4. Sample γ -ray spectra to 1 MeV for (a) an aliquot of final extracted ^{99m}Tc obtained following irradiation of recycled ^{100}Mo , and (b) an aliquot of the ^{100}Mo collection vial. Samples were measured for 1 hr LT starting at 4.2 hr and 2.6 hr post-EOB, respectively.

5.3.4. ^{99m}Tc Radiochemical analysis

Table 5-5 summarizes the pH, radiochemical purity, and aluminum ion concentration measured for the extracted [^{99m}Tc]TcO₄⁻ in this study. As noted, all values are within the limits outlined by the United States Pharmacopeia (USP) pertechnetate monograph [20].

Table 5-5. [^{99m}Tc]TcO₄⁻ pH, radiochemical purity, and Al³⁺ concentration evaluated in this study following irradiation of both new and recycled ¹⁰⁰Mo.

	pH	TcO ₄ ⁻ [%]	Al ³⁺ [μg/mL]
New (No. = 4)	5.0–7.0	> 99	< 2.5
Recycled (No. = 3)	6.0–6.5	> 99	< 2.5
USP Monograph	4.5–7.5	> 95	< 10

Comparison of MDP labelling using ^{99m}Tc from a generator to ^{99m}Tc produced from irradiation of recycled ¹⁰⁰Mo metal showed similar chromatography results with < 1% colloid for both generator-Tc and cyclotron-Tc. Free pertechnetate was < 1% for generator-Tc, and < 3% for cyclotron-Tc. Using the imaging parameters described above, Figure 5-5 shows MDP images obtained with the two methods of ^{99m}Tc production. Images are displayed using the default window/levelling settings of the upper and lower limits set to the maximum and minimum pixels intensities, respectively, for each image. Qualitatively, there is no significant difference in the biodistribution of the two radiopharmaceuticals.

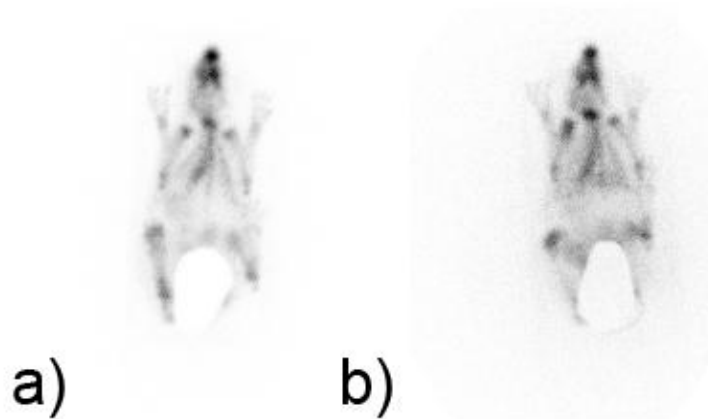


Figure 5-5. 40 MBq [^{99m}Tc]MDP uptake 2 hr post-injection for: (a) ^{99m}Tc from a generator, and (b) ^{99m}Tc obtained from cyclotron irradiation of recycled ^{100}Mo . The same rabbit was used for both images and imaged 6 days apart.

5.4. Discussion

This study presents a process for ^{99m}Tc extraction from a dissolved ^{100}Mo metal target, purification of the resulting ammonium molybdate, and hydrogen reduction back to metallic molybdenum. While metal to metal recovery yields of 87% are reported, we expect improvement by working with several grams of material. Furthermore, since visual inspection of the irradiated targets occasionally revealed region(s) void of ^{100}Mo due to small amounts of ^{100}Mo sloughing off into the helium cooling section of the target, we also expect improved recovery by implementing sintered targets as opposed to pressed metal powder. As noted above, the use of sintered targets is a parallel project currently under development at the University of Alberta. Irradiations at higher currents, higher energies, and longer irradiation times will however lead to increased accumulation of $A \neq 100$ stable molybdenum isotopes. As such, upon development of these higher-power targets, it will be necessary to re-assess potential changes in the radionuclidic purity and/or isotopic molybdenum

composition upon recycling and compare these results with the 12 MeV, 20–30 μA , 60–80 minute irradiations performed in this study.

The ^{100}Mo prepared in this study has been evaluated by ICP-MS, and no difference in the measured isotopic composition of new vs. recycled ^{100}Mo was found. The [$^{99\text{m}}\text{Tc}$]pertechnetate obtained following irradiation of both new and recycled ^{100}Mo had values for the pH, radiochemical purity, and Al^{3+} concentration that were in accord with USP recommendations. While radionuclidic purity evaluation revealed no differences in the $^{94\text{g}}\text{Tc}$, $^{95\text{g}}\text{Tc}$, and $^{96\text{g}}\text{Tc}$ impurities following irradiation of new or recycled ^{100}Mo , radionuclidic contaminants of ^{181}Re and $^{182\text{m}}\text{Re}$ were noted following irradiation of recycled ^{100}Mo . As these contaminants may yield increased dose and degrade image quality due to the high energy γ -rays of $^{182\text{m}}\text{Re}$, these contaminants will be mitigated in future experiments by using tantalum or quartz boats as opposed to tungsten. For this reason, as well as for the purpose of reducing larger quantities of the ammonium molybdate, we are currently investigating the use of a quartz rotary reactor tube furnace (e.g. Carbolite HTR) for future experiments.

5.5. Conclusion

The proposed methodology demonstrated that efficient recycling of enriched metallic ^{100}Mo targets is possible. This strategy is very desirable when considering production of large quantities of $^{99\text{m}}\text{Tc}$ on a routine basis. The proposed method has been evaluated and an overall metal to metal recovery of 87% was reported for this initial study. Recycled ^{100}Mo has been used to produce [$^{99\text{m}}\text{Tc}$]TcO₄⁻ that was comparable to generator derived $^{99\text{m}}\text{Tc}$. Although many of the recycling steps extended over several hours or days including, for example, hydrogen reduction or lyophilisation, respectively, each of these steps required minimal personnel time. Consequently, following setup optimization, the overall personnel time required for recycling a batch, or multiple pooled batches of ^{100}Mo , could likely be reduced to less than a few hours.

While the focus of this manuscript is on the cyclotron production of ^{99m}Tc , the proposed methodology may be applied to the cyclotron production of other medically relevant technetium isotopes such as the positron-emitting ^{94m}Tc . Furthermore, although we have implemented the ABEC separation scheme in these experiments, it should be possible to extend the proposed recycling methodology to other existing ^{99m}Tc extraction schemes.

This preliminary biodistribution data suggests that there is no significant difference in the biological handling of MDP when labelled by ^{99m}Tc produced by the two methods. Whilst quantitative analysis has not been performed, the equivalence of imaging parameters, counts, and biodistribution suggest that MDP labelled with cyclotron produced ^{99m}Tc using recycled enriched ^{100}Mo metal targets will offer a new route to the routine production of clinical radiopharmaceuticals in clinical nuclear medicine practice.

5.6. References

1. B. Scholten, R.M. Lambrecht, M. Cogneau, H.V. Ruiz, S.M. Qaim, Excitation functions for the cyclotron production of ^{99m}Tc and ^{99}Mo , *Appl. Radiat. Isot.* 51 (1999) 69–80.
2. F. Rösch, A.F. Novgorodov, S.M. Qaim, Thermo chromatographic separation of ^{94m}Tc from enriched molybdenum targets and its large scale production for nuclear medical applications, *Radiochim. Acta.* 64 (1994) 113–120.
3. B.T. Christian, R.J. Nickles, C.K. Stone, T.L. Mulnix, J. Clark, Improving the radionuclidic purity of ^{94m}Tc for PET imaging, *Appl. Radiat. Isot.* 46 (1995) 69–73.
4. H.M. Bigott, R. Laforest, X. Liu, A. Ruangma, F. Wuest, M.J. Welch, Advances in the production, processing and microPET image quality of technetium-94m, *Nucl. Med. Biol.* 33 (2006) 923–933.

5. N. Dallali, M. Ghanbari, Y. Yamini, B. Fateh, Y.K. Agrawal, Liquid-liquid extraction of ultra-trace amounts of technetium produced by $^{100}\text{Mo}(p,2n)^{99m}\text{Tc}$ nuclear reaction in cyclotron, *Indian J. Chem. A.* 46A (2007) 1615–1617.
6. S. Chattopadhyay, S.S. Das, M.K. Das, N.C. Goomer, Recovery of ^{99m}Tc from $\text{Na}_2[^{99}\text{Mo}]\text{MoO}_4$ solution obtained from reactor-produced $(n,\gamma)^{99}\text{Mo}$ using a tiny Dowex-1 column in tandem with a small alumina column, *Appl. Radiat. Isot.* 66 (2008) 1814–1817.
7. D.R. McAlister, E.P. Horwitz, Automated two column generator systems for medical radionuclides, *Appl. Radiat. Isot.* 67 (2009) 1985–1991.
8. R.D. Rogers, A.H. Bond, S.T. Griffin, E.P. Horwitz, New technologies for metal ion separations: Aqueous Biphasic Extraction Chromatography (ABEC). Part I Update of pertechnetate, *Solvent Extr. Ion Exc.* 14 (1996) 919–946.
9. R. Chakravarty A. Dash, M. Venkatesh, A novel electrochemical technique for the production of clinical grade ^{99m}Tc using $(n,\gamma)^{99}\text{Mo}$, *Nucl. Med. Biol.* 37 (2010) 21–28.
10. S.M. Tuominen, Preparation and sintering of fine molybdenum powder, *Powder Technology* 30 (1981) 73–76.
11. Aluminum alloy 6061 datasheet, Alcoa Engineered Products, Cressona, PA, http://www.alcoa.com/adip/catalog/pdf/Extruded_Alloy_6061.pdf (accessed 2011).

12. J.F. Ziegler, M.D. Ziegler, J.P. Biersack, The stopping and range of ions in matter (SRIM code, version 2008.04), <http://www.srim.org/> (accessed 2009).
13. National Nuclear Decay Center, Nuclear reaction and decay Q-values (QCalc), <http://www.nndc.bnl.gov/qcalc/> (accessed 2009).
14. L.J. Csányi, I. Horváth, Z.M. Galbács, Peroxide derivatives of molybdenum(VI) in neutral and alkaline media, *Transition Met. Chem.* 14 (1989) 90–94.
15. R.C. Weast, M.J. Astle, *CRC Handbook of Chemistry and Physics*, Boca Raton, Florida: CRC Press (1980) B72–B166.
16. C.K. Gupta, *Extractive Metallurgy of Molybdenum*, Boca Raton, Florida: CRC Press, (1992) 278-283, 317–319.
17. R. Selwyn, R. Nickles, B. Thomadsen, L. DeWerd, J.A. Micka, New internal pair production branching ratio of ^{90}Y : the development of a non-destructive assay for ^{90}Y and ^{90}Sr , *Appl. Radiat. Isot.* 65 (2007) 318–27.
18. National Nuclear Decay Center. Nuclear structure and decay Data (NuDat 2.5). <http://www.nndc.bnl.gov/nudat2/> (accessed 2011).
19. R.J. Barlow, *Statistics – A Guide to the Use of Statistical Methods in the Physical Sciences*, West Sussex, England: John Wiley & Sons Ltd (1989) 54.
20. U.S. Pharmacopeia. http://www.pharmacopeia.cn/v29240/usp29nf24s0_m80740.html (accessed 2011).

6. High-current metallic ^{100}Mo targets

A version of this chapter was presented at the 19th International Symposium of Radiopharmaceuticals Sciences, Amsterdam, Aug 28th–Sept 2nd, 2011:

K. Gagnon, C. Holt, J.S. Wilson, D. Mitlin, S. McQuarrie, Target preparation and recycling of molybdenum for the cyclotron production of $^{99\text{m}}\text{Tc}$, J. Label. Compd. Radiopharm. 54 (2011) S54.

6.1. Introduction

While parallels are noted between the cyclotron production of $^{99\text{m}}\text{Tc}$ and the cyclotron production of $^{94\text{m}}\text{Tc}$, the $^{94\text{m}}\text{Tc}$ production targets are typically limited to currents on the order of 5 μA [1]. This is roughly two orders of magnitude shy of the 100–500 μA needed for large-scale cyclotron production of $^{99\text{m}}\text{Tc}$. Unlike existing oxide-based target design strategies used for $^{94\text{m}}\text{Tc}$ [2, 3, 4, 5], this work focused on construction of targets using metallic enriched ^{100}Mo .

Enriched ^{100}Mo metal is commercially available and is supplied or may be recycled [6], as a powder. Formation of the enriched ^{100}Mo powder into a solid structure with minimal porosity is necessary in order to tolerate the high-power irradiations and maintain adequate structural stability. Although it is possible to press the powder as a means for target preparation, our initial tests revealed that there are concerns both with the thermal performance of such targets as well as the structural stability of these targets during post-irradiation transport.

The following factors were considered when evaluating metallic target design strategies:

- (i) The ability to achieve the desired target thickness – a factor which will depend on irradiation energy and target angle.

- (ii) The ability to deposit, or adhere, the molybdenum onto a backing plate. From our initial studies on directly cooled self-supported ^{nat}Mo foil, the water cooling was found to oxidize the molybdenum and thus directly cooled self-supported targets could not be used.
- (iii) The loss of expensive enriched material during target preparation.
- (iv) The ease of target construction and/or ability to produce many targets at once for scale-up purposes.

Enriched metallic molybdenum target preparation strategies, including electroplating [7] and rolling [8, 9, 10] have been discussed previously in the literature. While electroplating eliminates the additional step of reducing the ammonium molybdate to molybdenum metal at elevated temperatures under hydrogen atmosphere, the thicknesses achieved via electroplating have been limited to $\sim 30\ \mu\text{m}$ [7]. In contrast, rolled targets have been successfully prepared and irradiated, however material losses and lengthy preparation strategies are noted for this strategy [8, 9]. Metallic target preparation via thermal-spray coating of ^{nat}Mo in the context of cyclotron production of $^{99\text{m}}\text{Tc}$ has also been described in the literature [11]. Such targets have been successfully irradiated to $160\ \mu\text{A}$ at 25 MeV, however material losses were not reported for the thermal-spray coating method, and efficient deposition of enriched ^{100}Mo has yet to be demonstrated with this technique.

In this study, we present and evaluate a strategy for target preparation via sintering of ^{100}Mo metal. We achieved this by heating pressed molybdenum powder to $1600\ ^\circ\text{C}$ under a reducing atmosphere which led to the densification of the molybdenum powder into a solid structure. The formation of sintered molybdenum pellets occurred well below the $2623\ ^\circ\text{C}$ melting point of molybdenum. The produced pellets were each bonded to an aluminum target support plate by applying heat and pressure to the pellet under vacuum. Following initial optimization studies with ^{nat}Mo , three targets of enriched ^{100}Mo were prepared. Irradiation to beam powers in excess of 1 kW followed by the

successful extraction Curie quantities of [^{99m}Tc]TcO $_4^-$ has been achieved with these targets.

6.2. Materials and methods

6.2.1. Sintering overview

Due to the high cost of ^{100}Mo , preliminary sintering studies were performed using either commercially available metallic $^{\text{nat}}\text{Mo}$ (Aldrich, $\geq 99.9\%$ metal basis, 1–2 μm), or metallic molybdenum obtained from hydrogen reduction of [$^{\text{nat}}\text{Mo}$]ammonium molybdate as described in [6]. The enriched targets were prepared from commercially purchased metallic ^{100}Mo (Trace Sciences International) with the following isotopic composition: 97.39% ^{100}Mo , 2.58% ^{98}Mo , 0.01% ^{97}Mo , 0.005% ^{96}Mo , 0.005% ^{95}Mo , 0.005% ^{94}Mo , and 0.005% ^{92}Mo .

Using 300–350 mg of molybdenum metal powder, the powder was placed into a tantalum plate having a 1 mm deep elliptical well with semi-axes of 5 mm x 10 mm and hydraulically pressed using a hardened steel die. This molybdenum/tantalum assembly was placed into a Carbolite TZF 16/610 furnace and heated using the temperature control parameters shown in Table 6-1 under Grade 5.0 UHP hydrogen atmosphere at nominal flow rates of 750–1000 sccm. A flow rate of 750 sccm was used for the final enriched ^{100}Mo . While steps 2 and 4 of Table 6-1 were not essential for sintering, in accord with the reduction studies presented in Chapter 5, these two steps were added in an attempt to reduce any oxides prior to sintering. No additional characterization studies were however performed to evaluate the oxygen content of the molybdenum post sintering. The final product post sintering was an elliptical pellet of molybdenum which did not adhere to the tantalum support plate and was easily picked up and handled with tweezers.

Table 6-1. Programmed temperature profile used for sintering of molybdenum metal pellets.

Step	Temperature Range[°C]	Programmed Temperature Rate [°C/min]
1	25→600	5
2	600 (hold x 1hr)	0
3	600→1000	5
4	1000 (hold x 1hr)	0
5	1000→1600	5
6	1600 (hold x 3hr)	0
7	1600→25	-5

6.2.2. Sintering optimization

Previously reported strategies for sintering of molybdenum describe the use of binders including zinc stearate [12] and ethylene bis stearamide (EBS) [13]. We similarly attempted to sinter molybdenum using 2% zinc stearate by weight (Alfa Aesar) as well as 2% EBS by weight (Acrawax[®] C, Lonza, [powder and atomized]). Since no qualitative differences were noted between SEM images of the sintered pellets with/without binders, the use of binders was discontinued in this study.

One significant challenge that arose during our initial ^{nat}Mo studies was that the sintered pellets were notably bowed. This was problematic with regards to the subsequent required bonding step as flat molybdenum pellets are desired in order to maximize cooling. To prevent bowing, we devised a strategy whereby a 2 mm thick tantalum “cap” was placed atop the molybdenum during the sintering process. As noted in the schematic of Figure 6-1, the elliptical cap was a male cut-out to the existing 0.5 cm x 1.0 cm semi-axes tantalum well. This small amount of additional mass proved sufficient to eliminate any notable bowing of the

molybdenum pellet. This was a key development as maximal bonding between the molybdenum and aluminum is necessary to ensure optimum heat removal.

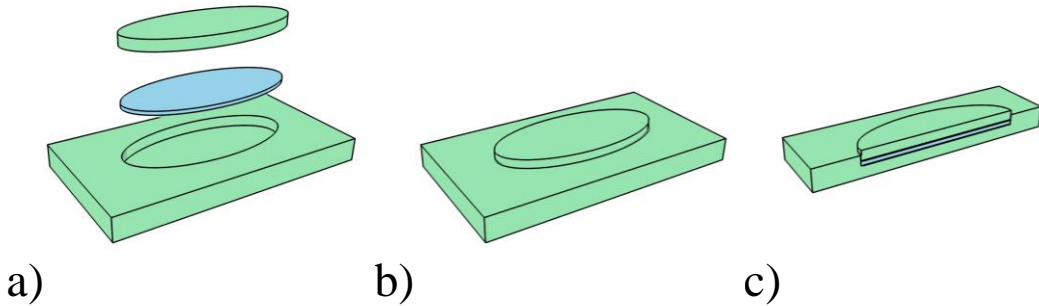


Figure 6-1. Schematic denoting (a) the assembly of the tantalum plate, molybdenum powder, and tantalum “cap”, (b) the complete plate system as inserted into the sintering oven, and (c) a cross-sectional cut-out through the plate system. Green = tantalum, blue = molybdenum.

6.2.3. Bonding

We were initially discouraged by the lack of post-sintering adherence of the molybdenum pellet to the tantalum support, but soon realized this to be of great benefit. Based on experimentally validated thermal modelling studies performed with COMSOL Multiphysics[®] (v. 3.5a) [14], we determined that tantalum is not ideal for use as a target support plate during cyclotron irradiation due to its poor thermal conductivity of $58 \text{ W m}^{-1} \text{ K}^{-1}$. Lack of adherence thus allowed the molybdenum pellet to be bonded to a material that is well-suited for irradiation, but would not have tolerated the high temperatures needed for sintering. For example, Al or Cu with thermal conductivities of $235 \text{ W m}^{-1} \text{ K}^{-1}$ and $400 \text{ W m}^{-1} \text{ K}^{-1}$, respectively, would be suitable for irradiation, but not for sintering.

In this study, target support plates were constructed of 6061 aluminum. Aluminum was selected as it is minimally activating, easily machined, inexpensive thus eliminating the need for plate re-use, and has a reasonable thermal conductivity. Furthermore, due to surface passivation, aluminum is chemically inert to the dissolution system we have implemented for ^{99m}Tc extraction which includes dissolution via hydrogen peroxide followed by basification with ammonium carbonate. In addition to an elliptical well that was identical in size to that of the tantalum plates, a groove was also machined into the aluminum plates to allow for an o-ring to be seated and seal the target plate to the helium cooling target assembly during irradiation. Prior to bonding with the molybdenum, the aluminum plates were cleaned by soaking overnight in a solution of ~50 mL of 29–32% w/w H_2O_2 (Alfa Aesar, ACS Grade) and ~150 mL of 70% HNO_3 (Sigma-Aldrich, ACS Grade).

The general scheme we developed for bonding molybdenum to aluminum requires the application of both heat and a compressive force under a vacuum atmosphere. When the molybdenum pellet was placed into the well of the aluminum target plate, it sits below the top surface of the plate. Pressure was applied to the pellet by placing one of the tantalum “caps” described above on top of the molybdenum so that the molybdenum was sandwiched between the tantalum cap and the aluminum target support plate. This sandwiched molybdenum assembly was subsequently loaded into the ELAN CB6L (SUSS MicroTec) wafer bonding system located at the University of Alberta’s Micro and Nanofabrication facility (NanoFab, Edmonton, AB).

Bonding of molybdenum onto aluminum was achieved by evacuating the chamber to 5×10^{-4} Torr, applying a compression force of 1500 N to this sandwich configuration, and heating both the top and bottom heating elements to 400 °C for one hour. To avoid oxidation of the molybdenum, heating elements were allowed to cool to 300 °C prior to venting of the chamber and releasing the applied force. A typical temperature/chamber vacuum/compression cycle is given in Figure 6-2.

While elevated temperature and pressure conditions were attempted using the maximum system parameters of 500 °C and 8800 N, such attempts proved disastrous as the aluminum target plate bonded directly onto the lower heating element of the bonding system. Consequently, all further bonding studies were performed with an extra 3 mm protective steel plate in place between the bonding system and the aluminum plate.

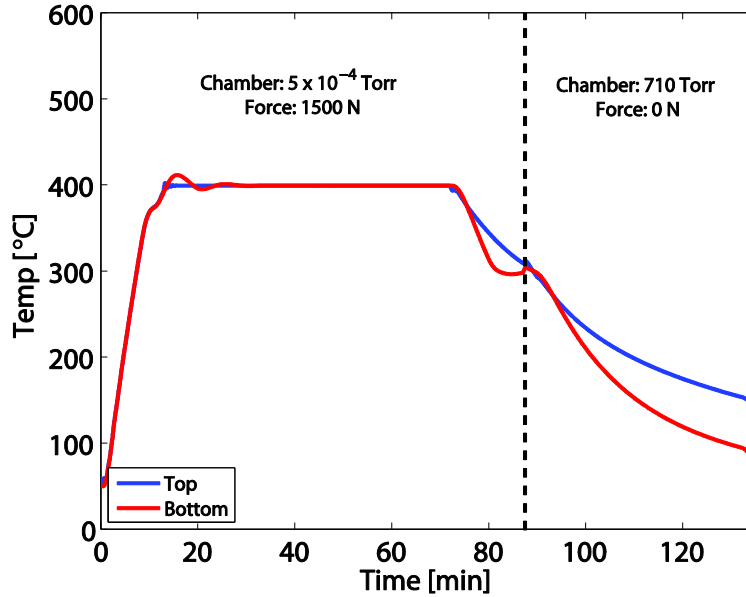


Figure 6-2. A sample measured temperature profile of both the top and bottom heating elements of the SUSS wafer bonding system.

A total of three ^{nat}Mo and three ¹⁰⁰Mo targets were bonded as described above. Adherence and structural stability were verified by dropping the three ^{nat}Mo targets onto the ground from a height of approximately 1.5 m. Two of the three pellets remained adhered to the aluminum; the reason for separation in the third target is unknown. One of the two remaining ^{nat}Mo bonded pellets was further tested by placing it on a hot-plate pre-set to 550 °C for approximately 90 s, upon which it was then immediately removed, immersed in liquid nitrogen, and once again dropped from a height of approximately 1.5 m. Aside from evidence of

oxidation on the surface of the molybdenum due to being heated in air, the target remained intact. The ^{100}Mo targets were not dropped prior to irradiation.

6.2.4. Irradiation

Test irradiations were performed on the two sintered and bonded $^{\text{nat}}\text{Mo}$ targets and the three sintered and bonded ^{100}Mo targets. All targets were oriented at 30 degrees to the beam and irradiations were performed on the variable energy TR-19/9 Cyclotron (Advanced Cyclotron Systems Inc., Richmond, ACSI, BC), at the Edmonton PET Centre (Edmonton, AB). A summary of the irradiation conditions is given in Table 6-2.

As illustrated in Figure 6-3, the target plate is not electrically isolated from the helium cooling portion of the target. Consequently, the measured beam current does not correspond to the amount of beam incident on the molybdenum target, but rather the amount of beam incident on both the molybdenum target and the helium cooling portion of the target. Poor beam alignment and/or large beam divergence will therefore result in the incorrect reporting of beam current incident on the molybdenum. For the purpose of ensuring maximum registered beam on the molybdenum, a thermocouple was affixed to the helium cooling section of the target as indicated in Figure 6-4 and the temperature was monitored real-time throughout each irradiation. The temperature was used as a surrogate indicator of beam alignment, where lower temperatures presumably represented improved beam alignment and a more accurate readout of the current “on-target”. During irradiation we therefore aimed for a beam tuning which would minimize the temperature of the helium assembly. Since we had previously noted melting of the helium cooling lines when the thermocouple temperature exceeded 100 °C, while tuning the beam to achieve the desired operating current, temperatures were maintained below approximately 80 °C. This optimization sometimes took upwards of an hour. It is largely for this reason that the operating currents of Table 6-2 differ significantly from the average current, where the average current was calculated by dividing the total integrated current by the irradiation time.

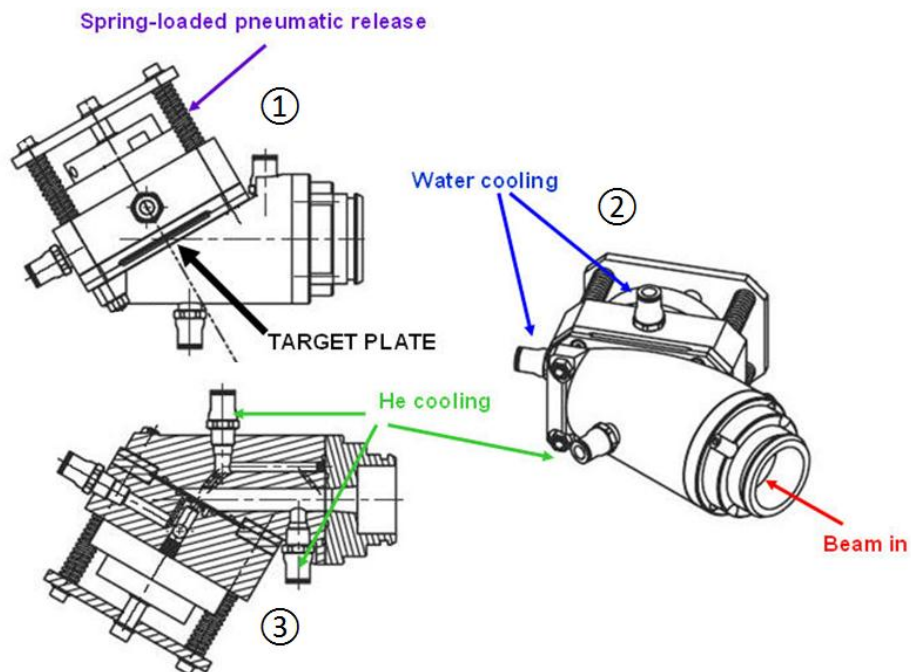


Figure 6-3. Three views of the 30 degree ACSI solid target system showing both the water and helium cooling sections of the target (schematics courtesy of ACSI).

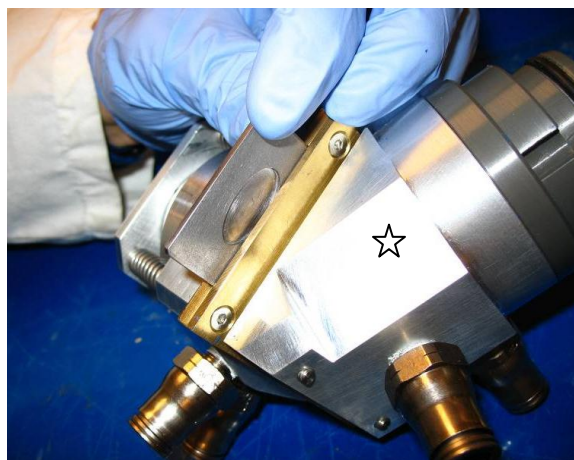


Figure 6-4. Picture of the target system used for irradiation of the ^{100}Mo targets developed in this work. The target plate shown in this photo does not contain any ^{100}Mo or o-ring. The approximate location where the thermocouple was affixed to the helium cooling assembly has been indicated by a star.

Table 6-2. Irradiation conditions for the ^{nat}Mo and ^{100}Mo targets prepared in this study.

Sample	Material	Mo Target Mass [mg]	Energy [MeV]	Operating Current [μA]	Integrated Current [$\mu\text{A min}$]	Average Current [μA]	Irradiation Length [min]
1	^{nat}Mo	~350	17.5	95	972	49	20
2	^{nat}Mo	~350	17.5	80	1500	71	21
3	^{100}Mo	~300	18.0	80	25551	71	360
4	^{100}Mo	~300	18.0	80	25002	69	360
5	^{100}Mo	~300	18.0	45	14750	41	360

Following irradiation, the ^{nat}Mo targets were allowed to decay for an extended period of time prior to visual inspection. In contrast, the ^{100}Mo targets were removed approximately 30–45 minutes post-EOB by remotely dropping the target into a lead container using the pneumatic release mechanism noted in Figure 6-3. The distance dropped was approximately 10 cm and all targets remained intact during this process. The shielded container was transferred to a hot-cell and the targets were processed immediately to extract the $[\text{}^{99m}\text{Tc}]\text{TcO}_4^-$.

6.2.5. Target dissolution and ^{99m}Tc extraction

The irradiated ^{100}Mo and aluminum support plate were placed in a beaker on a hot-plate set at 60 °C. Through use of remote manipulators, the molybdenum was dissolved by step-wise addition of ~10 mL of 29–32% w/w H_2O_2 (Alfa Aesar, ACS Grade) and then basified by addition of 2 mL of 3 M $(\text{NH}_4)_2\text{CO}_3$. This basified solution was transferred into a sealed 20 mL vial, and the dissolution beaker was further rinsed with 8 mL of 3 M $(\text{NH}_4)_2\text{CO}_3$ and added to the sealed vial. Prior to further processing, the vial activity was assayed using a CRC-15PET dose calibrator with a ^{99m}Tc calibration setting of #079. Standard borosilicate glassware was employed in this study.

The dissolved target solution was purified using an automated Bioscan Reform Plus module which we have modified for extraction of $[^{99m}\text{Tc}]\text{TcO}_4^-$ using ABECTM resin [15, 16]. With this module, the dissolved solution was passed through a column of 500 mg of 100–200 mesh ABEC-2000 resin (Eichrom) and the pertechnetate was retained. The molybdate eluate was collected for future recycling. The column was then washed with 1 mL of 3 M ammonium carbonate solution to remove residual molybdate, followed by 3 mL of 1 M sodium carbonate solution. The high salt concentrations were necessary to prevent elution of the pertechnetate. The ABEC column was washed with 10 mL of sterile water to remove the pertechnetate and the resulting solution was passed through a strong cation exchange column (All-Tech) to reduce the pH to acceptable levels. Both ammonium carbonate (Alfa Aesar, ACS Grade) and sodium carbonate (Fisher Scientific, ACS Grade) solutions were freshly prepared using sterile water prior to the separation. Conditioning of the columns involved washing the ABEC with 20 mL of 3 M ammonium carbonate, and the SCX with 10 mL of sterile water.

The activity of the eluted $[^{99m}\text{Tc}]\text{TcO}_4^-$ was assayed with a dose calibrator. The $[^{99m}\text{Tc}]\text{TcO}_4^-$ was then evaluated for Al^{3+} concentration using the aurintricarboxylic acid spot test, pH using a colorimetric spot test, radionuclidic purity via γ -ray spectroscopy, and radiochemical purity via ITLC. A fraction of the collected $[^{99m}\text{Tc}]\text{TcO}_4^-$ was also used to label MDP in which the stability was evaluated by ITLC.

6.3. Results and discussion

6.3.1. Sintering

Sintered pellets of molybdenum were successfully prepared by the heating of pressed molybdenum in a tantalum support plate under hydrogen atmosphere to temperatures of 1600 °C. Figure 6-5 gives a comparison of a pressed ^{nat}Mo target versus a pressed and sintered ^{nat}Mo target. Both samples were prepared using metallic molybdenum obtained following hydrogen reduction of [^{nat}Mo]ammonium molybdate. In this figure, excellent contact is noted between

the molybdenum powder grains in the sintered sample. To ensure that sintering occurred throughout the pellet, not just the surface, a sintered pellet was broken in two and an SEM image obtained edge-on as shown in Figure 6-6. In this study, pellet densities of up to 93% were observed, and mass losses following sintering were typically less than 2%. Due to an increase in density, the sintered elliptical molybdenum pellets were smaller than the tantalum well. The ^{100}Mo pellets of these experiments occupied approximately 67% of the total surface area of the initial ellipse area.

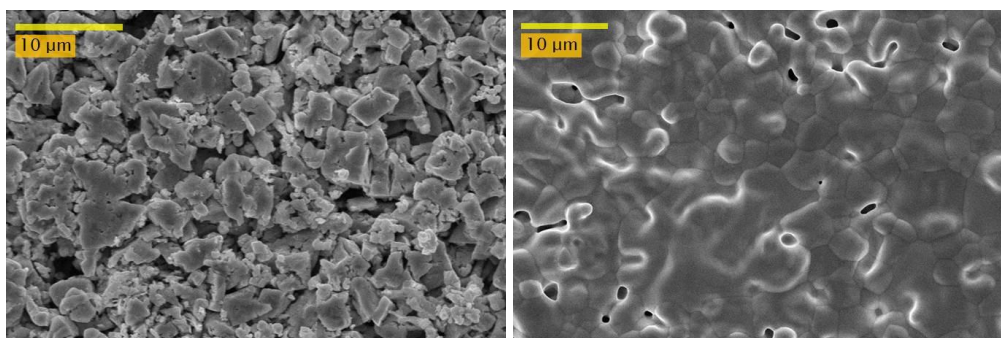


Figure 6-5. SEM image of pressed $^{\text{nat}}\text{Mo}$ (left) versus pressed and sintered $^{\text{nat}}\text{Mo}$ (right).

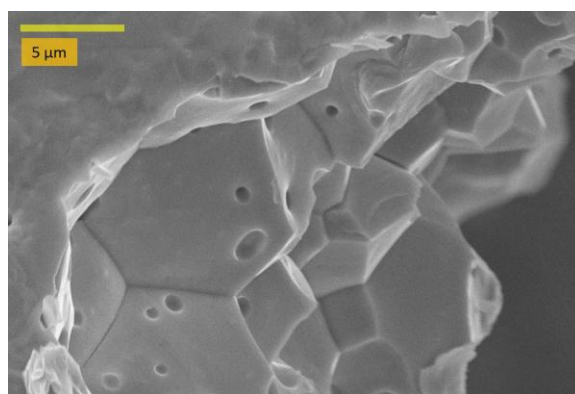


Figure 6-6. An edge-on SEM view of a sintered $^{\text{nat}}\text{Mo}$ pellet broken in two.

As a refractory metal, tantalum was selected as the molybdenum support during the sintering process as it has a high melting point and its surface is

chemically inert due to passivation. While other metals could have been selected for this application, from our experience, we advise against the use of tungsten at any point during the target preparation since proton activation of trace contaminants of tungsten will yield rhenium. The chemical similarities between contaminant rhenium and technetium will add an additional level of complexity with regards to final ^{99m}Tc purification.

During optimization studies, the use of binders was not found to reveal qualitative surface differences when compared with sintered pellets prepared without the use of binders. We did however develop a strategy to rectify the bowing of sintered pellets by addition of a tantalum “cap” during the sintering process. While pellet production may benefit from further optimization of the sintering time [13, 17], temperature [18], use of moist hydrogen [19], use of vacuum [13 18], etc., the parameters outlined in this study proved adequate. The developed process also required minimal user processing time as the Mo/Ta assemblies were loaded into an oven at the end of the day and retrieved the following morning. Furthermore, using this setup, we simultaneously produced as many as seven sintered pellets at once – a feat which is of great benefit when considering potential scale-up for the large-scale cyclotron-production of ^{99m}Tc .

6.3.2 Bonding

We have presented a strategy for bonding of the sintered molybdenum pellets onto an aluminum target support plate. Enriched ^{100}Mo targets prepared by the proposed strategy were found to maintain structural stability following irradiation. While pellets were bonded to the aluminum target plate one-by-one, for the purpose of scale-up we foresee that it should be possible to adapt the setup to allow for simultaneous bonding of many targets at once.

6.3.3. Irradiation

Two $^{\text{nat}}\text{Mo}$ and three enriched ^{100}Mo targets were irradiated following preparation with this proposed sintering and bonding strategy. Figure 6-7 gives pictures of Sample #2 from Table 6-2 both pre- and post-irradiation at 80 μA and

17.5 MeV. Evidence of oxidation resulting from irradiation can be seen on the surface of the molybdenum, however with $m_{\text{initial}} = 4.6417$ g and $m_{\text{final}} = 4.6418$ g, no mass loss was observed for this target following irradiation.

Following irradiation of the ^{100}Mo targets, $[\text{}^{99\text{m}}\text{Tc}]\text{TcO}_4^-$ was extracted using a Bioscan Reform Plus module which we have adapted to accommodate a column loaded with approximately 0.5 g of ABEC resin. With non-decay-corrected production yields of 60.5, 51.9, and 44.7 GBq for targets 3 through 5, respectively, consistent recovery of more than a Curie of $^{99\text{m}}\text{Tc}$ is reported. Typical extraction times were approximately 30 minutes for this system. The time between EOB and assaying of the final $^{99\text{m}}\text{Tc}$ activity varied from 101–136 minutes as the target was left to decay for approximately 30–45 minutes prior to removal. Chemical evaluation of the extracted $[\text{}^{99\text{m}}\text{Tc}]\text{TcO}_4^-$ showed that the Al^{3+} concentration, pH, and radiochemical purity were all within USP limits [20]. Radionuclidic purities in excess of 99.9% are reported at EOB when contributions from $^{94\text{g}}\text{Tc}$, $^{95\text{m}}\text{Tc}$, $^{95\text{g}}\text{Tc}$, $^{96\text{g}}\text{Tc}$, and $^{97\text{m}}\text{Tc}$ were evaluated. Radiochemical purity of the labelled MDP was found to be greater than 98% up to 24 hours post labelling.

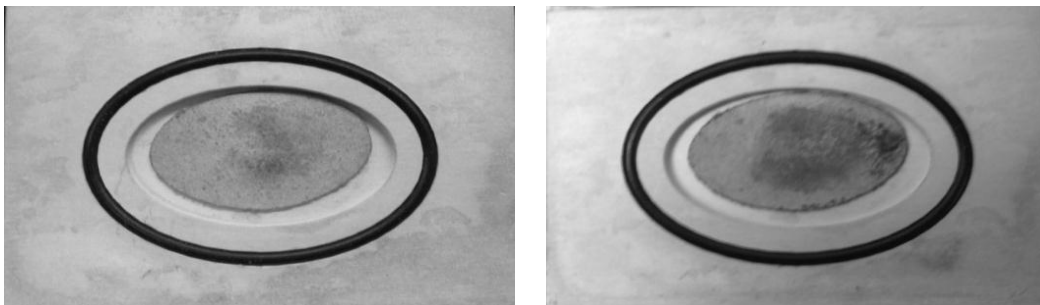


Figure 6-7. A $^{\text{nat}}\text{Mo}$ target pre (left)- and post (right)- irradiation.

While evaluation of the thick target yields of $^{99\text{m}}\text{Tc}$ was not the goal of this study, the decay-corrected $^{99\text{m}}\text{Tc}$ saturated yields were determined using both the pre-extraction and post-extraction activity assays. Despite 100% extraction efficiency, these numbers are not expected to be identical due to coproduction of

contaminant ^{96}Nb , ^{97}Nb , and ^{99}Mo which will contribute to the pre-extraction activity assay as these contaminants are not retained on the ABEC resin. Results have been compared with a theoretical saturated yield of $4.8 \text{ GBq}/\mu\text{A}$ calculated from the cross section fitting parameters presented by Gagnon et al. [21] using energy step sizes of 0.1 MeV , from $17.9 \rightarrow 8.0 \text{ MeV}$. The following factors are attributed to the discrepancies between the recovered and theoretical $^{99\text{m}}\text{Tc}$ yields listed in Table 6-3:

- (i) The need for further optimization of the chemical extraction system including, for example, the mass of resin, flow rates, etc.
- (ii) The need for developing a more compact and efficient dissolution system. At present, technetium is lost during the dissolution step as it is carried away with the evaporating peroxide/water vapours. Evidence of such loss is noted as there is immediate contamination on the surfaces outside of the dissolution beaker following dissolution.
- (iii) The need for creating oversized pellets to account for pellet size reduction due to density increase following sintering as seen in Figure 6-7. The ^{100}Mo pellets of these experiments occupied approximately 67% of the total area of the aluminum well. While the first two ^{100}Mo pellets were bonded near the centre of the aluminum well, the third ^{100}Mo was strategically bonded off-centre as there was indication using the Gafchromic beam monitoring strategy developed by Avila-Rodriguez, et al. [22] that the beam spot was off to one side.
- (iv) Loss of beam on the helium cooling assembly of the target system despite efforts to minimize this contribution by temperature monitoring.

Table 6-3. Percent of theoretical saturated yield based on assays performed prior to extraction, and post extraction.

Sample	Pre-extraction	Post-extraction
	Yield [%]	Yield [%]
3	57	46
4	54	38
5	66	55

While strategies for improving and optimizing the aforementioned points are currently under investigation, we nevertheless report the successful production of Curie quantities of high quality [^{99m}Tc]TcO₄⁻ using the sintered target strategy.

6.4. Conclusion

In this preliminary study, a strategy for preparing enriched ^{100}Mo metallic targets was demonstrated. This strategy entails the sintering of molybdenum in a hydrogen atmosphere, followed by bonding of the produced pellet onto an aluminum target support plate. Successful irradiation of these newly developed targets to beam powers in excess of 1 kW is reported. Targets have been found to maintain good structural stability post-irradiation which will facilitate remote or automated target recovery. Curie quantities of high radiochemical and radionuclidic purity [^{99m}Tc]TcO₄⁻ have been obtained following the irradiation of ^{100}Mo metallic targets, oxidative dissolution, and separation of the ^{99m}Tc from the ^{100}Mo with our modified automated synthesis module. Considering that previous ^{94m}Tc enriched molybdenum targetry systems were typically limited to irradiation currents on the order of 5 μA , the demonstrated strategy, which is amenable to the simultaneous preparation of numerous targets, is a significant advance with regards to achieving large-scale cyclotron production of ^{99m}Tc . Further optimization studies, as well as studies at higher irradiation energies and currents are in progress.

6.5. References

1. K. Gagnon, S. McQuarrie, D. Abrams, A.J.B. McEwan, F. Wuest, Radiotracers based on technetium-94m, *Current Radiopharmaceuticals* 4 (2011) 90–101.
2. H.M. Bigott, R. Laforest, X. Liu, A. Ruangma, F. Wuest, M.J. Welch, Advances in the production, processing and microPET image quality of technetium-94m, *Nucl. Med. Biol.* 33 (2006) 923–933.
3. B.E. Rogers, J.J. Parry, R. Andrews, P. Cordopatis, B.A. Nock, T. Maina, MicroPET imaging of gene transfer with Somatostatin receptor-based reporter gene and ^{94m}Tc -Demotate 1, *J. Nucl. Med.* 46 (2005) 1889–1897.
4. B.T. Christian, R.J. Nickles, C.K. Stone, T.L. Mulnix, J. Clark, Improving the radionuclidic purity of ^{94m}Tc for PET imaging, *Appl. Radiat. Isot.* 46 (1995) 69–73.
5. F. Rösch, A.F. Novgorodov, S.M. Qaim, Thermochemical separation of ^{94m}Tc from enriched molybdenum targets and its large scale production for nuclear medical applications, *Radiochim. Acta.* 64 (1994) 113–120.
6. K. Gagnon, C. Holt, J.S. Wilson, D. Mitlin, S. McQuarrie, Target preparation and recycling of molybdenum for the cyclotron production of ^{99m}Tc , *J. Label. Compd. Radiopharm.* 54 (2011) S54.
7. T. Morley, K. Gagnon, P. Schaffer, E. Asselin, S. Zeisler, S. McQuarrie, M. Kovacs, J. Wilson, F. Benard, T. Ruth, Cyclotron production of technetium radioisotopes, *J. Nucl. Med.* 52 (2011) S291.

8. N.Y. Kheswa, P. Papka, E.Z. Buthelezi, R.M. Lieder, R. Neveling, R.T. Newman, Manufacturing of calcium, lithium, and molybdenum targets for use in nuclear physics experiments, *Nucl. Instrum. Meth. A.* 613 (2010) 389–391.
9. A.R. Lipski, L.L. Lee Jr., J.F. Liang, J.C. Mahon, Preparation of isotopic molybdenum foils utilizing small quantities of material, *Nucl. Instrum. Meth. A.* 334 (1993) 126–127.
10. F.J. Karasek, Fabrication of target foils by rolling techniques, *Nucl. Instrum. Meth.* 102 (1972) 457–458.
11. H. Targholizadeh, G. Raisali, A.R. Jalilian, N. Rostampour, M. Ensaf, and M.K. Dehghan, Cyclotron production of technetium radionuclides using a natural metallic molybdenum thick target and consequent preparation of [Tc]-BRIDA as a radio-labelled kit sample, *Nukleonika*, 55 (2010) 113–118.
12. V.V. Sukhozhak, V.V. Panichkina, V.V. Skorokhod, Theory and technology of sintering, thermal, and chemicothermal treatment processes – Pressing and sintering of fine molybdenum powder, Translated from *Poroshkovaya Metallurgiya*, 128 (1973) 20–22.
13. H.S. Huang, K.S. Hwang, Deoxidation of molybdenum during vacuum sintering, *Metall. Mater. Trans. A.* 33 (2002) 657–664.
14. K. Gagnon, J.S. Wilson, and S.A. McQuarrie, Thermal modelling of a solid cyclotron target using finite element analysis: An experimental validation, *Proceedings of the 13th International Workshop on Targetry and Target Chemistry*, Roskilde, Denmark, July 26–28 (2010) O11.

15. D.R. McAlister, E.P. Horwitz, Automated two column generator systems for medical radionuclides. *Appl. Radiat. Isot.* 67 (2009) 1985–1991.
16. R.D. Rogers, A.H. Bond, S.T. Griffin, E.P. Horwitz, New technologies for metal ion separations: Aqueous Biphasic Extraction Chromatography (ABEC). Part I Update of pertechnetate, *Solvent Extr. Ion Exc.* 14 (1996) 919–946.
17. S.M. Tuominen, Preparation and sintering of fine molybdenum powder, *Powder Technol.* 30 (1981) 73–76.
18. V.I. Torbov, V.N. Troitskii, T.V. Rezhikova, A.Z. Rakhmatullina, A.P. Zuev, V.N. Doronin, Theory and technology of sintering, thermal, and chemicothermal treatment processes – Sintering of very fine molybdenum and tungsten powders, Translated from *Poroshkovaya Metallurgiya*, 229 (1981) 47–51.
19. E.P. Ignashev, A.U. Kharin, Sintering of molybdenum pressing in moist hydrogen and their rolling into strip, Translated from *Poroshkovaya Metallurgiya*, 15 (1963) 99–103.
20. U.S. Pharmacopeia.
http://www.pharmacopeia.cn/v29240/usp29nf24s0_m80740.html
(accessed 2011).
21. K. Gagnon, F. Bénard, M. Kovacs, T.J. Ruth, P. Schaffer, J.S. Wilson, S.A. McQuarrie, Cyclotron production of ^{99m}Tc : Experimental measurement of the $^{100}\text{Mo}(p,x)^{99}\text{Mo}$, ^{99m}Tc and ^{99g}Tc excitation functions from 8 to 18 MeV, *Nucl. Med. Biol.* 38 (2011) 907–916.

22. M.A. Avila-Rodriguez, J.S. Wilson, S.A. McQuarrie, The use of radiochromic films to measure and analyze the beam profile of charged particle accelerators, *Appl. Radiat. Isot.* 67 (2009) 2025–2028.

7. Quality control of cyclotron produced ^{99m}Tc

A version of this chapter was presented at the Annual Congress of the European Association of Nuclear Medicine, Birmingham, UK, October 15–19, 2011.

K. Gagnon, D. Abrams, J.S. Wilson, S.A. McQuarrie, A.J.B. McEwan, Quality control of cyclotron vs. generator ^{99m}Tc -labeled radiopharmaceuticals, *Eur. J. Nucl. Med. Mol. Imaging.* 38 (2011), S105.

7.1. Introduction

The quality of cyclotron-based $[\text{}^{99m}\text{Tc}]\text{TcO}_4^-$ as compared with the long-standing accepted quality of the existing reactor-based $^{99}\text{Mo} \rightarrow ^{99m}\text{Tc}$ generator strategy is a fundamental consideration for the large scale cyclotron ^{99m}Tc production.

As a starting point for evaluating the quality of the extracted cyclotron-produced $[\text{}^{99m}\text{Tc}]\text{TcO}_4^-$ product, we refer to the United States Pharmacopeia (USP) pertechnetate monograph [1]. This monograph outlines limits for radionuclide identification, bacterial endotoxin content, pH, radiochemical purity, radionuclidic purity, and chemical purity with specific evaluation of aluminum and methyl ethyl ketone noted where applicable. It must be noted, however, that the USP monograph is specific to $[\text{}^{99m}\text{Tc}]\text{TcO}_4^-$ obtained following the decay of the parent ^{99}Mo which is, in turn, produced either via neutron bombardment of ^{98}Mo , or as a product of uranium fission. In fact, with regards to radionuclidic purity, different USP specifications are reported, depending on which of these two ^{99}Mo production methods is employed. Thus, when extending the USP specifications to the direct cyclotron production of ^{99m}Tc , guidelines for radionuclidic purity as well as chemical purity, a factor which is based on the various separation strategies, must be re-evaluated.

In addition to the above noted USP specifications, it has been suggested that the coproduction of contaminant ^{99g}Tc may be a limiting factor in the cyclotron production of ^{99m}Tc [2]. We have however previously demonstrated that for typical irradiation conditions, this contaminant is expected to be on par with the level of ^{99g}Tc contaminant observed in a generator eluted at a 24 hr frequency [3]. The extracted $[\text{}^{99m}\text{Tc}]\text{TcO}_4^-$ may be further assessed by evaluating its labelling efficiency, stability of the labelled product, and biodistribution of ^{99m}Tc -labelled radiopharmaceuticals.

This Chapter provides a summary of the acquired quality data for all $[\text{}^{99m}\text{Tc}]\text{TcO}_4^-$ produced up to September 2011 following the irradiation of powdered or sintered ^{100}Mo targets at the Edmonton PET Centre (EPC). Where relevant, comparisons are made with USP specifications. Quality data for the labelling efficiency of ^{99m}Tc -labelled MDP and disofenin, as well as biodistribution studies with $[\text{}^{99m}\text{Tc}]\text{TcO}_4^-$ and $[\text{}^{99m}\text{Tc}]\text{disofenin}$ are also described and compared with generator-based ^{99m}Tc .

7.2. Materials and methods

Experiments are divided into two categories: targets which have been processed using the manual separation methodology described in Chapter 5, and targets which have been processed using the automated Bioscan Reform-Plus extraction system described in Chapter 6. All targets processed via the manual separation scheme have employed “Batch 1” of ^{100}Mo , while all those separated with the automated scheme used “Batch 2”. The isotopic compositions of these two batches are given in Table 7-1.

The total of all non-foil, or non-Chapter 3, ^{100}Mo irradiation/ ^{99m}Tc extraction experiments performed up to September 2011 at the EPC are reported chronologically in Table 7-2. This table includes experiments from Chapter 5 and 6, as well as one additional manual extraction experiment performed at 18 MeV, and two further non-sintered automated extraction experiments. The sample

names in Table 7-2 are denoted by the use of ME or AE to indicate manual or automated extraction, and N or R to indicate the use of new or recycled ^{100}Mo .

Table 7-1. The two ^{100}Mo batches used for $^{99\text{m}}\text{Tc}$ production at the EPC.

	Batch 1 [%]	Batch 2 [%]
^{100}Mo [%]	99.27	97.39
^{98}Mo [%]	0.47	2.58
^{97}Mo [%]	0.08	0.01
^{96}Mo [%]	0.05	0.005
^{95}Mo [%]	0.04	0.005
^{94}Mo [%]	0.03	0.005
^{92}Mo [%]	0.06	0.005

The tests used to evaluate $[^{99\text{m}}\text{Tc}]\text{TcO}_4^-$ quality have evolved throughout these studies in consideration of the future goal of preparing $^{99\text{m}}\text{Tc}$ for human use. It is for this reason that additional QC data is presented for the latter lots of Table 7-2. The different categories of tests performed are as follows:

- (i) USP specifications
- (ii) Additional chemical purity testing
- (iii) Stability of $[^{99\text{m}}\text{Tc}]\text{TcO}_4^-$ and labelling of other $^{99\text{m}}\text{Tc}$ -pharmaceuticals
- (iv) Biodistribution studies

Table 7-2. A chronological summary of all thick target experiments performed with enriched ^{100}Mo up to September 2011.

Lot	^{100}Mo Batch	E_p [MeV]	Target Preparation	Irradiation Time [min]	Integrated Current [$\mu\text{A min}$]	Additional Studies
ME-N1	1	12.1→6.5	Pressed	80	1500	MDP Labelling
ME-N2	1	12.1→6.5	Pressed	79	1500	MDP Labelling
ME-N3	1	12.1→6.5	Pressed	72	2000	Disofenin Biodistribution (Rabbit imaging)
ME-N4	1	12.1→6.5	Pressed	80	1500	Disofenin Biodistribution (Mouse dissection)
ME-N5 ^a	1	18.1→10.4	Pressed	360	7112	MDP Labelling
ME-R1	1	12.1→6.5	Pressed	80	1500	MDP Labelling
ME-R2	1	12.1→6.5	Pressed	60	1642	MDP Biodistribution (Rabbit imaging)
ME-R3	1	12.1→6.5	Pressed	80	1901	MDP Biodistribution (Rabbit imaging)
AE-N1	2	17.9→5.5	Sintered	360	25551	MDP Labelling/Stability
AE-N2	2	17.9→5.5	Sintered	360	25002	MDP Labelling/Stability
AE-N3	2	17.9→5.5	Sintered	360	14750	MDP Labelling/Stability
AE-N4 ^b	2	17.4→14.5	Pressed	60	1150	TcO_4^- Biodistribution (Mouse dissection)
AE-N5 ^b	2	16.8→14.0	Pressed	75	1650	TcO_4^- Biodistribution (Rabbit imaging)

^aUses manual extraction (ME) methodology of Chapter 5, but sample is not discussed within chapter

^bUses automated extraction (AE) methodology of Chapter 6, but sample is not discussed within chapter

7.2.1. USP specifications

The sodium pertechnetate USP specifications [1] are routinely evaluated for [^{99m}Tc]TcO $_4^-$ eluted from $^{99}\text{Mo}/^{99m}\text{Tc}$ generators at the Edmonton Radiopharmaceutical Centre (ERC). ERC is a centralized radiopharmacy whose mandate is the manufacture and supply of radiopharmaceuticals to regional hospitals in the Capital Health Region. The testing procedures in this study follow guidelines of ERC and were adopted from their clinical standard operating procedures. USP specifications on sterility [4] and osmolality [5] were also evaluated though not specific to [^{99m}Tc]TcO $_4^-$, in order to evaluate the feasibility of using the recovered activity for injection.

7.2.1.1. Radionuclide identification

Radionuclide identity of ^{99m}Tc was determined by measurement of the half-life in a dose calibrator and/or by identification of the 140 keV photopeak following sample assay on a HPGe detector. Further details on γ -ray spectroscopy are given in Section 7.2.1.5. The half-life was evaluated by two repeated assay measurements in a dose calibrator on the same day as the ^{99m}Tc production. These measurements were typically performed 2–3 hours apart and within a few hours post-EOB. An additional assay was also performed the day following extraction so as to allow for an overnight half-life evaluation.

7.2.1.2. Bacterial endotoxin

The bacterial endotoxin content of samples was determined at ERC using the Charles River Endosafe-PTS USP compatible system methodology. A 25 μL sample, or dilutions thereof, was placed on the Endosafe-PTS system cartridge in quadruplicate and processed by the system followed by result printout.

7.2.1.3. pH

One drop from the product sample vial was applied to each section of commercially available narrow range, either 0–6 or 5–10, pH paper (EMD

Chemicals). The colours of the wetted areas were immediately compared to the reference colour indicator chart supplied with each lot of pH paper.

7.2.1.4. Radiochemical purity

Radiochemical purity (RCP) was evaluated by ITLC. Namely, 1–2 drops of [^{99m}Tc] TcO_4^- were dispensed from a 25G needle at the origin of a pre-marked commercially available, 1 x 7 cm silica gel coated strip (ITLC-SG). Initial studies were performed with 0.9% NaCl or acetone as the mobile phase, while later studies employed n-butanol. Upon assaying of the strip with a Bioscan AR-2000 radio-TLC scanner, the detected activity was associated with two well-defined areas on the strip. The origin peak represented technetium complexes, hydrolyzed or reduced technetium, and/or colloidal technetium, while the peak near the solvent front represented the [^{99m}Tc] TcO_4^- . Areas under each peak were integrated, and the radiochemical purity given as a percentage of the total integrated area.

7.2.1.5. Radionuclidic purity

The relative radionuclidic impurities in the ^{100}Mo and ^{99m}Tc aliquots were determined via γ -ray spectroscopy using an HPGe detector (Ortec model GEM35P4-S). Samples were placed on a rigid stand 25 cm from the detector end cap, and dead times maintained below 5%. Aliquots of approximately 1–20 μL were used to quantify ^{94g}Tc , ^{95g}Tc , ^{96g}Tc , ^{99}Tc , ^{97}Nb , and ^{99}Mo contributions. These aliquots were evaluated for both 1 and 10 hr count times, with acquisitions typically commencing within 1–5 hr post-EOB. Evaluation of the ^{95m}Tc and ^{97m}Tc impurities was performed by evaluating a > 1 mL sample volume between 5–8 days post-EOB. Since the ^{99m}Tc had essentially all decayed for this assay, the longer-lived ^{96g}Tc was also evaluated. As the ratio of ^{96g}Tc to ^{99m}Tc was previously determined in the initial aliquots, re-assessment of the ^{96g}Tc allowed for calculation of the relative contributions of ^{95m}Tc and ^{97m}Tc to ^{99m}Tc .

Table 7-3. Summary of nuclear decay data obtained from the NNDC NuDat database [6].

Radionuclide	$t_{1/2}$	E_{γ} [keV]	I_{γ} [%]
^{99m} Tc	6.01 hr	140.511	89.08 ^a
^{97m} Tc	91.0 d	96.5	0.32
^{96g} Tc	4.28 d	812.54	82
^{95g} Tc	20.0 hr	765.789	93.8
^{95m} Tc	61 d	204.117	63.2
^{94g} Tc	293 min	702.67	99.6
⁹⁹ Mo	65.94 hr	739.500	12.13
⁹⁷ Nb	72.1 min	657.94	98.23

^a Includes 0.02% contribution from the 142.63 keV γ -ray

The detector was calibrated at the fixed 25 cm geometry using NIST traceable calibration sources (Eckert and Ziegler) of ²²Na, ⁵⁴Mn, ⁵⁷Co, ⁶⁰Co, ¹⁰⁹Cd, ¹³³Ba and ¹³⁷Cs. All activities were corrected for decay during counting time and decay to EOB as described by Selwyn et al. [7]. The decay data that was used to calculate the activity of the radionuclides was obtained from the NNDC NuDat database [6] and is summarized in Table 7-3.

7.2.1.6. *Chemical purity: Aluminum*

The USP pertechnetate monograph states that aluminum evaluation should be performed if separation is accomplished by an alumina column in the preparation of the injection. While an alumina column was not used in these studies, this test was nevertheless considered important since the molybdenum is affixed onto an aluminum target plate which remained present during target dissolution. This semiquantitative test was conducted according to the method described by the commercial test strip supplier (Biodex). A drop of the test solution was placed on the strip and a reference standard drop of 2.5 $\mu\text{g/mL}$ was placed on a second strip. The test sample colour intensity was then visually compared to the reference standard colour intensity.

7.2.1.7. *Chemical purity: Methyl Ethyl Ketone (MEK)*

This test was not performed since MEK was not used for the chemical extractions in these studies.

7.2.1.8. *Additional tests for injection: Sterility*

A decayed sample of lots AE-N1 through AE-N3 was taken for sterility testing. Samples were prepared for sterility testing by withdrawing an aliquot from each lot, and redistributing the volume into a sterile, pyrogen-free, septum sealed, capped, labelled vial. All samples were submitted to Keystone Labs, Inc. (Edmonton, AB), a qualified contract lab used by ERC for sterility testing.

7.2.1.9. *Additional tests for injection: Osmolality*

A decayed sample of the eluted ^{99m}Tc from lots AE-N1 through AE-N5 was submitted for osmolality testing to Dynacare (Edmonton, AB). The purpose of this test was to ensure that no significant residual ammonium or sodium carbonate was added to the [^{99m}Tc]TcO₄⁻ from the lines and/or resin after the automated separation system cleared the lines with air. From lot AE-N5, an appropriate volume of 5% NaCl was added to a sample of [^{99m}Tc]TcO₄⁻ for injection purposes to yield an NaCl concentration of 0.9%. Both the initial unadjusted, and adjusted samples of lot AE-N5 were submitted for osmolality testing.

7.2.2. *Additional chemical purity tests*

7.2.2.1. *Chemical purity: Hydrogen peroxide*

The peroxide content was evaluated semiquantitatively using the EM Quant[®] colorimetric peroxide testing strips within one hour post extraction. Initially, 100–1000 mg/L strips were used. As no positive test results were noted, 1–100 mg/L range testing strips were instead employed. Tests were conducted using the method outlined by the supplier (EMD Chemicals), whereby the 1–100 mg/L peroxide testing strip was immersed into the sample for one second, removed, and excess liquid let to run off the edge of the strip onto absorbent

paper. The color intensity of the strip was visually compared to the supplied colour scale standards after it had reacted for five seconds.

7.2.2.2. *Chemical purity: Molybdenum*

The chemical molybdenum content was evaluated semiquantitatively using the EM Quant[®] colorimetric testing kit (EMD Chemicals). This test was conducted according to the method described by the commercial test strip supplier. For this test, using the spoon provided with the testing kit, a level spoonful of sulfamic acid was dissolved into 5 mL of decayed pertechnetate. The pH of the solution was evaluated to ensure a value below 1 and adjusted with sulphuric acid if necessary. The colorimetric strip was immersed in the solution for 1 minute, excess liquid was removed, and then the test sample color intensity was visually compared to the reference colour indicator chart.

7.2.3. *Stability of [^{99m}Tc]TcO₄⁻ and labelling of other ^{99m}Tc-pharmaceuticals*

7.2.3.1. *Pertechnetate*

The radiochemical stability of the [^{99m}Tc]TcO₄⁻ was evaluated via ITLC-SG as described above. Stability was measured out to 48 hours for sample lots AE-N1 through AE-N5. Inverted vial stability testing was performed on lot AE-N4 to monitor for possible interactions with the vial septum.

7.2.3.2. *Methylene diphosphonate*

MDP kits used in these studies were supplied by ERC. After labelling, radiochemical purity was evaluated via ITLC. Colloidal technetium was evaluated by ITLC-SG using 0.9% NaCl as the mobile phase. Free pertechnetate was initially evaluated using ITLC-SG with MEK as a mobile phase; however, for consistency with the methodology implemented at ERC, we later changed to Whatman 31 ET (W 31 ET) paper with acetone as a mobile phase. The labelling efficiency for MDP was calculated by subtracting out the measured values for both colloidal Tc and free pertechnetate.

7.2.3.3. *Disofenin*

Disofenin kits used in these studies were supplied by ERC. After labelling, radiochemical purity was evaluated via ITLC. ITLC-SG strips were used with 50% methanol as the mobile phase to evaluate colloidal technetium and free pertechnetate was evaluated using silicic acid ITLC (ITLC-SA) and 30% NaCl as a mobile phase. The labelling efficiency for disofenin was calculated by subtracting out the measured values for both colloidal Tc and free pertechnetate.

7.2.4. *Biodistribution studies*

In addition to the [^{99m}Tc]MDP rabbit imaging studies presented in Chapter 5, biodistribution studies were also carried out with [^{99m}Tc]disofenin and [^{99m}Tc]TcO $_4^-$. Both rabbit imaging studies and mice dissection studies were performed and the corresponding protocols are outlined below. All animal experiments were carried out in accordance with guidelines of the Canadian Council on Animal Care and were approved by the local animal care committee of the Cross Cancer Institute.

7.2.4.1. *Rabbit [^{99m}Tc]disofenin biodistribution study*

The [^{99m}Tc]disofenin was diluted to 200 MBq/mL with 0.9% NaCl solution of which 0.2 mL, or 40 MBq, was then injected intravenously into the ear vein of a rabbit using a 26G needle. Planar images were acquired starting between 5 and 10 minutes post-injection on a Symbia T16 SPECT/CT system. A comparison of the cyclotron and generator-based images was performed qualitatively through visual inspection of the images. Two different rabbits were used for this study.

7.2.4.2. *Mouse [^{99m}Tc]disofenin biodistribution study*

Labelled [^{99m}Tc]disofenin was diluted to 0.15 MBq/mL with nitrogen purged 0.9% NaCl solution. Following sixty minutes of fasting, 0.1 mL of the diluted solution, or 15 kBq, was injected intravenously into the caudal tail vein of three, 20–30 g, male BALB/c mice using a 26G needle. Each mouse was

ethanized in a CO₂ chamber sixty minutes post-injection. The intestine, gallbladder, liver, kidneys, stomach excluding duodenum, and blood were removed and their activity was assayed on a Wizard 1480 gamma counter (PerkinElmer).

7.2.4.3. Rabbit [^{99m}Tc]TcO₄⁻ biodistribution study

The [^{99m}Tc]TcO₄⁻ was diluted to 200 MBq/mL with 0.9% NaCl solution of which 0.2 mL, or 40 MBq, was then injected intravenously into the ear vein of a rabbit using a 26G needle. Image acquisition started 8 and 23 minutes post-injection for the cyclotron and generator [^{99m}Tc]TcO₄⁻, respectively. The same rabbit was used for both [^{99m}Tc]TcO₄⁻ scans. Identical time-point imaging was challenging as the gamma camera was located several floors below the vivarium which is where the injection took place. A 50 minute dynamic image acquisition was performed with 1 minute frames on an ADAC Argus single head gamma camera using a LEGP collimator. Qualitative comparison of the cyclotron and generator-based images was performed through visual inspection of the images, as well as comparison of uptake trends in the thyroid, heart, liver, and kidneys. Trends were determined by segmenting the respective organs in the summed image dataset, extending the regions of interest (ROI) to all 50 images, and then calculating the average background subtracted pixel intensity for each region.

7.2.4.4. Mouse [^{99m}Tc]TcO₄⁻ biodistribution study

The [^{99m}Tc]TcO₄⁻ was diluted to 0.30 MBq/mL with 0.9% NaCl solution of which 0.1 mL, or 30 kBq, was then injected intravenously into the caudal tail vein of a mouse using a 26G needle. Five male BALB/c mice were used for each time-point dataset, except for the cyclotron pertechnetate 4 hr time point, of which only four mice were evaluated. At 15 min, 45 min, and 4 hr post-injection, the mice were euthanized in a CO₂ chamber. Uptake in the blood, salivary glands, thyroid, lung, heart, stomach, GIT, liver, kidneys, testes, brain was evaluated following activity assay on a Wizard 1480 gamma counter.

7.3. Results and Discussion

7.3.1. USP specifications

Excluding radionuclidic purity, results of tests described in Section 7.2.1 are summarized in Table 7-4 alongside USP specifications where appropriate. While specific half-life limits are not reported in the USP, the reported half-lives are comparable with the half-life of ^{99m}Tc . The measured endotoxin content, pH, RCP, Al^{3+} , osmolality and sterility of all measured samples fell within clinical specifications.

The radionuclidic purity (RNP) data is summarized in Table 7-5. Values are reported as a percentage of the total ^{99m}Tc activity at EOB. Since early experiments were not optimized for detection of ^{95m}Tc and ^{97m}Tc , these components were not evaluated (NE) in the initial lots. While attempts were always made to evaluate ^{99}Mo , this component was not always detected (ND) despite 10 hour assay times. Activity of ^{97}Nb is not reported, as this component was not observed in the extracted ^{99m}Tc .

It was not possible to compare the radiotechnetium contaminants to USP specifications since the USP is specific to the $^{99}\text{Mo} \rightarrow ^{99m}\text{Tc}$ based production strategy, and radiotechnetium contaminants are therefore not listed. Since a value for ^{99}Mo is listed, despite the different production methods, we have nevertheless compared the ^{99}Mo measured in this work with USP specifications and note that when detected, this contaminant was below the USP specification of 0.15 kBq/MBq, or 0.015%.

Table 7-4. Summary of test results to evaluate USP specifications.

Lot	$t_{1/2}$ [hr] Same Day	$t_{1/2}$ [hr] Overnight	Endotoxin [EU/V]	pH	RCP [%]	Al³⁺ [µg/mL]	Sterility	Osmolality of Eluted ^{99m}Tc [mOsm/kg]	Adjusted Osmolality [mOsm/kg]
ME-N1	5.88	6.00	–	5.0	99.2	< 2.5	–	–	–
ME-N2	5.89	5.98	–	5.0	99.6	< 2.5	–	–	–
ME-N3	5.90	6.04	–	6.0	99.8	< 2.5	–	–	–
ME-N4	5.87	6.04	–	7.0	99.7	< 2.5	–	–	–
ME-N5	5.91	5.98	–	7.0	99.8	< 2.5	–	–	–
ME-R1	5.99	6.03	–	6.5	99.9	< 2.5	–	–	–
ME-R2	–	–	–	6.0	99.9	< 2.5	–	–	–
ME-R3	–	–	–	6.5	99.8	< 2.5	–	–	–
AE-N1	6.01	6.01	< 120	6.5	99.7	< 2.5	Pass	26	–
AE-N2	6.04	5.99	< 120	5.0	98.3	< 2.5	Pass	5	–
AE-N3	6.01	5.98	< 120	5.0	99.4	< 2.5	Pass	5	–
AE-N4	–	–	< 120	6.0	99.6	< 2.5	–	4	–
AE-N5	–	–	< 120	6.0	99.7	< 2.5	–	11	318
Criteria:	–	–	≤ 175	4.5–7.5	> 95	≤ 10	Pass	N/A	250–370

Table 7-5. Relative RNP data reported as a percentage of ^{99m}Tc at EOB.

Lot	^{100}Mo Batch	^{94g}Tc	^{95m}Tc	^{95g}Tc	^{96g}Tc	^{97m}Tc	^{99}Mo
ME-N1	1-N	0.0204	NE	0.0392	0.0151	NE	ND
ME-N2	1-N	NE	NE	0.0407	0.0158	NE	ND
ME-N3	1-N	0.0178	NE	0.0406	0.0142	NE	ND
ME-N4	1-N	0.0157	NE	0.0391	0.0156	NE	ND
ME-N5	1-N	0.0665	NE	0.0477	0.0150	NE	ND
ME-R1	1-R	0.0245	NE	0.0439	0.0173	NE	ND
ME-R2	1-R	0.0234	NE	0.0405	0.0154	NE	0.0080
ME-R3	1-R	0.0181	NE	0.0439	0.0144	NE	ND
AE-N1	2-N	0.0030	0.000016	0.0028	0.0013	0.0078	0.0011
AE-N2	2-N	0.0022	0.000013	0.0009	0.0009	0.0060	ND
AE-N3	2-N	0.0028	0.000018	0.0025	0.0010	0.0058	0.0014
AE-N4	2-N	0.0033	0.000011	0.0022	0.0007	0.0046	0.0004
AE-N5	2-N	0.0023	0.000013	0.0023	0.0009	0.0057	0.0013

Significant differences in radionuclidic impurities were noted between the two batches of ^{100}Mo used in these studies, a finding which was similar to the batch comparison results of Scholten et al. [2]. As observed from the results of Table 7-5, the effect of the ^{100}Mo batch had a greater impact on the RNP than the irradiation energy. Furthermore, Batch #2 with a 97.39% enrichment ^{100}Mo , gave much lower levels of the high-energy γ -emitting radionuclidic impurities such as ^{96g}Tc and ^{95g}Tc than the more highly enriched Batch #1 which had a ^{100}Mo enrichment of 99.27%. This difference is explained by evaluating the isotopic impurity profile of Table 7-1. While the overall ^{100}Mo enrichment of Batch #1 is higher than Batch #2, the $^{92-97}\text{Mo}$ contaminants of Batch #1 are approximately 10-fold larger than Batch #2. The ^{98}Mo contaminant comprises only 64% of the total isotopic contaminants of Batch #1, while in Batch #2 ^{98}Mo accounts for 99% of the isotopic molybdenum impurities.

The possible Tc-producing reactions up to 19 MeV for ^{98}Mo will be $^{98}\text{Mo}(p,n)^{98}\text{Tc}$, $^{98}\text{Mo}(p,2n)^{97g}\text{Tc}$, and $^{98}\text{Mo}(p,2n)^{97m}\text{Tc}$. Since the first two of these

reactions leads to products with half-lives of 4.2×10^6 y, the produced activity of ^{98}Tc and ^{97g}Tc will be negligible. While ^{97m}Tc may also be produced, it emits a single γ -ray at 96.5 keV, with an abundance of 0.32%. Thus, when considering both dosimetry and image quality in selecting a batch of ^{100}Mo for clinical production of ^{99m}Tc , one should not ask the question, “What is the enrichment of ^{100}Mo ?” but rather, “What is the isotopic impurity profile of the ^{100}Mo ?” A batch of ^{100}Mo with high ^{98}Mo contaminant, but limited $^{92-97}\text{Mo}$ contaminants will likely be preferred over a batch of higher enrichment ^{100}Mo that has significantly higher levels of $^{92-97}\text{Mo}$.

7.3.2. Additional chemical purity tests

Chemical peroxide and molybdenum concentrations were evaluated for lots AE-N4 and AE-N5. The peroxide concentration was $< 1 \mu\text{g/mL}$ and the molybdenum concentration was $< 5 \mu\text{g/mL}$ for both lots. Although the strip-based test for evaluation of peroxide is straightforward, the current molybdenum test is not convenient as the EM Quant[®] colorimetric testing kit requires 5 mL of solution. Since the $[\text{}^{99m}\text{Tc}]\text{TcO}_4^-$ is currently eluted in 10 mL, this test therefore consumes 50% of the final solution. Further investigation is necessary either to implement a different testing strategy such as neutron activation analysis, or to validate a modified version of the existing test which would require less volume.

7.3.3. Stability of $[\text{}^{99m}\text{Tc}]\text{TcO}_4^-$ and labelling of other ^{99m}Tc -pharmaceuticals

The RCPs of $[\text{}^{99m}\text{Tc}]\text{TcO}_4^-$, $[\text{}^{99m}\text{Tc}]\text{MDP}$, and $[\text{}^{99m}\text{Tc}]\text{disofenin}$ are summarized in Table 7-6 and Table 7-7. The column headings of Table 7-6 represent the number of hours post-extraction, while the headings in Table 7-7 correspond to the number of hours post-labelling. Typical RCPs of at least 99% were noted for the extracted $[\text{}^{99m}\text{Tc}]\text{TcO}_4^-$, and, except for ME-N1 and AE-N1, all evaluated lots remained within USP limit of $> 95\%$ up to 24 hr post extraction. The low values for ME-N1 and AE-N1 at 3 hr and 24 hr, respectively, were considered anomalies since the RCPs evaluated at later time-points were $> 95\%$.

Table 7-6. [^{99m}Tc]TcO $_4^-$ radiochemical purity and stability from 1–50 hr post extraction.

Lot	1 hr	2 hr	3 hr	4 hr	6 hr	14 hr	16 hr	18 hr	20 hr	24 hr	48 hr	50 hr	Mobile Phase
ME-N1	99.2	97.0	93.4	–	–	–	–	–	–	96.8	–	–	Acetone
ME-N2	99.6	–	–	–	–	–	–	–	–	97.7	–	–	0.9% NaCl
ME-N3	–	–	–	–	99.8	–	–	–	–	99.8	–	–	0.9% NaCl
ME-N4	–	99.7	–	–	–	–	–	–	–	99.6	95.4	–	0.9% NaCl
ME-N5	99.8	–	–	–	–	–	–	–	–	–	–	–	0.9% NaCl
ME-R1	99.9	–	–	–	–	–	–	–	–	–	–	–	0.9% NaCl
ME-R2	99.9	–	–	–	–	–	–	–	–	–	–	–	0.9% NaCl
ME-R3	99.8	–	–	–	–	–	–	–	–	–	–	–	0.9% NaCl
AE-N1	99.7	99.7	99.5	–	–	98.7	–	98.0	–	92.8	95.7	–	n-butanol
AE-N2	98.3	98.4	99.3	98.3	–	–	98.9	–	98.8	99.0	97.3	–	n-butanol
AE-N3	99.4	98.4	99.0	99.0	–	–	98.6	–	99.0	98.5	91.3	–	n-butanol
AE-N4 ^a	–	99.6	–	–	99.6	–	–	–	–	99.1	91.2	–	n-butanol
AE-N5	99.7	99.7	99.8	–	98.8	99.7	–	–	–	99.2	–	92.5	n-butanol

^a Inverted vial (all others upright)

Table 7-7. Labelling efficiency and stability for MDP and disofenin^a.

Lot		0.25 hr	1 hr	2 hr	3 hr	5 hr	24 hr	48 hr	Stationary Phase	Mobile Phase
ME-N1	MDP	–	95.3	–	–	–	–	–		
	Colloid	–	3.5	–	–	–	–	–	ITLC-SG	0.9% NaCl
	Pert	–	1.2	–	–	–	–	–	ITLC-SG	MEK
ME-N2	MDP	–	–	96.8	–	–	98.5	–		
	Colloid	–	–	2.8	–	–	1.1	–	ITLC-SG	0.9% NaCl
	Pert	–	–	0.4	–	–	0.3	–	ITLC-SG	MEK
ME-N3	Disofenin	–	97.2	–	–	–	82.9	–		
	Colloid	–	1.2	–	–	–	2.2	–	ITLC-SG	50% MeOH
	Pert	–	1.6	–	–	–	14.9	–	ITLC-SA	30% NaCl
ME-N4	Disofenin	–	95.4	–	–	–	–	–		
	Colloid	–	1.8	–	–	–	–	–	ITLC-SG	50% MeOH
	Pert	–	2.8	–	–	–	–	–	ITLC-SA	30% NaCl
ME-N5	MDP	–	96.7	–	–	–	–	–		
	Colloid	–	2.3	–	–	–	–	–	ITLC-SG	0.9% NaCl
	Pert	–	1.0	–	–	–	–	–	ITLC-SG	MEK
ME-R1	MDP	–	95.1	–	–	–	–	–		
	Colloid	–	2.5	–	–	–	–	–	ITLC-SG	0.9% NaCl
	Pert	–	2.3	–	–	–	–	–	ITLC-SG	MEK
ME-R2	MDP	–	96.7	–	–	94.0	–	–		
	Colloid	–	0.9	–	–	1.7	–	–	ITLC-SG	0.9% NaCl
	Pert	–	2.5	–	–	4.3	–	–	W 31 ET	Acetone
ME-R3	MDP	–	96.3	–	–	–	–	–		
	Colloid	–	0.8	–	–	–	–	–	ITLC-SG	0.9% NaCl
	Pert	–	2.9	–	–	–	–	–	W 31 ET	Acetone
AE-N1	MDP	98.6	98.5	98.7	96.8	–	98.7	97.5		
	Colloid	0.8	0.8	0.6	2.4	–	0.5	1.9	ITLC-SG	0.9% NaCl
	Pert	0.6	0.8	0.7	0.8	–	0.8	0.6	W 31 ET	Acetone
AE-N2	MDP	98.2	98.3	98.9	98.6	–	98.5	96.5		
	Colloid	0.8	0.8	0.6	0.5	–	0.4	1.1	ITLC-SG	0.9% NaCl
	Pert	1.0	0.9	0.6	0.9	–	1.1	2.4	W 31 ET	Acetone
AE-N3	MDP	98.9	98.4	98.6	98.6	–	98.7	97.5		
	Colloid	0.4	0.8	0.5	0.4	–	0.6	0.9	ITLC-SG	0.9% NaCl
	Pert	0.7	0.9	0.9	0.9	–	0.7	1.6	W 31 ET	Acetone

^a Variation from 100% due to rounding

Labelling efficiencies > 95% for both [^{99m}Tc]MDP and [^{99m}Tc]disofenin were observed as noted in Table 7-7. Good stability of the [^{99m}Tc]MDP was also noted up to 48 hr post-labelling, particularly for the ^{99m}Tc obtained via the automated extraction system.

7.3.4. Biodistribution studies

The results of the rabbit and mouse biodistribution studies with [^{99m}Tc]disofenin and [^{99m}Tc]TcO $_4^-$ are described in the following section. In these studies, the rabbit data are presented qualitatively, while the mouse results are reported quantitatively.

7.3.4.1. Rabbit [^{99m}Tc]disofenin biodistribution study

The [^{99m}Tc]disofenin rabbit images obtained 5–10 minutes post-injection are presented in Figure 7-1. Images are displayed using the default window/levelling settings of the upper and lower limits set to the maximum and minimum pixels intensities, respectively, for each image. In the cyclotron-based image (right), contamination of the ear at the injection site was noted.

Due to the fast dynamics associated with this particular radiopharmaceutical, and the fact that the vivarium where the injection took place and gamma camera are separated by three floors, imaging at identical time-points post-injection was not straightforward. Nevertheless, similar qualitative distributions were generally noted, however analysis would benefit from further repeated uptake studies.

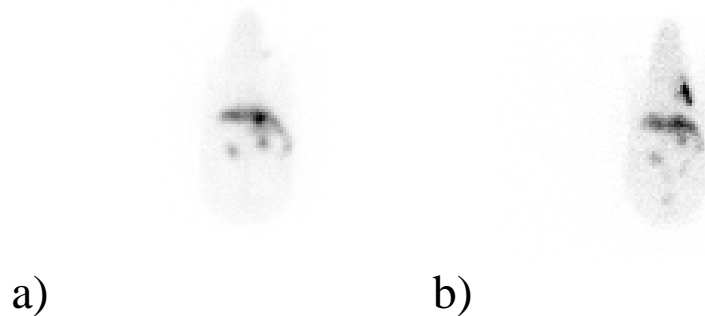


Figure 7-1. 40 MBq [^{99m}Tc]disofenin uptake in two different rabbits 5–10 minutes post-injection using (a) generator-based and (b) cyclotron-based ^{99m}Tc .

7.3.4.2. *Mouse [^{99m}Tc]disofenin biodistribution study*

The average and standard deviation of the triplicate [^{99m}Tc]disofenin uptake measurements in mice are reported in Table 7-8 for both generator- and cyclotron-based ^{99m}Tc. To evaluate whether the generator and cyclotron datasets differ significantly, the unpaired two-tailed t-test p-values and the clinical QC limits used by ERC are also reported in Table 7-8. While no significant differences in solid organ uptake are noted, uptake differences with p < 0.05 are noted for blood. The reason for this discrepancy is unknown, however all mice individually satisfied the clinical QC criteria.

Table 7-8. 15 kBq [^{99m}Tc]disofenin uptake in mice 1 hr post-injection.

	Generator	Cyclotron	p-value	Criteria
Intestine + Gallbladder [%]	88.2 ± 5.3	87.2 ± 0.8	0.7628	> 80%
Liver [%]	3.6 ± 1.4	2.9 ± 0.1	0.4346	< 10%
Kidneys [%]	1.3 ± 0.3	1.7 ± 0.2	0.1270	< 10%
Stomach [%]	0.3 ± 0.3	0.8 ± 0.5	0.2117	< 3%
Blood [%]	1.4 ± 0.1	1.99 ± 0.03	0.0006	< 3%
Body Mass [g]	22.6 ± 0.7	21.6 ± 0.2	–	20–30

7.3.4.3. *Rabbit [^{99m}Tc]TcO₄⁻ biodistribution study*

Examples of the [^{99m}Tc]TcO₄⁻ rabbit images at 25, 40, and 55 minute post-injection obtained during the 50 minute dynamic scan are given in Table 7-9. Images were initially prepared using window/level settings which spanned the maximum and minimum pixel intensities, however this resulted in images which revealed little tissue uptake other than in the bladder. The presented images were therefore displayed with saturation of 0.6% of the displayed pixels as obtained using the ImageJ image analysis software platform (National Institutes of Health, v. 1.44p). Overall, similar distributions were noted between the generator and cyclotron sources of ^{99m}Tc, however, as noted above for [^{99m}Tc]disofenin, these

results are qualitative and analysis would benefit from further repeated uptake studies.

Table 7-9. 40 MBq [^{99m}Tc]TcO $_4^-$ uptake in at 25, 40, and 55 minutes post-injection using the same rabbit.

	25 minutes	40 minutes	55 minutes
Generator			
Cyclotron			

The average background subtracted pixel value in each of the manually contoured thyroid, heart, liver, and kidney ROIs obtained for each source of ^{99m}Tc for each of the 50 rabbit images in the dynamic scans are shown in Figure 7-2. While perhaps slightly more quantitative than a visual comparison of the images, this analysis should be considered qualitative as the average pixel intensity will depend on both the size and margins of the delineated ROIs. ROIs drawn on the generator-based images were perhaps slightly larger than those of the cyclotron-based images which would consequently explain the overall higher pixel intensity for the cyclotron-based images. Nevertheless, evaluation of the data revealed similar trends in the uptake of [^{99m}Tc]TcO $_4^-$ in the thyroid, as well as similar

clearance trends for the heart and liver. Uptake in the kidneys was somewhat variable, and difficult to compare, particularly since early time-point data was not available for the generator-based $[^{99m}\text{Tc}]\text{TcO}_4^-$.

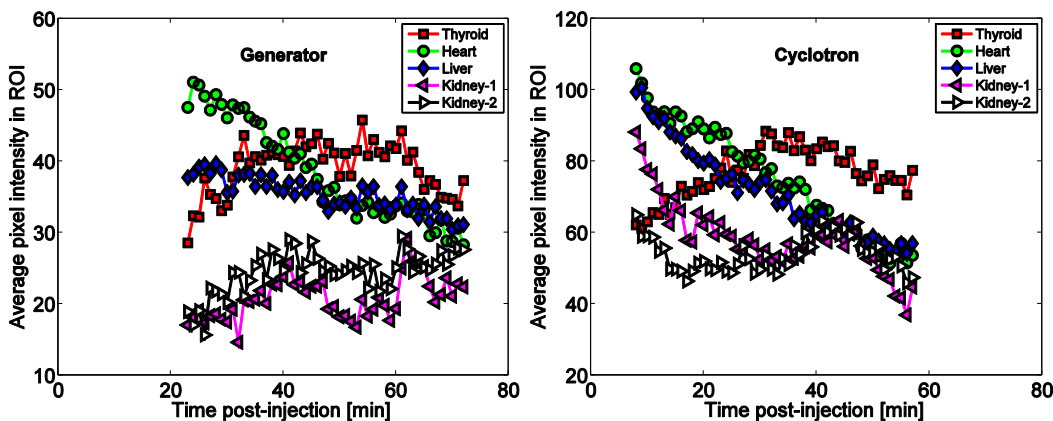


Figure 7-2. ROI delineations to evaluate uptake of 40 MBq $[^{99m}\text{Tc}]\text{TcO}_4^-$ in the same rabbit for a 50 minute dynamic scan acquisition using both generator and cyclotron sources of ^{99m}Tc .

7.3.4.4. *Mouse $[^{99m}\text{Tc}]\text{TcO}_4^-$ biodistribution study*

The average and standard deviation of the five, or four for the cyclotron 4 hr time-point, $[^{99m}\text{Tc}]\text{TcO}_4^-$ uptake measurements in mice as a function of time are reported in Figure 7-3 for both generator- and cyclotron-based ^{99m}Tc . The figure has been divided into four sub-plots for clarity. Data was also plotted on a bar chart in Figure 7-4 for ease in comparison of organ systems. In general, good quantitative agreement was noted for both sources of ^{99m}Tc for the ten organs evaluated. Significant differences ($p < 0.05$ for an unpaired two-tailed t-test) were however noted for the liver and lung at 15 minutes and 4 hours, as well as the brain at 15 minutes post injection. The reason for this disagreement is unknown, particularly since no significant uptake differences were noted for any of the 45 minute time points.

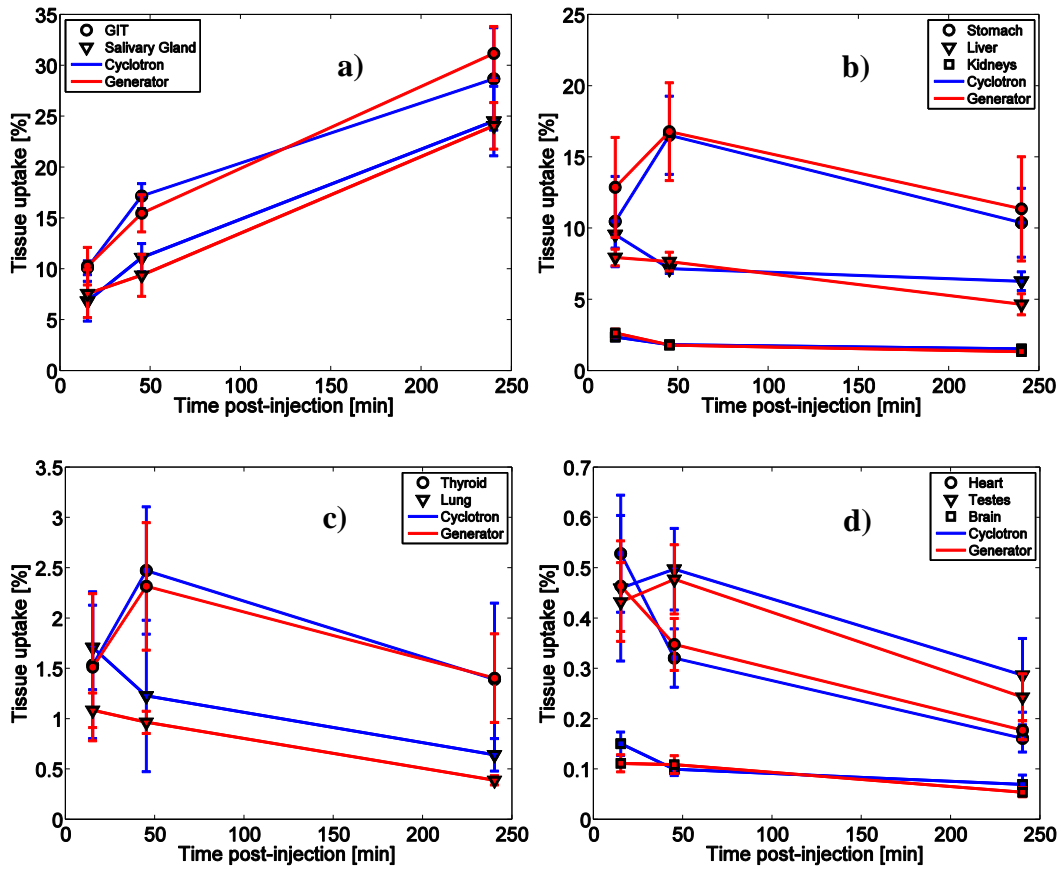


Figure 7-3. 30 kBq ^{99m}Tc uptake in mice as a function of time post-injection. Four subplots are given for ease of visualization.

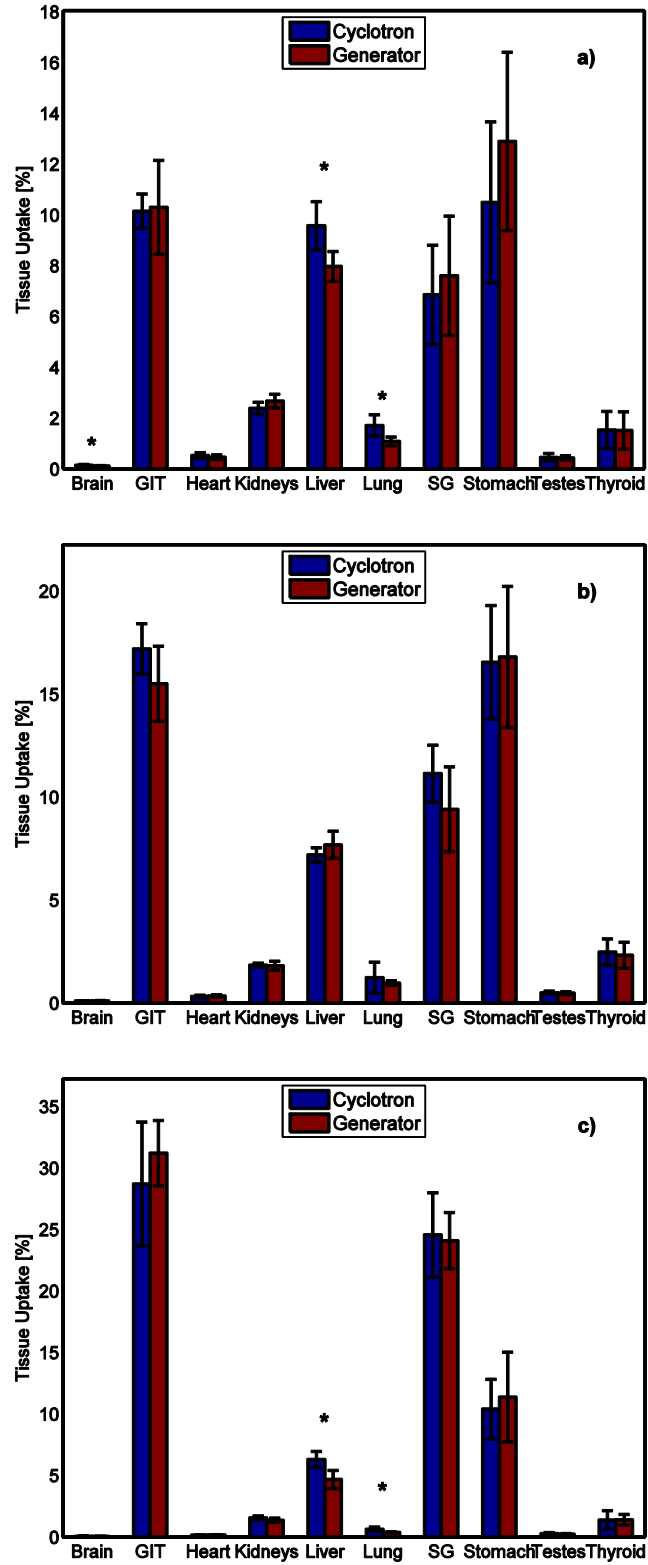


Figure 7-4. 30 kBq [^{99m}Tc]TcO $_4^-$ uptake in mice (a) 15 min, (b) 45 min, and (c) 4 hr post-injection (* $p < 0.05$).

7.4. Conclusion

This Chapter presents a summary of quality data for all ^{99m}Tc produced using either pressed or sintered targets at the EPC up to September 2011. Where relevant, QC parameters were found to be within the USP specifications [1]. In considering the clinical production of cyclotron-based ^{99m}Tc , new guidelines on radionuclidic purity must be developed. The isotopic composition of the enriched ^{100}Mo must also be carefully selected. Furthermore, depending on the extraction strategy and target materials used, additional chemical testing may be warranted, and it is for this reason that chemical peroxide and chemical molybdenum were evaluated.

While the level of ^{99g}Tc was not itself directly evaluated for these irradiations, this contaminant was not found to have an impact on the labelling efficiency of ^{99m}Tc MDP and ^{99m}Tc disofenin when cyclotron-produced ^{99m}Tc was used. Overall, the uptake assessed by rabbit imaging showed qualitatively similar biodistributions when both generator- and cyclotron- based ^{99m}Tc disofenin and ^{99m}Tc TcO₄⁻ are compared. Overall good agreement was noted for quantitative mouse biodistribution studies of generator- and cyclotron-based ^{99m}Tc disofenin and ^{99m}Tc TcO₄⁻.

7.5. References

1. U.S. Pharmacopeia (Pertechnetate).
http://www.pharmacopeia.cn/v29240/usp29nf24s0_m80740.html
(accessed 2011).
2. B. Scholten, R. Lambrecht, M. Cogneau, H. Ruiz, S. Qaim, Excitation functions for the cyclotron production of ^{99m}Tc and ^{99}Mo , *Appl. Radiat. Isot.* 51 (1999) 69–80.
3. K. Gagnon, F. Bénard, M. Kovacs, T.J. Ruth, P. Schaffer, J.S. Wilson, S.A. McQuarrie, Cyclotron production of ^{99m}Tc : Experimental

measurement of the $^{100}\text{Mo}(p,x)^{99}\text{Mo}$, $^{99\text{m}}\text{Tc}$ and $^{99\text{g}}\text{Tc}$ excitation functions from 8 to 18 MeV, Nucl. Med. Biol. 38 (2011) 907–916.

4. U.S. Pharmacopeia (Sterility).
http://www.pharmacoepia.cn/v29240/usp29nf24s0_c71.html (accessed 2011).
5. U.S. Pharmacopeia (Osmolality and Osmolarity).
http://www.pharmacoepia.cn/v29240/usp29nf24s0_c785.html (accessed 2011).
6. National Nuclear Decay Center, Nuclear structure and decay Data (NuDat 2.5) <http://www.nndc.bnl.gov/nudat2/> (accessed 2011).
7. R. Selwyn, R. Nickles, B. Thomadsen, L. DeWerd, J. Micka, A new internal pair production branching ratio of ^{90}Y : The development of a non-destructive assay for ^{90}Y and ^{90}Sr , Appl. Radiat. Isot. 65 (2007) 318–327.

8. Summary and future direction

8.1. Research summary

With the recent shortages in the reactor-based supply of ^{99m}Tc and the growing use of cyclotron infrastructure for production and distribution of PET isotopes, the direct cyclotron production of ^{99m}Tc is a promising alternative as a reliable supply of this key medical isotope. The focus of this dissertation was to address several of the technical challenges related to the direct cyclotron production of ^{99m}Tc . An overview of previously existing technetium production strategies using a cyclotron was introduced in Chapter 2 [1].

As an initial task, we felt it was imperative to obtain a better understanding of the probability for coproduction of ^{99g}Tc since it has been suggested that this contaminant may have implications in subsequent radiopharmaceutical labelling [2]. Unlike ^{99m}Tc , the evaluation of ^{99g}Tc production via γ -ray spectroscopy is not straightforward due its low overall radioactivity and the low, $6.5 \times 10^{-4} \%$, abundance of its single 89.5 keV γ -ray. In Chapter 3 we describe the use of mass spectrometry to quantify ^{99g}Tc and make the first experimental measurement of the ^{99g}Tc excitation function in the energy range of 8 to 18 MeV [3]. These results suggested that similar ratios of ^{99m}Tc to ^{99g}Tc nuclei can be expected when comparing typical cyclotron irradiation parameters with a standard $^{99}\text{Mo}/^{99m}\text{Tc}$ generator eluted at a 24 hr frequency.

Since the cross sections for producing ^{99m}Tc , as well as potential contaminants, depend on the proton irradiation energy, data presented in Chapter 4 revealed a simple strategy for evaluating the proton energy of a cyclotron without the need for sophisticated equipment or data analysis [4]. Knowledge of the irradiation energy is important for the selection of irradiation parameters to balance the optimal ^{99m}Tc yields with tolerable levels of ^{99g}Tc .

Next, we note that highly enriched ^{100}Mo must be used in order to achieve ^{99m}Tc of high radionuclidic purity. As this enriched material is in limited supply and expensive, and since the bulk of the material is not consumed during irradiation, a method for recycling irradiated ^{100}Mo was desirable. In Chapter 5, a strategy for isolating, purifying, and recycling irradiated ^{100}Mo as a metal was developed [5, 6, 7]. An enriched metal to metal recovery of 87% was demonstrated following target preparation, irradiation, $[\text{}^{99m}\text{Tc}]\text{TcO}_4^-$ extraction, ammonium molybdate isolation, and hydrogen reduction. Further improvements are expected with additional optimization experiments.

When considering molybdenum target design strategies, metallic ^{100}Mo is preferred. The poor thermal conductivity of molybdenum oxide severely limits the amount of beam current that can be applied, while metallic molybdenum targets are amenable to the high power irradiations needed for the large-scale production of ^{99m}Tc . Since enriched ^{100}Mo is purchased or recycled as a powder, a technical challenge arose regarding the formation of structurally stable and sufficiently thick metallic targets while minimizing ^{100}Mo material losses. In Chapter 6, a strategy for sintering enriched ^{100}Mo pellets and subsequent bonding onto an aluminum target plate was presented [6, 7]. The ^{100}Mo mass losses were typically less than 2%, and the targets developed in this study were successfully irradiated with proton currents of 80 μA which, to the best of our knowledge, is the highest irradiation current tested to date on enriched ^{100}Mo targets. Curie quantities of ^{99m}Tc were reliably produced and extracted from our targets.

With the goal of using cyclotron-produced ^{99m}Tc for clinical applications, an extensive list of ^{99m}Tc QC data was presented in Chapter 7 [8]. The QC results

from our automated extraction system presented in Chapter 7 were submitted as part of a recent Clinical Trial Application to Health Canada entitled, “A Prospective Phase I Study of Cyclotron-Produced Tc-99m Pertechnetate (CPERT) in Patients With Thyroid Cancer” [9]. This Phase I study was designed to evaluate the safety of cyclotron-produced $[^{99m}\text{Tc}]\text{TcO}_4^-$. As a secondary goal, the trial will compare the uptake of cyclotron- and generator-based $[^{99m}\text{Tc}]\text{TcO}_4^-$ in patients with well differentiated thyroid cancer post-thyroidectomy and pre-treatment with radioactive iodine. This trial was approved by Health Canada on September 30, 2011, and the world’s first clinical images with cyclotron-based $[^{99m}\text{Tc}]\text{TcO}_4^-$ were obtained on October 12, 2011. While this is an ongoing study, the first clinical scan with cyclotron-produced $[^{99m}\text{Tc}]\text{TcO}_4^-$, along with a comparison to generator-based $[^{99m}\text{Tc}]\text{TcO}_4^-$, is presented in Figure 8-1.

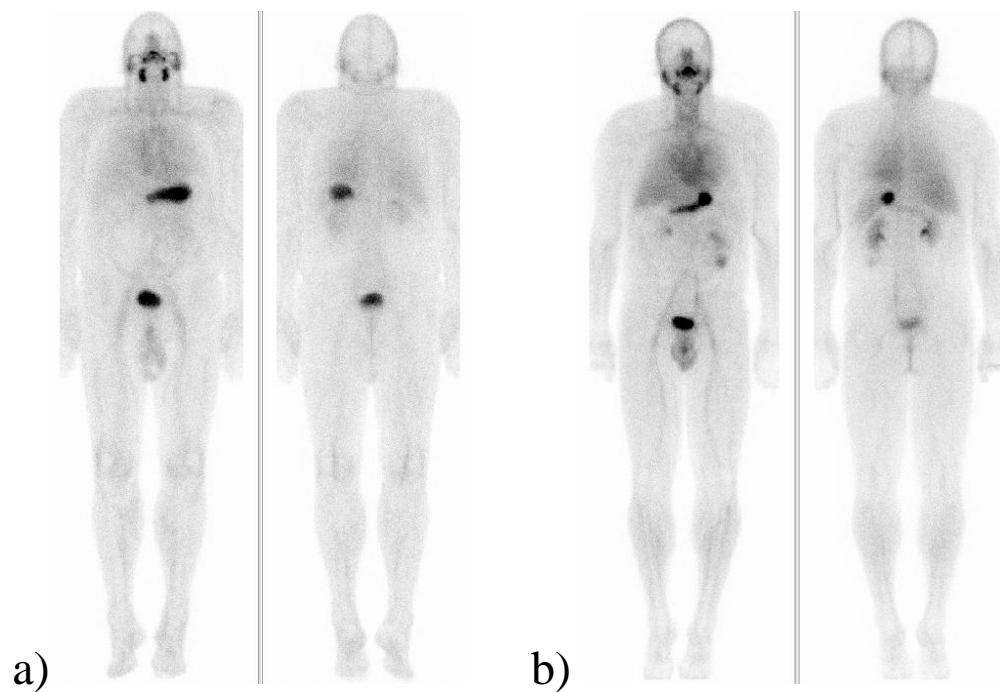


Figure 8-1. Whole body $[^{99m}\text{Tc}]\text{TcO}_4^-$ image for (a) cyclotron and (b) generator $[^{99m}\text{Tc}]\text{TcO}_4^-$.

8.2. Future research

Proton irradiation currents on the order of 500 μA and proton energies of 24 MeV are projected in order to meet the regional/metropolitan clinical demand for the cyclotron-production of $^{99\text{m}}\text{Tc}$. While the research presented in this dissertation was limited to ~ 100 μA at ~ 18 MeV using the existing TR-19/9 cyclotron infrastructure at the Cross Cancer Institute, it is expected that the target recycling and target design technology developed in this work will provide a strong platform for the development of future higher powered targets. With the arrival of a new TR-24 cyclotron in Edmonton scheduled for the spring of 2012, re-evaluation of $^{99\text{m}}\text{Tc}$ quality and target performance at higher beam powers is anticipated in the near future. Upon establishing a reliable supply of cyclotron-produced $^{99\text{m}}\text{Tc}$, detailed assessment regarding the cost of producing and distributing this $^{99\text{m}}\text{Tc}$, in comparison to the current reactor-based scheme will be required.

Due to distribution challenges resulting from the 6 hr half-life of $^{99\text{m}}\text{Tc}$, cyclotron production of $^{99\text{m}}\text{Tc}$ has been typically envisioned as a supplement, as opposed to a complete substitute, for the existing reactor-based strategy. This is particularly true when considering $^{99\text{m}}\text{Tc}$ supply to non-metropolitan areas. One alternative which requires further investigation, however, is the cyclotron production of ^{99}Mo . While the $^{100}\text{Mo}(p,x)^{99}\text{Mo}$ reaction scheme is generally not considered viable for sustaining a large regional supply [2], small quantities of ^{99}Mo are simultaneously produced during the $^{100}\text{Mo}(p,2n)^{99\text{m}}\text{Tc}$ production strategy. Additional assessment is planned to further evaluate whether or not this ^{99}Mo production is useful as it may be of benefit in further supplementing the $^{99\text{m}}\text{Tc}$ supply to remote locations and/or assist in providing emergency or off-hour [$^{99\text{m}}\text{Tc}$] TcO_4^- doses without the need for a full cyclotron production run.

Depending upon isotopic composition, irradiation parameters, chemical processing strategy, target plate material selection, etc., further quality control assessments, biodistribution studies, and clinical trials will be required to establish that cyclotron-produced $^{99\text{m}}\text{Tc}$ -radiopharmaceuticals are a clinically equivalent

substitute to those produced from generator technetium. Nevertheless, the goal of producing high quality ^{99m}Tc on a cyclotron for clinical applications has been met with the successful launch of the Phase I trial noted above, and has resulted in the world's first clinical images with cyclotron-produced ^{99m}Tc .

8.3. References

1. K. Gagnon, S. McQuarrie, D. Abrams, A. J. B. McEwan and F. Wuest, Radiotracers based on technetium-94m, *Current Radiopharmaceuticals*, 4 (2011) 90–101.
2. B. Scholten, R. Lambrecht, M. Cogneau, H. Ruiz, S. Qaim, Excitation functions for the cyclotron production of ^{99m}Tc and ^{99}Mo , *Appl. Radiat. Isot.* 51 (1999) 69–80.
3. K. Gagnon, F. Bénard, M. Kovacs, T.J. Ruth, P. Schaffer, J.S. Wilson and S.A. McQuarrie, Cyclotron production of ^{99m}Tc : Experimental measurement of the $^{100}\text{Mo}(p,x)^{99}\text{Mo}$, ^{99m}Tc , and ^{99g}Tc excitation functions from 8 to 18 MeV, *Nucl. Med. Biol.* 38 (2011) 907–916.
4. K. Gagnon, M. Jensen, H. Thisgaard, J. Publicover, S. Lapi, S.A. McQuarrie, and T.J. Ruth, A new and simple calibration-independent method for measuring the beam energy of a cyclotron, *Appl. Radiat. Isot.* 69 (2011) 247–253.
5. K. Gagnon, J. S. Wilson, C. Holt, D. Abrams, A. J. B. McEwan, D. Mitlin, and S.A. McQuarrie, Cyclotron production of ^{99m}Tc : Recycling of enriched ^{100}Mo metal targets, submitted to *Applied Radiation and Isotopes* (August, 2011).

6. K. Gagnon, C. Holt, J.S. Wilson, D. Mitlin, S. McQuarrie, Target preparation and recycling of molybdenum for the cyclotron production of ^{99m}Tc , *J. Label. Compd. Radiopharm.* 54 (2011) S54.
7. J Wilson, K Gagnon, SA McQuarrie, Target preparation and recycling molybdenum for the cyclotron production of ^{99m}Tc , Report of Invention, patent in process, (April 4th, 2011).
8. K. Gagnon, D. Abrams, J.S. Wilson, S.A. McQuarrie, A.J.B. McEwan, Quality control of cyclotron vs. generator ^{99m}Tc -labeled radiopharmaceuticals, *Eur. J. Nucl. Med. Mol. Imaging.* 38 (2011), S105.
9. A Prospective Phase I Study of Cyclotron-Produced Tc-99m Pertechnetate (CPERT) in Patients With Thyroid Cancer. ClinicalTrials.gov Identifier: NCT01437254, <http://www.clinicaltrials.gov/ct2/show/NCT01437254?term=cyclotron&rank=1> (accessed 2011).